Universität Bonn

Physikalisches Institut

Associated Production of a Top Quark and a Z Boson in pp Collisions at $\sqrt{s} = 13$ TeV Using the ATLAS Detector

Irina Antonela Cioară

The production of a top quark in association with a Z boson is studied using $36.1\,\mathrm{fb}^{-1}$ of proton–proton collision data collected by the ATLAS experiment at the LHC in 2015 and 2016 at a centre-of-mass energy of 13 TeV. The search is performed in the trilepton channel, in which both the Z boson and the top quark decay to final states involving charged leptons. Events containing three identified leptons (electron and/or muon) and two jets, one of which is identified as a b-quark jet are selected. The major backgrounds come from diboson, top-pair production and Z +jets production. An artificial neural network is used to improve the background rejection and the tZq production cross-section is extracted. The result is in agreement with the Standard Model prediction and has an observed significance of $4.2\,\sigma$, thus yielding the first evidence for tZq associated production.

Associated Production of a Top Quark and a Z Boson in pp Collisions at $\sqrt{s} = 13$ TeV Using the ATLAS Detector

Dissertation
zur
Erlangung des Doktorgrades (Dr. rer. nat.)
der
Mathematisch-Naturwissenschaftlichen Fakultät
der
Rheinischen Friedrich-Wilhelms-Universität Bonn

von
Irina Antonela Cioară
aus
Constanța, Rumänien

Bonn, 18.06.2018

Contents

Introduction

The current landscape of particle physics

The Standard Model of particle physics is a theory developed in an attempt to understand and explain the fundamental constituents of matter and their interactions. Until now, it has been experimentally validated in countless analyses, throughout decades of experiments and over a wide energy range. Because of this, it can be regarded as one of the most successful theories in physics. However, the Standard Model does not offer solutions for important open questions (such as matter-antimatter asymmetry or the origin of dark matter) and it does not incorporate gravity.

In the last 10 years significant progress has been made in further validating the Standard Model by analysing proton–proton collision data recorded at the Large Hadron Collider (LHC). This culminated in the discovery of the last missing predicted elementary particle (the Higgs boson) and many precision measurements of different Standard Model parameters, such as the first measurement of the W boson mass in pp collisions performed by the ATLAS collaboration.

One of the most important areas in which such measurements can be performed is related to the heaviest elementary particle in the Standard Model, the top quark. Since its discovery at the Tevatron in 1995, the top quark and its properties have been thoroughly studied. The LHC has proven to be a very good experimental environment for this purpose, producing millions of top quarks during its operation. The first part of the LHC program, referred to as Run 1, at a centre-of-mass energy of 7 TeV and 8 TeV benefited from an increase of the cross-sections for top quark related processes of up to 20 times compared to the Tevatron. Already with this data, a wide variety of precision measurements were performed in top-quark pair production events. In addition, the less probable mechanism, single top-quark production (via t-, s-channel or tW interactions) was extensively investigated. However, it was the increase in centre-of-mass energy up to 13 TeV in Run 2 of the LHC operations that has opened up new possibilities in terms of accessibility to other top-quark related processes with very small cross-sections.

One of these processes is the associated production of a single top-quark and a Z boson (tZq). This production mode probes the coupling of the top quark to the Z boson, as well as the WWZ coupling. Additionally, it constitutes an important background for other analyses related to rare top-quark processes, like the associated tH production, or beyond Standard Model searches, like flavour changing neutral currents involving top-quarks. Prior to the analysis presented in this thesis, tZq production has never been investigated by the ATLAS collaboration.

1

Thesis overview and structure

This thesis describes the first ATLAS search for *tZq* associated production, as predicted by the Standard Model. This was performed using proton–proton collision data collected by the ATLAS detector at a centre-of-mass energy of 13 TeV during its 2015-2016 operation. The data that was used corresponds to 36.1 fb^{-1} integrated luminosity. Events in which both the *W* boson coming from the top quark and the Z boson decay leptonically (resulting in a final state including three leptons, missing transverse energy and two jets) are considered. The results of this analysis have been published in ref. [1], and represent the first strong evidence of associated production of a *Z* boson and a single top-quark, with the measured cross-section being in agreement with the theoretical predictions and the observed statistical significance of the result being 4.2 σ.

The thesis is structured as follows. Chapter 2 gives a short overview of the Standard Model and explains concepts related to physics at hadron colliders that are needed in order to understand the analysis. The last section of the chapter focuses on details about top-quark physics, including a discussion about the possible production mechanisms, with an emphasis on the process targeted by this analysis.

A description of the LHC and the ATLAS detector (including information on particle identification) is given in chapter 3. The procedure used for reconstructing the physics objects is also presented. The data and the Monte Carlo simulated samples that are used for modelling the signal and background processes are described in chapter 4.

An important step in any particle physics analysis is the selection of events with a final state similar to the one resulting from the process of interest. This is done by applying cuts on the kinematic properties of the final-state objects. The first section of chapter 5 gives an overview of the possible final states of *tZq* production. This is followed by a summary of the cuts that are used for defining a region enriched in signal events. The remaining sections describe the methods used for evaluating the different sources of background as well as how these estimations are checked in dedicated validation regions.

Once the backgrounds are correctly estimated, an artificial neural network is used for separating signal and background and obtaining a single variable with high discrimination power. This is described in the first section of chapter 6. The sources of systematic uncertainties that need do be taken into account for the final cross section measurement are also presented. All these are combined in a binned likelihood fit used for extracting the measured signal strength; this procedure is explained in the last section of the chapter.

A discussion of the fit results obtained using both an Asimov dataset and the real data is included in chapter 7. The final chapter gives an overview of the analysis, as well as a short outlook of possible directions for future *tZq* analyses.

Theoretical concepts

The first part of this chapter has the role of setting the scene by reminding the reader of the basic content of the Standard Model (SM) of particle physics, as well as key concepts related to physics at hadron colliders. However, this is not a thorough review of these complex topics (this can be found in many sources such as [2] or [3]), but rather aims at offering the necessary information to understand the analysis presented in this thesis.

The second part of the chapter is related to the top quark. Its properties, decay mode and production mechanisms are discussed. This is based on in-depth reviews of top-quark physics, such as [4] and [5]. The final section focuses on the rare top-quark production mechanisms, such as associated production with heavy bosons.

2.1 The Standard Model in a nutshell

The Standard Model theory is the foundation of modern particle physics. Its role is to explain and predict elementary[1] particles, as well as their interactions.

There are two types of elementary particles that are included in the SM: these are fermions (also referred to as matter particles) and bosons (force carrier particles). An overview of how they are organised and their properties is given in figure 2.1. In addition to the content shown in this chart, each particle has a corresponding antiparticle that has the same mass and spin but opposite values for properties such as electric charge, lepton and baryon number, strangeness and parity[2]. The upper panel of the chart lists the three generations of fermions (consisting of six leptons and six quarks of different flavours) along with their electric charge, mass and allowed interaction type. The first generation consists of the lightest particles, the electron and its corresponding neutrino and the up and down quarks. At low energies, these particles constitute the building blocks of matter, with the up and down quarks being bound together and forming nucleons (two up-quarks and one down-quark for the proton and two down-quarks and one up-quark for the neutron). Electrons orbiting around this nucleus then complete the atom. However, when investigating higher energy scales, a more complex structure of the particle physics landscape emerges. In particular, two additional generations of particles with identical properties as the ones discussed

---

[1] In this context, the word elementary refers to particles that have no substructure (or at least not one that can be investigated with currently available experimental methods).

[2] Unless stated otherwise, in this thesis, referring to a particle type actually includes both the particle and its antiparticle (e.g. electrons means electrons and positrons).

above are revealed. The only difference between the three generations is the particle masses, with the 2nd and 3rd generation each being heavier versions of the previous one. So far, only three fermion generations were experimentally observed. This is also supported by electroweak results from the LEP Collaboration that measure the number of light neutrino species to be $N_\nu = 2.9841 \pm 0.0083$ [6].

Additional to the matter content of the SM, three different interactions are included. These are the strong, weak and electromagnetic interactions and some of their properties are listed in the bottom panel of figure 2.1. Each of these forces is mediated by spin 1 particles called gauge bosons and is described by a quantum field theory (QFT). In QFTs, particles can be understood as excitations of a field that satisfies a set of field equations. All information about the dynamics of the fields involved is encompassed in the Lagrangian density.

Leptons					Quarks			
	Particle	Q	Mass	Interaction	Particle	Q	Mass	Interaction
First generation	electron (e^-)	-1	0.511 MeV		down (d)	-1/3	4.7 MeV	
	neutrino (ν_e)	0	< 2 eV		up (u)	+2/3	2.2 MeV	
Second generation	muon (μ^-)	-1	105.7 MeV		strange (s)	-1/3	96 MeV	
	neutrino (ν_μ)	0	< 2 eV		charm (c)	+2/3	1.28 GeV	
Third generation	tau (τ)	-1	1776.9 MeV		bottom (b)	-1/3	4.18 GeV	
	neutrino (ν_τ)	0	< 2 eV		top (t)	+2/3	173.1 GeV	

Interaction	Boson	Strength	Spin	Mass	Higgs boson
Strong	Gluon (g)	1	1	0	
Weak	W boson ($W^\pm$) Z boson (Z^0)	10^{-8}	1	80.4 GeV 91.2 GeV	Mass 125.1 GeV Spin 0
Electromagnetism	photon (γ)	10^{-3}	1	0	

Figure 2.1: Overview of the elementary particles and their interactions. Structure inspired from [3]. The particle masses are taken from [7]. The type of interaction that each particle participates in is indicated by the respective colour of that interaction. Particles interacting with the Higgs field are marked by the orange dotted line.

The electromagnetic interaction is mediated by the photon and described by Quantum Electrodynamics (QED). This type of interaction occurs between any electrically charged particles and, among other things, it is responsible for keeping electrons orbiting around the nucleus.

The weak force, responsible for the β decay, is mediated by the W and Z bosons. This acts on all matter particles, including neutrinos. The weak and electromagnetic interactions are unified in the SM and are described by a $SU(2)_L \times U(1)_Y$ gauge symmetry. The index L is related to the fact that the weak isospin doublets are composed of left-handed particle and right-handed antiparticle states. The Y stands for the weak hypercharge[3].

The strong interaction is responsible for keeping quarks bound inside the proton or neutron. This is mediated by gluons and described in Quantum Chromodynamics (QCD). Gluons are electrically neutral

---

[3] The hypercharge is related to the electric charge and isospin through the Gell-Mann-Nishijima formula: $Q = I_3 + \frac{1}{2}Y$.

particles that carry colour charge. The strong force is responsible for quark interactions, each quark carrying one of the three possible colours (red, green, blue) or the anticolour. Bound quark states, called hadrons, must be colour neutral and hence consist of two quarks of opposite colour charge or three quarks of different colours. The strong interaction is characterised by the $SU(3)_C$ gauge symmetry.

The gravitational force is not included in the SM and generally it is not discussed in particle physics since its effect at this level is extremely small and can be neglected. At these scales, its coupling strength is of the order 10^{-37}.

The most recently discovered particle in the SM (that is also the only spin 0 boson) is the Higgs boson. This is a fundamental piece of the SM and can be understood as an excitation of the Higgs field. The Higgs mechanism is responsible for the W and Z bosons acquiring mass through the breaking of the $SU(2)_L \times U(1)_Y$ symmetry with a vacuum expectation value that is non-zero. Additionally, through gauge-invariant Yukawa interactions of the Higgs field with the fermion fields, the masses of the fermions can be generated as well. The coupling constants for these interactions are proportional to the masses of the respective fermions.

Another interesting related aspect appears in the flavour changing weak interaction. This occurs through the exchange of a W boson. The mass eigenstates are found to be different from the weak eigenstates (i.e. they are mixed in weak decays). The unitary transformation describing that mixing for the three generations of fermions is given by a 3×3 unitary matrix called the Cabbibo-Kobayashi-Maskawa (CKM) matrix [7]. This has in total 4 free, independent parameters that can be counted as three mixing angles and a complex phase. In the SM, the complex phase accommodates CP violation. The relation between the weak (q') and mass (q) eigenstates is shown below:

$$\begin{pmatrix} d' \\ s' \\ b' \end{pmatrix} = V_{\text{CKM}} \times \begin{pmatrix} d \\ s \\ b \end{pmatrix}.$$

Every element of the quark-mixing matrix, V_{ij}, describes the probability of a transition between quarks i and j. Each of these elements can be measured independently and represents a fundamental parameter of the SM. The experimentally measured values of the CKM matrix parameters are shown below [7]. The errors on the CKM element values were omitted for easier readability but they are all below 10%.

$$V_{\text{CKM}} = \begin{pmatrix} V_{ud} & V_{us} & V_{ub} \\ V_{cd} & V_{cs} & V_{cb} \\ V_{td} & V_{ts} & V_{tb} \end{pmatrix} = \begin{pmatrix} 0.97417 & 0.2248 & 0.00409 \\ 0.220 & 0.995 & 0.0405 \\ 0.0082 & 0.040 & 1.009 \end{pmatrix}$$

So far, all experimental observations are in agreement with the SM expectations, showing no clear signs of physics beyond the Standard Model (BSM). However, there are still many open questions that the SM does not provide an explanation for. One of these is related to the existence of a scale at which all three fundamental interactions unify. Another open issue is the so-called "hierarchy problem". This is related to the scale at which electroweak symmetry breaking occurs. In the SM, the expansion of the Higgs boson mass in perturbation theory includes contributions that are quadratically divergent. Without any additional solution, this results in large corrections to the mass due to the very high reference scale (for example the Plank scale). This can be solved either by considering a new symmetry or by fine tuning the size of the tree-level and loop contributions. Another shortcoming of the SM is the failure of providing a candidate for dark matter. In the current understanding of the universe, dark matter takes up to 25 % of all energy but there is no clear indication of what that is made of. Several BSM extensions offer dark matter candidates, but so far experimental searches did not have any conclusive results on the

subject.

From a cosmological standpoint, other examples of shortcomings of the SM are the fact that it is missing an explanation for the observed matter antimatter asymmetry in the universe and it also does not offer a quantum theory of gravity [8].

2.2 Physics at hadron colliders

Relating theoretical concepts to experimental observations is a crucial step in the validation of SM predictions. In order to gain access to information at the most fundamental level, collecting data at very high energies is necessary. One of the possible ways in which this can be achieved is through collisions of high energy beams of hadrons (e.g. at the Large Hadron Collider, which will be described in detail in chapter 3).

The following concepts and quantities related to physics at hadron colliders are repeatedly used throughout this thesis and hence, will be explained in detail in the following sections.

2.2.1 Hard scattering, factorisation and cross-sections

One of the most important quantities in particle physics is the cross-section. For any given process, this is related to the quantum mechanical probability of that interaction. It represents a link between theory prediction and what can be experimentally measured. More precisely, cross-sections of different SM processes are theoretically calculated and then compared to the values obtained by experimentalists, from determining how often this final state appears in the observed data (e.g. from hadron collisions). It is therefore very important to understand how the interaction takes place and how the cross-sections for different processes can be calculated.

In QCD, although the name would suggest otherwise, the coupling constant shows a dependence on the scale at which the interaction takes place. For the strong coupling constant this is a logarithmic decrease that can be written as $\alpha_S(Q^2) = \frac{1}{\ln(Q^2/\Lambda^2)}$, where Q is the momentum scale, while Λ is the QCD scale and is approximately $200\,\text{MeV}$.

This QCD feature that allows the interaction between particles to become weaker when the energy scale increases is called asymptotic freedom. Because of that, at lower energy scales the coupling becomes very strong, explaining the confinement of quarks and gluons inside hadrons. In theoretical predictions for processes that occur at a very high energy scales, one can rely on the fact that the strong coupling constant, α_S, becomes very small due to gluon self-interaction causing the anti-screening of colour charges. With $\alpha_S \ll 1$, a perturbative expansion can be applied, offering a good description of the hard scattering process.

In hadron collisions, the initial protons are an incoherent sum of partons[4]. The scale of the interactions occurring inside the hadron is soft, thus yielding a large α_S and falling into the non-perturbative regime. Each parton, i, inside the proton carries a longitudinal momentum fraction, $x_i = p_i/p_{\text{total}}$. The probability density function for a parton to have momentum fraction x, at a given momentum scale Q^2, is called the parton density function (PDF). These can be extracted by analysing data from deep inelastic lepton-nucleon scattering and hadron induced hard-scattering processes [9].

One of the main features of QCD (and a very useful tool for hard-scattering calculations) is factorisation. This property allows the separation of dynamics occurring at different energy scales. In particular,

---

[4] Partons are pointlike constituents of hadrons (quarks or gluons).

when writing the cross-section for a $pp \to X$ process, this becomes:

$$\sigma_{pp\to X} = \sum_{ijk} \int \mathrm{d}x_1 \, \mathrm{d}x_2 \, \mathrm{d}z f_i(x_1, \mu) f_j(x_2, \mu) \times \sigma_{ij\to k}(x_1, \ x_2, \ z, \ Q^2, \ \alpha_s(\mu), \ \mu) D_{k\to X}(z, \mu),$$

where the first part is related to the non-perturbative part of the process and includes the parton distributions functions $f_{i/j}$, with i/j being a quark, anti-quark or gluon, for the interacting partons that carry longitudinal momentum fractions x_1 and x_2. The second part is given by the parton cross-section, $\sigma_{ij\to k}$. This can be calculated using perturbation theory in powers of α_S. The remaining function $D_{k\to X}$ is called the fragmentation function and links the perturbative partons that appear in the final state to the particles that are observed. The quantities included in the factorised cross-section show a dependence on two different scales. These are the renormalisation and factorisation scales and are typically set to $\mu_f = \mu_r = \mu$. In perturbation theory, the factorisation and renormalisation scales are introduced in order to regularize infrared and UV divergences. A complete discussion about this topic can be found in [10]. Since μ_f and μ_r are not intrinsic parameters of QCD, measurable cross-sections should not have a dependence on the chosen values of the factorisation and renormalisation scales.

For the perturbative calculation of $\sigma_{ij\to k}$ in α_S, one can define different levels of accuracy. For example, if the calculation is done with the smallest power of the α_S coupling possible for the considered process, the calculation will be performed at leading order (LO). The calculation considering one α_S power beyond LO is next-to-leading order (NLO), and so on.

2.2.2 Collisions and particle decays

Centre-of-mass energy

The total energy available in the centre-of-mass system, $\sqrt{s}$, is defined as:

$$\sqrt{s} = \sqrt{(\sum_{i=1}^{2} E_i)^2 - (\sum_{i=1}^{2} p_i)^2},$$

where E_i and p_i are the energy and momentum of the two initial-state particles.

In the case of fixed target experiments this can be approximated to $s = 2m_b E_a$, where m_b is the mass of the target particle and E_a is the energy of the incoming particle. For symmetric, colliding beams, the formula reduces to $\sqrt{s} = 2E_{\mathrm{beam}}$. Both approximations are valid if the energy of the projectile (or particle beam) is much higher than the rest mass of the particles involved in the interaction.

Luminosity

Luminosity is a quantity that measures the ability of a particle accelerator to produce a certain number of interactions. For colliding beams with Gaussian beam profiles, one can define the instantaneous luminosity as:

$$L = f \frac{n_1 n_2}{4\pi \sigma_x \sigma_y}$$

where $n_{1/2}$ are the number of particles in each of the bunches colliding with a frequency f and $\sigma_{x/y}$ are the horizontal and vertical beam sizes.

More often mentioned in this thesis however is the integrated luminosity over a considered period of time of machine operation. This is an important quantity because it can be used to calculate the number

of interactions, N, for a process with cross-section, σ, via:

$$N = \sigma \int \mathcal{L}(t)\mathrm{d}t.$$

Decay width and branching ratios

The total decay width of a particle is defined as $\Gamma = \frac{\hbar}{\tau}$, where τ is the lifetime of the particle. For a particle that can decay into different final states (also called decay modes), the total decay width can be written as the sum of the partial widths of all possible decay modes.

The branching ratio is then defined as the fraction of times the particle will decay to a particular final state i: $\mathrm{BR}_i = \Gamma_i/\Gamma_{\mathrm{total}}$.

2.2.3 Kinematics

The following quantities related to the kinematics of high-energy collisions are described in a typical coordinate system in which the z-axis is along the beam line and the $x - y$ plane is perpendicular to the beam and is usually referred to as the transverse plane. The polar angle, θ, is measured around the z-axis. A more detailed description of the ATLAS coordinate system is given in section 3.2.

Rapidity and preudorapidity

For a hadron collider such as the LHC, the centre-of-mass system of the proton–proton system is considered. Because of the difference in longitudinal momentum of the two interacting partons, a boost of the final state objects in the longitudinal direction[5] can occur. It is therefore useful to consider quantities that are invariant under longitudinal boost. The rapidity of a particle gives information about its angular coordinates. It is defined as

$$y = \frac{1}{2} \ln\left(\frac{E + p_z}{E - p_z}\right),$$

where E is the measured energy of the particle and p_z is the particle momentum along the beam axis. Rapidity differences are invariant under Lorentz transformations along the z-axis.

More commonly however, instead of using y, a quantity called pseudorapidity is used. This is defined as

$$\eta = -\ln\left(\tan\frac{\theta}{2}\right),$$

with θ being the polar angle between the particle and the beam axis. At high energies ($E \gg M$), the rapidity and pseudorapidity become equal.

Missing transverse momentum

In order to gain information about the momentum and direction of particles that do not interact with the detector (such as neutrinos), conservation of momentum can be used. Because the momentum component in the longitudinal direction is unknown for the incoming partons, only the transverse component can offer a constraint. This is defined as $p_T = \sqrt{p_x^2 + p_y^2}$. Since the total p_T of the initial state is 0, the vectorial sum of all transverse momenta of the final state particles should also add up to 0. The missing

---

[5] The longitudinal direction is considered along the z-axis.

transverse momentum is defined as

$$\vec{E}_T^{\,\text{miss}} = -\sum_i \vec{p}_T^{\,i},$$

where the index i goes over all visible particles. The most common notation is E_T^{miss}, implying that the transverse momentum and transverse energy are equal; this assumption is valid for particles that are massless.

2.3 Top-quark physics

In 1973, in order to explain CP violation in kaon decays, Kobayashi and Maskawa postulated the existence of a third generation of quarks (the top and bottom quarks). Motivated by the GIM mechanism and further supported by the discovery of a third generation lepton (the tau lepton discovered in 1974) breaking the symmetry between the number of quark and lepton generations, the existence of two heavier quarks was widely accepted. The b-quark was discovered soon after, in 1977, and afterwards the searches focused on finding the last missing matter particle. In 1991, a lower bound for the top quark mass was set by the CDF collaboration to 91 GeV [11]. This was an important turning point since it was proving that the top quark is heavier than the W boson and therefore the production mode that was considered in the searches ($W \to \bar{b}t$) was actually not possible.

Finally, in 1995, both CDF and D0 collaborations published evidence of the discovery of the top quark in collisions registered at the Tevatron accelerator [12], [13]. The centre-of-mass energy for the collisions was $\sqrt{s} = 1.8$ TeV and the observation focused on events in which $t\bar{t}$ pairs are produced.

2.3.1 Top-quark properties

The basic properties of the top quark were already included in figure 2.1. It is part of a weak isospin doublet together with the b-quark and has spin $1/2$, charge $+2/3e$ and the third component of weak isospin $+1/2$. Its mass and decay width, however, make it unique among the SM particles and a very interesting and diverse study topic.

With a mass of 173.34 ± 0.76GeV[6] [14], it is the heaviest known elementary particle. Because of this, it has a strong coupling to the Higgs boson, offering insights into the scalar sector and adding constraints to the Higgs boson mass as well. Both the top quark and the Higgs boson play an important role in electroweak precision measurements due to their appearance in one-loop corrections to the W and Z masses.

Top quark decay width and lifetime

The decay of the top quark occurs via the electroweak charged current interaction, with the decay products being a W boson and a down-type quark. In the SM, the Lagrangian density related to this process is proportional to V_{tq}. This is the element of the CKM matrix responsible for transitions between the top quark and a lighter quark.

The total decay width of the top quark can be written at LO as:

$$\Gamma_t = \frac{G_F}{8\pi\sqrt{2}} m_t^3 \left(1 - \frac{m_W^2}{m_t^2}\right)\left(1 + 2\frac{m_W^2}{m_t^2}\right),$$

---

[6] This value is obtained from a combination of measurements performed by the CDF, D0 experiments at the Tevatron and ATLAS and CMS, at the LHC.

where G_F is the Fermi constant and m_W and m_t are the masses of the W boson and top quark respectively. The total width at LO is about 1.5 GeV. This can in turn be written as the sum of all partial decay widths as:

$$\Gamma_t = \sum_{q=d,s,b} \Gamma(t \to Wq),$$

in which the partial decay widths are proportional to the square of the corresponding CKM matrix element. From this, the branching ratio of $t \to Wb$ can be calculated as 0.998, meaning that the vast majority of top quarks will decay into a W boson and b quark.

Another distinct feature of the top quark is its lifetime. This can be calculated from the decay width and is 5×10^{-25} sec. This is faster than the typical hadronisation time (3×10^{-24} sec). The consequence of this is that the top quark does not form any bound states. Additionally, its spin state can be studied in detail via its decay products.

2.3.2 Top-quark production

Top-quark pair production

The most common mechanism for top quark production involves the creation of a top and anti-top quark pair in the final state through strong interaction. This can occur either via gluon–gluon fusion or $q\bar{q}$ annihilation. Feynman diagrams for these processes at LO in QCD are shown in figure 2.2. For the gluon induced process, the diagrams for both the t- and s-channel are included[7]. At LO the $t\bar{t}$ cross-section is proportional to α_S^2. The ratio of $q\bar{q}$ to gg induced processes depends on the centre-of-mass energy of the collisions and the PDFs of the interacting particles. In pp collisions at the LHC the dominant process is gluon-gluon fusion. For a 13 TeV centre-of-mass energy this accounts for roughly 90 % of $t\bar{t}$ events.
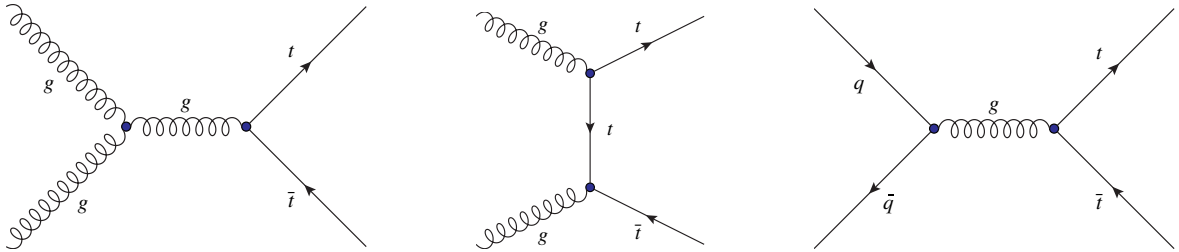
Figure 2.2: Feynman diagrams of the production of $t\bar{t}$ pairs at LO QCD.

At NLO, higher order corrections are applied to these processes by taking into account the real emission of gluons and virtual corrections. Other mixed channels such as qg or $\bar{q}g$ also become accessible.

$t\bar{t}$ pair production has been extensively studied, both at the Tevatron collider [15] and at the LHC [16].

Single top-quark production

Another way of producing top quarks at the LHC is through electroweak interaction. Three different processes can be defined based on the virtuality of the exchanged particle. The LO Feynman diagrams of these processes are shown in figure 2.3. The diagrams use the 5 flavour scheme (5FS), in which the

---

[7] s and t refer to the Mandelstam variables. These are kinematic variables that, for scattering processes, show the direction of the transfer of momentum by a virtual particle.

b quark in the initial state originates from flavour excitations inside the proton. In the 4 flavour scheme, (4FS), the *b* quark comes from the splitting of an initial-state gluon.

The dominant production mode occurs through the interaction of a *b* quark and a virtual *W* boson, resulting in the production of a top quark in the *t*-channel diagram shown on the left side of figure 2.3. This accounts for approximately 70% of the total electroweak production. The complete process can be written as $bq \rightarrow tq'$, where q' is the spectator quark. This plays a very significant part in the *t*-channel final state because it is predominantly emitted at a small polar angle. Experimentally, this process has been studied extensively at ATLAS, with fiducial, total and differential cross-section measurements performed at $\sqrt{s} = 8$ TeV [17], as well as fiducial and inclusive measurements published for $\sqrt{s} = 13$ TeV [18]. On the theoretical front, the process has been calculated differentially up to NNLO precision [19].
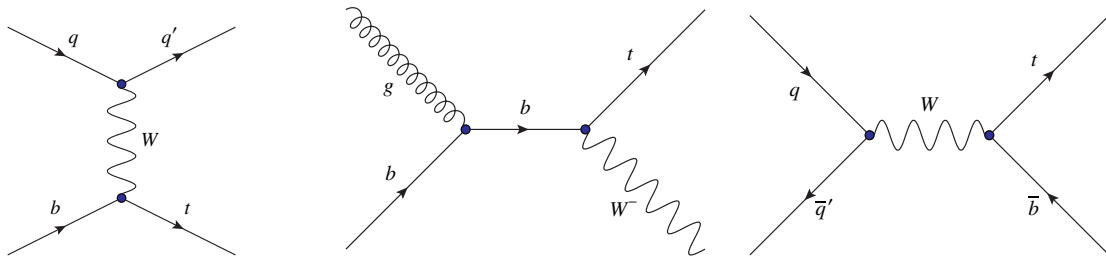
Figure 2.3: Feynman diagrams of single top-quark production at LO. The *t*-channel, *tW* and *s*−channel are shown from left to right.

The associated *tW* production has the second largest cross-section for electroweak top-quark production. In this case, a real *W* boson is produced in the final state. In the ATLAS collaboration, the associated production of a top quark and a *W* boson was first discovered by studying events in which both the top quark and the *W* boson decay into a final state involving leptons. This analysis was performed at $\sqrt{s} = 8$ TeV [20]. The cross-section was measured also at $\sqrt{s} = 13$ TeV [21] and currently the focus has shifted towards the measurement of differential cross-sections [22]. Searches for *tW* production in the single-lepton channel are also ongoing [23], [24]. The *tW* cross-section has been calculated up to approximate NNLO accuracy [25]. When including NLO corrections, the *tW* final state is the same as LO $t\bar{t}$ production. In Monte Carlo (MC) simulations, at generation level, this is handled by consistently removing this overlap [26].

The least common type of single top-quark production occurs through the exchange of a virtual *W* boson in an *s*-channel diagram. This process has been calculated up to approximate NNLO precision [27]. Evidence of *s*-channel production was first seen by the ATLAS collaboration at 8 TeV [28].

A summary of all single top-quark production cross-section measurements published by the ATLAS and CMS collaborations is shown in figure 2.4. The measured values are shown as a function of the centre-of-mass energies and are compared to the most accurate theoretical predictions available. Good agreement between the SM expectations and the measured cross-sections is observed.

2.3.3 Rare processes involving top quarks

As a result of the LHC progress in increasing both the luminosity and collision energy, the amount of collected data is large enough that processes with very low cross-sections become accessible for study. Many such processes involve top quarks. These include the associated production of a top-quark pair and an electroweak gauge boson (*Z* or *W*) and even a Higgs boson. The predicted NLO cross-sections at
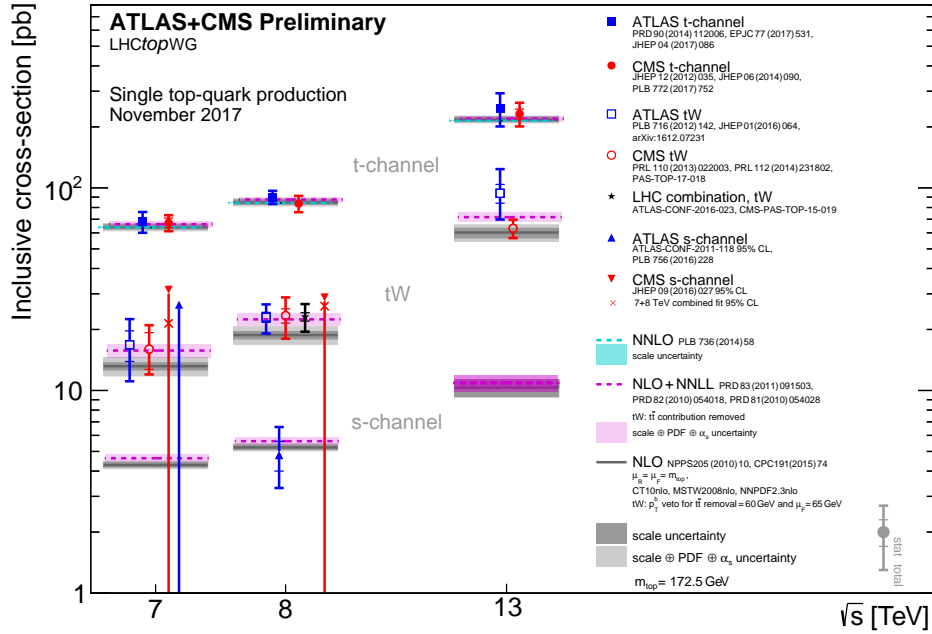
Figure 2.4: Summary of ATLAS and CMS measurements of the single top-quark production cross-sections as a function of the centre-of-mass energy compared to theoretical predictions [29].

13 TeV are below 1 pb. This is more than one order of magnitude lower compared to the smallest single top-quark production mechanism, *s*-channel production, as shown in figure 2.4.

Out of these processes, of particular interest is $t\bar{t}H$ production. This offers a direct way to investigate the top-Yukawa coupling. The observation of this process was very recently published by both ATLAS [30], [31] and CMS [32] collaborations. For a 13 TeV centre-of-mass energy, the $t\bar{t}H$ SM predicted cross-section, calculated at NLO accuracy, is 507^{+35}_{-50} fb [33]. The cross-section measured by the ATLAS collaboration with 79.8 fb^{-1} of data is $670 \pm 90(\text{stat.})^{+110}_{-100}(\text{syst.})$ fb, for a Higgs boson with mass $m_H = 125.0 \pm 0.21(\text{stat.}) \pm 0.11(\text{syst.})$ GeV [34]. The CMS result, obtained using datasets at centre of mass energies of $\sqrt{s} = 7, 8$ and 13 TeV with a total integrated luminosity of 60.7 fb^{-1}, yields a ratio between measurement and prediction of $1.26^{0.31}_{-0.26}$. Both result are in agreement with the SM predictions. The observed (expected) significance of the results is 5.8 (4.9) σ for ATLAS and 5.2 (4.2) σ for CMS, thus constituting the first observation of this process.

With even lower cross-sections, the associated production of a single top-quark and a Z [35] or H boson [36] can be investigated. The study of *tHq* events is very interesting because it gives information about the absolute value of the Yukawa coupling (similar to *ttH*) , but also about the relative sign of the top-Yukawa coupling with respect to the Higgs coupling to vector bosons. So far, only limits on the *tHq* production cross-sections have been published [37].

A study of *tZq* production can be seen as a precursor of a *tHq* analysis, given the possible similarities of the final state (depending on the considered decay chain) but it is also interesting in itself since it probes different couplings. This process will be discussed in more detail in the following subsection since it constitutes the subject of this thesis.

A similar final state as *tZq* production can result through the flavour changing neutral current (FCNC) of a *u* or *c* quark to the top quark with *Z* boson radiation. Such diagrams are forbidden at tree level and highly suppressed at higher orders. Some BSM theories like R-parity-violating supersymmetry or top-colour assisted technicolor models, predict an enhanced FCNC branching ratio. This makes *tZ*

events good candidates for such BSM searches because they offer access to *tqg* and *tqZ* anomalous couplings [38]. So far, the CMS collaboration has performed a search for *tZ*-FCNC production using 8 TeV data [39] but no sign of BSM effects was observed.

Associated *tZq* production

The associated production of a top quark and a *Z* boson occurs via the electroweak interaction through the *t*-channel diagram. The *Z* boson can be radiated from any of the quark lines or from the exchanged *W* boson, as shown in figure 2.5. The illustrated Feynman diagrams are at LO and are in the 4-flavour scheme. A top quark is produced through processes such as $u + b \rightarrow d + t + Z$ or $\bar{d} + b \rightarrow \bar{u} + t + Z$, while the anti-top quark appears via the charge conjugated processes. Less frequently, *tZq* production can be initiated by strange or charm quarks. The cross-section ratio $\sigma(tZq)/\sigma(\bar{t}Zq)$ should be approximately equal to 2, due to the difference in the parton distribution functions of the *u* and *d* quark at the typical *x* values relevant for this process.

A *tZq* production measurement is complementary to its QCD induced counterpart in which a *Z* boson is produced in association with a $t\bar{t}$ pair. $t\bar{t}Z$ production has a slightly larger predicted cross-section, $\sigma_{t\bar{t}Z} = 840$ fb and probes the top-quark's neutral-current coupling. This process has been investigated so far at $\sqrt{s} = 13$ TeV by both ATLAS [40] and CMS [41].

As can be seen from figure 2.5, *tZq* production offers access to the coupling of the top quark to a *Z* boson and additionally to the *WWZ* coupling. Measuring this process is therefore a very interesting test of the SM, since the production rate could be modified by several BSM theories (e.g. in vector-like quark models).
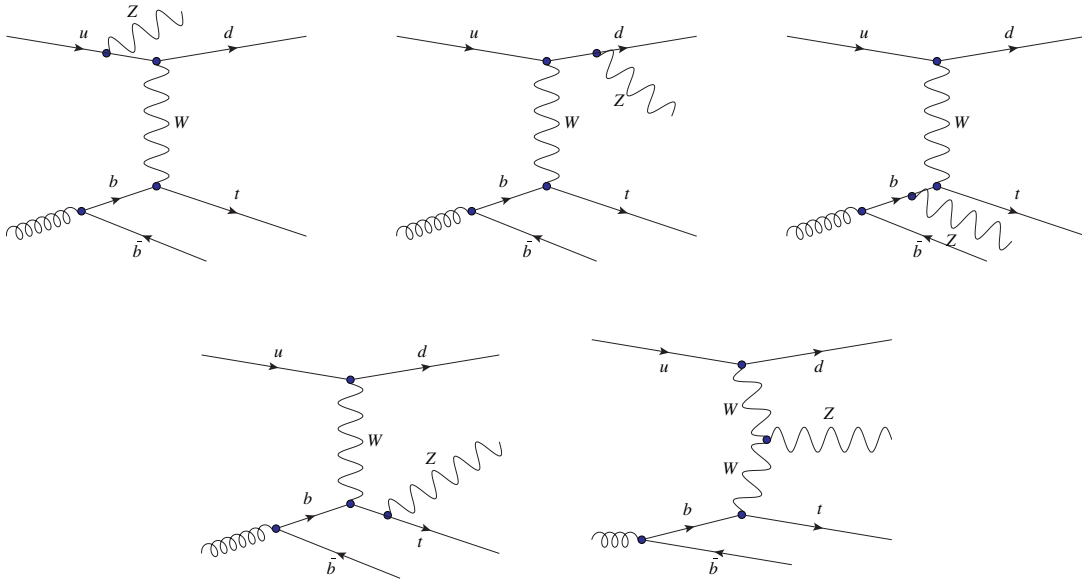
Figure 2.5: LO Feynman diagrams of *tZq* production in the 4-flavour scheme.

The first search for SM *tZq* production was performed by the CMS collaboration at 8 TeV [39] and resulted in a measured cross section of 10^{+8}_{-7} fb with a signal significance of 2.4σ.

The first evidence for associated *tZq* production was reported by the ATLAS collaboration at 13 TeV [1] and represents the focus of this thesis. The measured cross-section is 600 ± 170 stat. $\pm$ 140 syst. fb, with an observed (expected) significance of 4.2σ ($5.4\ \sigma$). The result is in agreement with the SM

cross-section calculated at NLO, $800^{+6.1}_{-7.4}\%$ fb. The calculation is done using MADGRAPH 5.3.3 with the NNPDF3.0_NLO_AS_0118 [42] PDF.

At 13 TeV, the CMS collaboration reports a measured cross-section of 123^{+44}_{-39} fb for the $pp \rightarrow tZq \rightarrow t\ell^+\ell^- q$ [43]. The observed significance of the result is 3.7σ. This result is compatible within the uncertainties with the SM predictions and when extrapolated to the total cross-section, it is compatible with the ATLAS measurement.

The LHC and the ATLAS experiment

In order to study processes that have a probability of production dependent on the collision energy, data with variable centre-of-mass energy is needed. Additionally, studying processes that are very rare requires a large amount of data. Tha Large Hadron Collider (LHC) fulfils both these conditions by so far delivering over $120\,\mathrm{fb}^{-1}$ of proton–proton (pp) collision data at 7, 8 and 13 TeV centre-of-mass energy.

The dataset used in the analysis presented in this thesis was collected by the ATLAS detector at the Large Hadron Collider (LHC) [44] during its 2015-2016 operation. This consists of $36.1\,\mathrm{fb}^{-1}$ of pp collision data.

This chapter includes a general overview of the LHC and a detailed description of the ATLAS detector and its subcomponents. The last section summarises how different physics objects are reconstructed in ATLAS, along with their associated calibration procedure.

3.1 The Large Hadron Collider

The European Organization for Nuclear Research (CERN) has been at the forefront of high energy particle physics research ever since being established in 1954. Since then, it has housed a large number of accelerators and experiments. Ideas regarding the design of a pp accelerator that would reuse the tunnel housing the Large Electron Positron (LEP) collider were first discussed as early as the 1980s. However, it was not until 2008 that the LHC first started its operation.

The LHC is a circular accelerator in which protons (or lead ions) collide at energies up to 13 TeV (1150 TeV). The machine has a 26.7 km circumference and is located at a mean depth of 100 m below ground, at the Swiss-French border, close to Geneva.

In order to accelerate the protons up to the highest energies, the LHC is the last in a chain of smaller accelerators that are meant to gradually increase the energy of the particles. A schematic view of the full accelerator complex is shown in figure 3.1. The protons are obtained by stripping electrons from hydrogen atoms. From the proton source the particles enter a linear accelerator (LINAC 2) and three circular ones (the Proton Synchrotron Booster, the Proton Synchrotron and the Super Proton Synchrotron), with their energy increasing up to 50 MeV, 1.4 GeV, 25 GeV and 450 GeV respectively. Once they have passed this threshold energy of 450 GeV, the particles are injected into the LHC ring in bunches. There, they circulate in a vacuum tube where they can be manipulated by electromagnetic devices. In order to keep the beams following a circular orbit, dipole magnets are used. These are designed to create a 8.3 T magnetic field over their full 15 m length. Quadrupole magnets are used for focusing the beams, while

the acceleration is done via accelerating cavities and electromagnetic resonators. Both the dipole magnets and the super-conducting cavities operate at very low temperature (below 5 K), requiring a complex cooling system using liquid helium. After about 25 minutes of acceleration that allows them to reach the 6.5 GeV target energy, the proton beams circulate in the accelerator for about ten hours, after which the beam is dumped.

The two beams rotate in opposite directions inside separate beam pipes along the LHC ring and circulate with a interbeam distance of 195 mm, intersecting only inside the four large experiment that are located along the machine.

The LHC data-taking periods so far are referred to as Run 1, that lasted between 2008 and 2012 and in which centre-of-mass energies of 7 and 8 TeV were reached, and Run 2 (that started in 2015 and is currently ongoing), in which the centre-of-mass energy reached 13 TeV. Approximately 25 fb^{-1} of data were delivered by the LHC during Run 1 and around 100 fb^{-1} more are expected to be recorded in Run 2. Unless stated otherwise, all the information given in this thesis refers to the Run 2 operations, specifically the 2015-2016 period, as the data used for the analysis was collected under these conditions.

The main differences between the two operation periods was the increase in energy to 6.5 TeV per beam. The number of bunches per beam was 2220 for most of the 2016 data-taking. Additionally, the spacing between the particle bunches went from 50 ns to 25 ns. A record instantaneous luminosity of $1.5 \times 10^{34} \, \mathrm{cm}^{-2}\mathrm{s}^{-1}$ was achieved.

As already mentioned, there are four main experiments operating at the interaction points of the colliding beams circulating in the LHC. The exact location of these experiments on the ring is marked on figure 3.1. Two of them, ATLAS [45] and CMS [46], are general purpose detectors that allow for the study of a wide range of topics related to elementary particles and their interaction, as well as searches for signs of new physics. The LHCb [47] experiment focuses on *b* physics and studies charge-parity violation by looking at the decays of *B* hadrons and ALICE[48] is dedicated to the study of data resulting from heavy ion collisions.

3.2 The ATLAS detector

When collisions occur at the LHC, individual interactions (referred to as events) take place. These result in the production of highly energetic particles that must be detected and identified. This is the task of large general purpose particle detectors, such as ATLAS.

The name of the detector, ATLAS, stands for "A Toroidal LHC Apparatus" and refers to probably the most recognizable component of the detector, the toroidal magnets that are part of the muon detection system. The detector is 46 m long and has a 25 m diameter. Its total weight is 7000 t. The ATLAS structure is typical for a general purpose particle physics detector, with the interaction point directly surrounded by tracking detectors, followed by calorimeters and a muon detection system. Each of these subcomponents can be seen in figure 3.2 and will be described in more detail in the following subsections. The detectors closest to the beam pipe, responsible for recording and reconstructing particle tracks, are the Pixel Detector (PD), the Semi-Conductor Tracker (SCT) and the Transition Radiation Tracker (TRT). These are part of the Inner Detector (ID). Following the ID, the electromagnetic and hadron calorimeters (ECAL and HCAL) have the role of measuring the energies of particles interacting with the detector. The largest volume of the detector is occupied by the Muon Spectrometer (MS).

Coordinate system

In this thesis, the standard ATLAS coordinate system definition is used. This defines the nominal interaction point as the origin, the *z*-axis along the beam line and the $x - y$ plane transverse to the *z*-axis
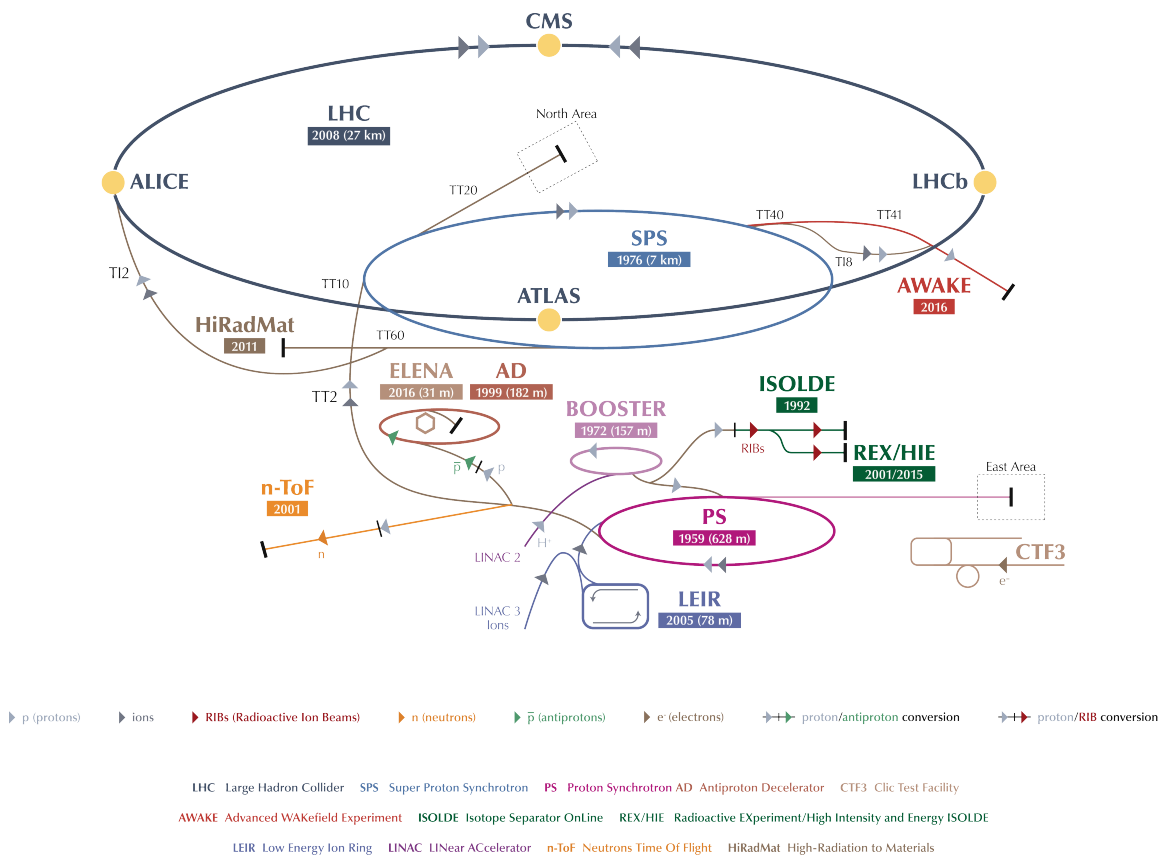
Figure 3.1: The CERN accelerator complex. [49]
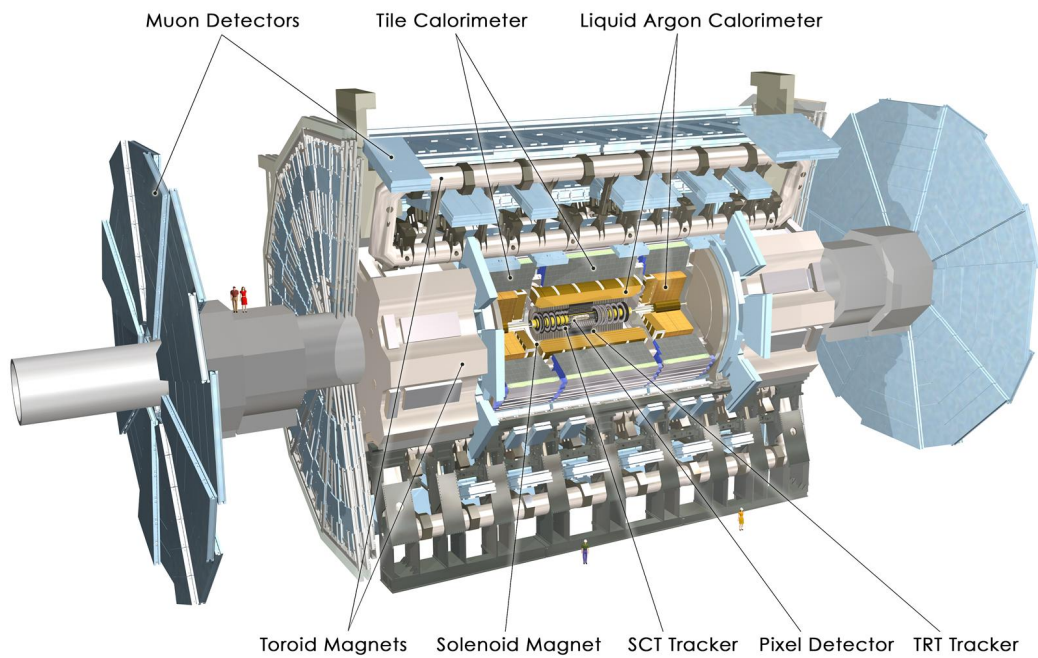
Figure 3.2: Overview of the ATLAS detector. [50]

(with the positive *x*-axis pointing towards the centre of the LHC ring and the positive *y*-axis pointing upwards). The polar angle, denoted with θ, is defined as the angle measured with respect to the beam axis. This angle was already mentioned in the definition of pseudorapidity, η, in section 2.2.3. The azimuthal angle, measured around the *z*-axis is denoted with ϕ. The plane defined by η and ϕ is commonly used for measuring distances. These are denoted by ΔR and can be calculated as $\Delta R = \sqrt{\Delta\eta^2 + \Delta\phi^2}$.

3.2.1 Inner detector

The role of the ID is to measure the momentum, direction and electric charge of all electrically charged particles passing through the detector[1], as well as reconstruct the point where the hard interaction occurred. In order to achieve this, the inner detector is surrounded by a magnetic field that is parallel to the beam axis. A schematic view of this system can be seen in figure 3.3. The tracking capabilities of this detector extend up to $|\eta| = 2.5$. All of the subdetectors have a similar structure: one cylindrical component with the length parallel to the beam line and covering the central part of the detector (referred to as the "barrel") and two components, one on each side of the detector, that are meant to detect particles travelling at high η, named endcaps.

The design transverse momentum resolution for the inner detector in the transverse plane is: $\sigma_{p_T}/p_T = 0.05\% \times p_T[\text{GeV}] \oplus 1\%$ [45].
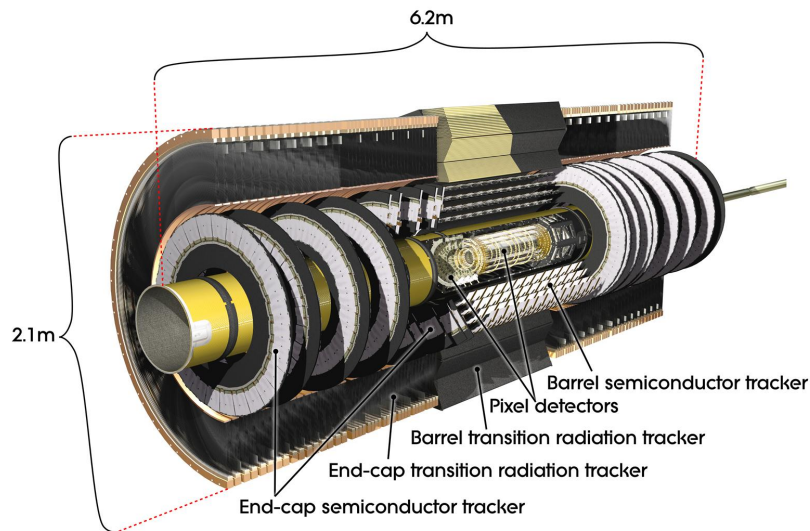
Figure 3.3: Schematic view of the inner part of the ATLAS detector. [51]

Pixel detector

Pixel detectors are used in the innermost layers of the detector because they offer the best accuracy in identifying signals in very dense environments, as it is the case in close proximity of the interaction point. The working principle of such devices relies on the property of a charged particle to induce a charge in the semiconductor medium due to ionisation. The ATLAS pixel detector uses silicon sensors.

The pixel detector consists of four barrel layers and three endcap disks. The initial setup only had three barrel layers but as of 2015, an additional Insertable B-Layer (IBL) was added. This new pixel

---

[1] For muons, the information from the ID is used along with input from the muon spectrometer.

layer is located only 3.3 cm from the beam pipe. It was designed to maintain (and potentially improve) the tracking and vertexing performance of the ATLAS pixel detector during Run 2 operations.

Each of these layers consists of rectangularly shaped modules (1546 in the central region and 288 in the endcaps). All modules are approximately 6 cm × 2 cm and consist of 46 080 pixels. The size of each individual pixel is $50 \times 400\,\mu m^2$ and each of them is read out independently, totalling over 92 million readout channels.

When particles pass any of these layers, *hits* are recorded. These 3-dimensional space points are then used to reconstruct the trajectory of the particles, as well as identify the primary point of interaction. During Run 1, the pixel detector had a tracking efficiency of approximately 99% and a spatial resolution of 8 μm in $r - \phi$ and 75 μm in z [52]. Similar performance is achieved during the Run 2 operation.

Semi-conductor tracker

The SCT is a silicon microstrip detector located immediately around the pixel detector. Its structure includes 4 cylindrical barrel layers and 18 planar endcap disks. These are composed of 4088 modules (2112 in the barrel and 988 in each endcap). Every module is made of four silicon strip sensors. The total area covered by the silicon is roughly $60\,m^2$ and the readout is done using over 6 million readout strips (distributed with a 80 μm spacing for the barrel region and between 70 and 90 μm in the endcaps). The position measurement of electrically charged particles is done with a precision of up to 17 μm, in the direction transverse to the strips.

Both in the endcap and barrel region, each layer will yield two strip measurements since the sensors are positioned back to back and rotated by a 40-milliradian stereo angle from each other [53]. The two measurements are combined into a space point. When passing through the detector (from the interaction point), typically 4 such hits will be identified by the SCT. On average, in Run 1, the intrinsic hit efficiency for the SCT has been (99.74 ± 0.04)% [54] and similar performance is observed during Run 2.

Transition radiation tracker

Due to its volume of approximately $12\,m^3$, the TRT is the largest subdetector of the ID. Its detector element consists of straw tubes that are 4 mm in diameter. Each straw is an individual drift chamber. The signal wires are made of gold-plated tungsten and have a 0.03 mm diameter. The barrel part of the detector consists of 50 000 straws, while the endcaps are composed of 250 000. The length of the straws is 144 cm in the central region and 39 cm in the endcap region.

Each of the straws is filled with a gas mixture (xenon or argon depending on the layer and region of the detector). Each particle crossing a gas-filled straw will cause ionisation. Due to the potential difference (the straw walls have high negative voltage), the primary electrons are accelerated towards the anode. An avalanche is created and the movement of charge carriers produces a current signal that can be detected. The readout of the wires is done at both ends of the straw.

In addition to its capability to provide space points for track reconstruction (typically more than 30 hits per track), the TRT plays a role in particle identification as well. Polymer fibers and foils fill the space between the drift tubes in order to create transition radiation[2]. For an electron, the probability of emitting such radiation is higher than for other charged particle, such as pions. This is valid over a large energy range, thus allowing one to differentiate between electrons and hadrons.

---

[2] Transition radiation is emitted when a charged particle crosses the boundary between two media with different dielectric constants.

3.2.2 Calorimeters

The role of the calorimeters is to measure the energy of highly energetic particles and to contribute to particle identification. The ECAL is responsible for measurements related to electrons and photons, while the HCAL measures the energies of hadronic showers. The ATLAS calorimeter system is shown in figure 3.4.
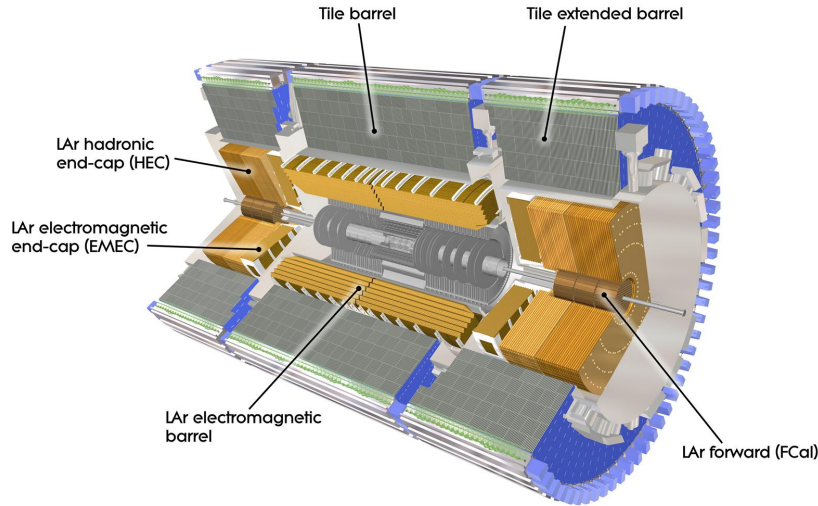
Figure 3.4: Schematic view of the ATLAS calorimeter system. [55]

The electromagnetic calorimeter

When a highly energetic electron passes through matter, it loses energy by radiating a photon in the electromagnetic field of the nuclei (bremsstrahlung). In the case of photons, the primary type of interaction (if $E_\gamma > 10\,\text{MeV}$) is electron pair production in the field of the nucleus. For either of the two cases, subsequent instances of bremsstrahlung and pair production occur when the particle (electron or photon) passes through matter. This is called an electromagnetic shower.

One of the quantities that characterises the interaction of electrons and photons in matter is the radiation length. This is denoted by X_0 and can be interpreted as the average distance that the particle travels until its energy decreases by $1/e$. X_0 is inverse proportional to the Z of the material in which the particle travels. It is therefore common to choose materials with high Z in order to minimise the size needed for the calorimeter to contain the electromagnetic shower. This happens once the energy of the particles in the shower falls below the threshold in which the particles start losing energy through ionisation rather than bremsstrahlung or pair production. The number of radiation lengths, x_{max}, after which the shower will have the maximum number of particles can be written as

$$x_{\text{max}} = \frac{\ln(E/E_C)}{\ln 2},$$

where E_C is the energy for which the loss through ionisation and bremsstrahlung becomes equal, referred to as critical energy, and E is the energy of the photon or electron.

The ATLAS ECAL is a so called sampling calorimeter, in which two materials alternate, one as an absorber and the other one as an active detection layer. The materials used are lead and liquid argon,

respectively. In terms of structure, the detector is composed of three parts. The central region, in the $|\eta| < 1.475$ range, is called the LAr electromagnetic barrel and two endcaps cover the forward region up to $\eta = 3.2$. The ECAL barrel has a thickness of approximately $22X_0$, while for the endcaps this is $26X_0$. In the central region, the layers closest to the centre of the detector have a higher granularity, with the first layer consisting of strips with $\Delta\eta \times \Delta\phi = 0.003 \times 0.1$. The design energy resolution (that was also validated using test beam results) in the central region is:

$$\frac{\sigma_E}{E} = \frac{10\%}{\sqrt{E}} \oplus 0.7\%.$$

The hadron calorimeter

When passing through matter, hadrons will lose energy via ionisation (or strong interaction with nuclei). A hadronic shower occurs when the particles created in the initial interaction also interact with the medium, creating more particles and thus starting a cascade of such events. The size of hadronic showers is larger than EM ones and hence, in order to completely contain them, HCALs usually occupy a larger volume in the detector.

The hadron calorimeter combines different materials and structures in order to provide reliable measurements of hadronically interacting particles. The Tile Calorimeter (TileCal) covers the central part ($|\eta| < 1.7$). It uses steel as absorber and plastic scintillating tiles as active material.

A LAr hadron endcap covers the $1.5 < |\eta| < 3.2$ region. This is a liquid argon calorimeter that uses copper as an absorber. Between $3.1 < |\eta| < 4.9$, the energy measurement is done by the high-density forward calorimeter (FCAL). This detector component is made of copper in the first layers (that is also responsible for catching EM showers) and for the outer layers tungsten is used.

The design jet energy resolution in the central region of the hadron calorimeter is:

$$\frac{\sigma_E}{E} = \frac{50\%}{\sqrt{E}} \oplus 3.0\%.$$

3.2.3 Muon spectrometer

Muons are the only particles (excluding neutrinos), that pass the ID and calorimeters without being stopped. The muon spectrometer is a tracking system that is designed to measure high p_T muons and also provides an independent muon trigger. It is composed of four subsections that use different technologies: Thin Gap Chambers (TGC), Resistive Plate Chambers (RPC), Monitored Drift Tubes (MDT) and Cathode Strip Chambers (CSC). The first two play a role in the triggering system, specifically RPCs in the barrel region and TGCs in the endcaps. The MDTs and CSCs are used for track and momentum measurement. This is possible because of the three superconducting air-core toroid magnets that are needed in order to deflect the muon tracks. All these components and their placement in the detector can be seen in figure 3.5.

The MDT is the component responsible for precisely measuring the muon momentum. It consists of 1171 chambers and 354 240 aluminium tubes with 30 mm diameter. The wires located at the centre of the drift tubes are made of tungsten-rhenium. The gas mixture used in the MDT chambers is Ar-CO_2. Each of the chambers consists of two parts with 4 or 3 monolayers of drift tubes in the inner or central and outer part of the detector respectively. The resolution of each multilayer piece is 50 µm.

Overall, the momentum resolution in the muon spectrometer is approximately 2 % to 3 % for most of the kinematic range. Around $p_T = 1$ TeV this worsens to 10 % [57].
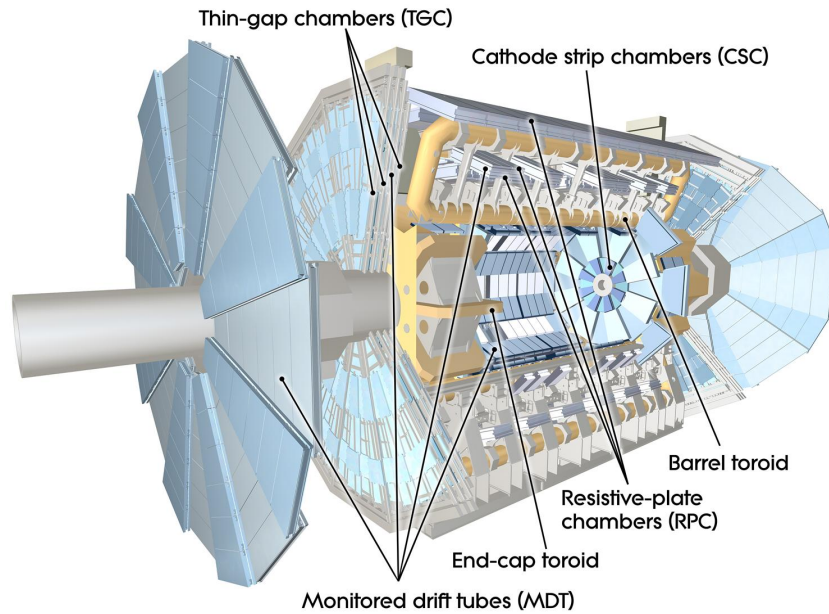
Figure 3.5: Schematic view of the ATLAS muon system [56].

3.2.4 Trigger and data acquisition system

With the high centre-of-mass energy and luminosity that the LHC operates at, the number of interactions that happen in a very short period of time is very high, making it impossible to store and process all the incoming data in real time. The trigger system is responsible for identifying "interesting" events that should be kept for offline analysis.

The trigger and data acquisition (TDAQ) system[3] is composed of two subcomponents: a first level trigger (L1), that is hardware based, and a high level trigger (HLT) that is based on software. The Level-1 trigger is responsible for a decrease in the event rate from 40 MHz to 100 kHz. It uses information from the muon detector, as well as the coarser layers of the calorimeters, for defining regions of interest (ROIs) in the detector that are then passed to the HLT. The decision for an event to pass or fail the Level-1 trigger is taken in 2.5 µs.

The HLT is responsible for reducing the event rate to 1 kHz. It takes as an input the regions of interest from the Level-1 system and uses information from the whole detector. Several algorithms process data from the ROIs or the whole event. The average decision time is 200 ms. After passing the HLT, events can be written in different data streams. For physics analysis, the data stream records full event information. Partial event information is recorded and used for monitoring, detector calibration or trigger level analysis [58].

3.3 Physics object reconstruction in ATLAS

In order to reconstruct high-level objects that can be associated to particles arising from the parton collision, input low-level objects must be first defined and identified. These are related to the particle trajectories, the position of the hard scattering interaction and energy depositions in the calorimeter.

---

[3] The trigger system has been updated in Run 2 in order to deal with the 5 times larger event rate compared to Run 1. The description presented only describes the Run 2 trigger system.

- **Tracks**

  The trajectories of charged particles in the detector are reconstructed using primarily information from the pixel and SCT detector. The TRT offers complementary information and allows the extension of the track reconstruction procedure up to a radius of 1082 mm within $|\eta| < 2.0$. The track finding algorithm used in Run 2 is described in detail in [59]. All reconstructed tracks must pass a set of quality criteria that include having p_T above 400 MeV and $|\eta| < 2.5$. Additionally, requirements related to the number of hits in the pixel and SCT must be met.

- **Primary vertex**

  In order to define the point where the hard interaction occurred, primary vertices are identified. The vertex reconstructing algorithm uses as input reconstructed tracks passing the quality criteria mentioned above. If several vertex candidates are found, the one with highest total $\sum p_T^2$ is identified as coming from the hard interaction. A detailed description of the vertex finding procedure can be found in [60].

- **Pile-up**

  Other inelastic pp collisions can occur. These are referred to as *pile-up* and give rise to additional vertices. Pile-up can be quantified either by specifying the number of reconstructed vertices in the event, denoted as N_{PV}, or by $\langle \mu \rangle$, the average number of additional interactions per bunch crossing. This is calculated as

  $$\mu = L_{\text{bunch}} \times \sigma_{\text{inel}} / f_r,$$

  where L_{bunch} is the instantaneous luminosity per bunch, σ_{inel} is the inelastic cross-section and f_r is the revolution frequency of the LHC. The inelastic pp cross-section at $\sqrt{s} = 13$ TeV is approximately 80 mb [61].

- **Topological clusters (Topo-clusters)**

  Topo-clusters are groups of calorimeter cells that are used for reconstructing signals from hadrons and jets. Identifying topo-clusters is useful for separating calorimeter signals from the relevant collision from noise or pile-up contributions. The topo-cluster identification starts from calorimeter cells (with signal measured at the EM scale[4]). Seed cells are chosen if the signal of the cell is at least 4 times larger than the expected average noise, $\sigma_{\text{noise,cell}}^{EM}$. The cells neighbouring the seed, either laterally or in depth, having a signal of at least two times $\sigma_{\text{noise,cell}}^{EM}$ will be added to the topo-cluster. This procedure is repeated until the cells no longer have any significant signal contribution. Neighbours are considered to be cells directly adjacent in a sampling layer of the calorimeter or cells located in an adjacent layer that overlap in the $\eta - \phi$ plane. After the cluster is built, if more than one maximum is found, the cluster is split accordingly [62].

The reconstruction of physics objects provides a link between the information recorded by all subdetectors and the final state particles produced in pp collisions. This analysis searches for events in which a top quark and a Z boson are produced; these lead to a final state possibly involving leptons (electrons or muons), jets and E_T^{miss}. This section explains how each of these objects are reconstructed and also any subsequent calibrations that they undergo. Calibration procedures are needed in order to relate signals from the detectors to fully corrected 4-momenta.

---

[4] The EM scale corresponds to the energy deposited by electromagnetically interacting particles.

3.3.1 Electrons

From the detector signals that indicate the production of an electron after a *pp* collision, to the final physics object that is used in the data analysis, several steps need to be performed. These are: electron reconstruction, identification, checking if the electron passes a dedicated trigger requirement, as well as verifying if it is isolated. A description for all four stages is provided below and more details can be found in [63–65].

Electron reconstruction and identification

The starting point for reconstructing an electron is to look for a *seed cluster* in the electromagnetic calorimeter. This is done using a sliding window algorithm that searches for a seed with $E_T > 2.5$ GeV. Regions of interest are defined using a cone with $\Delta R = 0.3$ around the seed cluster. Since the electrons are charged particles, they will also leave a signal in the tracking detector. Track seeds are found by searching for at least 3 hits in different layers of the silicon detectors. A track fit is then performed in order to extend the seed to a full track. This must be consistent with an electron track hypothesis (taking into account the energy loss due to interaction with detector material). Once electron track candidates are found, they are matched to the EM clusters. A match is found by selecting that pair with the smallest ΔR between the cluster barycentre and the extrapolated position of the track to the second layer of the calorimeter. The final four-momentum measurement includes the calorimeter information (energy of the cluster) and best matched track (direction).

An identification procedure is needed to distinguish electrons from other objects that might mimic the electron signature in the detector, such as hadron jets or converted photons. The electron identification is based on several variables related to the track–cluster matching, properties of the electron candidate in the different layers of the EM calorimeter, a likelihood variable based on TRT information and more. All the probability density functions of these variables are combined using multivariate analysis techniques in a likelihood-based (LH) discriminant that can be interpreted as the overall probability for the electron to be signal or background. This is the default identification technique used in Run 2.

Different operating points are defined for this method. These are *Loose, Medium* and *Tight* and differ in terms of background suppression and identification efficiency. For the *Tight* working point, an $|\eta|$- and p_T-dependent cut is applied on the LH discriminant in order to have 80 % efficiency. With this cut, a rejection factor of roughly 700 against jets for $p_T = 40$ GeV is achieved. The electron identification efficiency is compared in figure 3.6 for the three working points for a Monte Carlo generated sample of $Z \to ee$ events.

Electron isolation

The isolation of a physics object is related to the energy deposited by other particles in close proximity to the considered object. Checking if an electron is isolated helps with discriminating between prompt and non-prompt leptons. Prompt leptons originate from the decay of a W or Z boson or a τ lepton. Non-prompt leptons can result from photon conversion, heavy flavour hadron decays and even light-flavour hadrons that are misidentified as leptons. These are likely to not be spatially well separated from other energy depositions in the detector. Two variables, are used in order to check if an electron is isolated. The first one, $E_T^{\text{cone0.2}}$, checks for energy deposits in the calorimeter within a cone of $\Delta R = 0.2$ around the cluster associated to the electron. The second variable is track related and is denoted with $p_T^{\text{varcone0.2}}$. This is defined as the transverse momentum sum of all the tracks within a cone of $\Delta R = \min(0.2, 10\,\text{GeV}/E_T)$ around the electron track. Several isolation working points are defined, either for

fixed efficiency or as a function of E_T. In this thesis, electrons that pass the *Gradient* operating point are selected. The corresponding efficiencies are summarized in table 3.1.

Operating point	Calorimeter isolation	Track isolation	Total Efficiency
Gradient	$0.1143\% E_T + 92.14\%$	$0.1143\% E_T + 92.14\%$	$90/99\%$ at $25/60\,\mathrm{GeV}$

Table 3.1: Efficiency of the gradient operating point for electron isolation.

Electron trigger

When processing collision data, electron candidates are reconstructed at both the L1 and at the HLT level. The L1 trigger decision is based on the hadron and electromagnetic calorimeter information, while HLT triggers combine tracking and calorimeter information in order to identify potential electron objects. A likelihood identification was adopted for the HLT trigger in Run 2.

For any given trigger selection, a trigger efficiency can be defined as the ratio between the number of events selected by that trigger and the total number of reconstructed electrons. More details on the specific trigger requirement used for selecting electrons for this analysis are given in section 5.3.

Electron efficiency

The overall efficiency to identify and select an electron, $\epsilon_{\mathrm{electron}}$, can be written as:

$$\epsilon_{\mathrm{electron}} = \epsilon_{\mathrm{reconstruction}} \times \epsilon_{\mathrm{identification}} \times \epsilon_{\mathrm{isolation}} \times \epsilon_{\mathrm{trigger}}.$$

Each of the individual efficiencies is evaluated with respect to the step before. In order to properly simulate the data, MC samples are corrected to match the electron efficiency measured in data. This is done by looking at events coming from $Z \to ee$ and $J/\psi \to ee$ events and the factors are derived in bins of E_T and η of the electrons.

The reconstruction and identification efficiency, as well as the trigger efficiency are shown in figure 3.6. These are derived after selecting $Z \to ee$ events and are shown as a function of E_T. The values are integrated over the full η range.

3.3.2 Muons

Muon reconstruction relies on information from all tracking systems. Depending on how the ID and MS information is combined, different muon track candidates can be defined. For this analysis, the *combined* muons are used. These will be described in more detail below. Information on alternative muon reconstruction methods can be found in [67].

Muon reconstruction and identification

In order to reconstruct combined muons, track candidates found in the inner detector and the muon spectrometer are used as input. This is done by applying a global refitting procedure. In order to improve fit quality, MS hits can be either added or removed to the track candidate.

In the process of identifying muons, each track must satisfy a set of quality criteria in order to reduce the probability of the track to be produced by other particle decays, such as pions and kaons. The quality
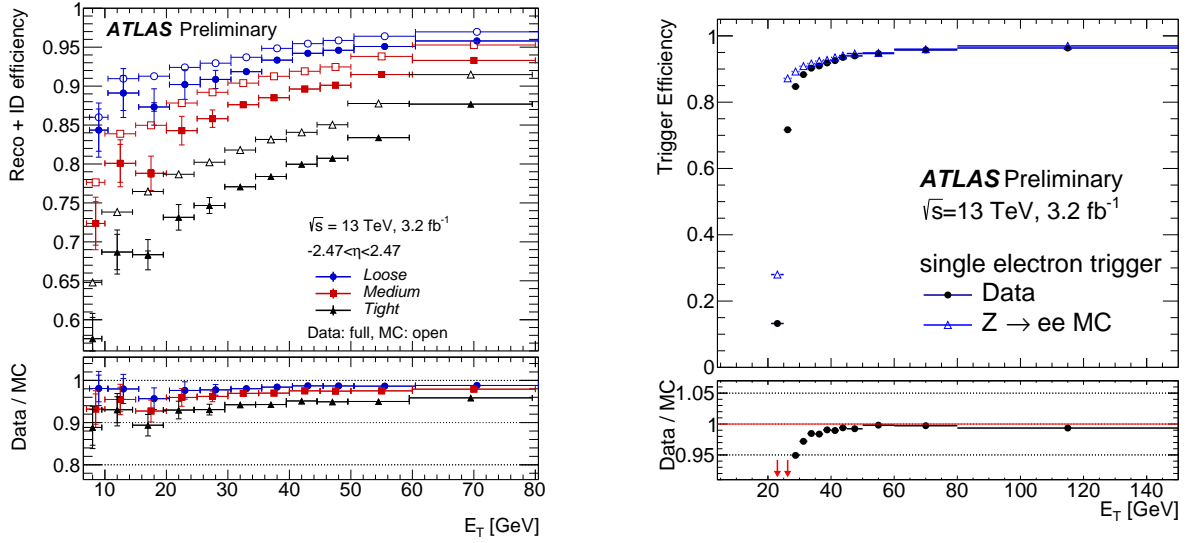
Figure 3.6: Combined electron reconstruction and identification efficiencies as a function of the transverse energy, (left) and trigger efficiency for electrons passing medium identification criteria (right) [66].

requirements also increase the probability of selecting muons for which the momentum measurement is reliable. The variables that are used for checking the quality of combined tracks are: the normalised χ^2 of the global fit, the significance of the charge and momentum measurements in the ID and MS and the difference between the p_T measurements in the two subdetectors divided by the momentum of the combined track.

Four muon identification operating points are defined. These are *Medium, Loose, Tight* and *High-p_T*. In this analysis, if muon isolation is applied, the *Medium* working point is implied. Objects considered for this working point rely on combined tracks or tracks reconstructed in the MS that are compatible to originating from the interaction point. Muons passing the *Medium* isolation criteria have smaller uncertainties related to reconstruction and calibration.

Muon isolation

The procedure used to evaluate the muon isolation if very similar to the one described for electrons. This relies on input from both the tracking detector and the calorimeter. Relative isolation criteria are considered and include the ratio of E_T^{cone20} and $p_T^{varcone30}$ [5] and the muon momentum.

Several isolation working points are defined. The *Gradient* operating point, that was applied for selecting muons used in this analysis, uses both relative isolation variables in order to keep the isolation efficiency of 90(99) % for $p_T = 25(60)$ GeV.

Muon trigger

In order to identify muons for triggering, coincident hits in the RPC and TGC chambers (for L1 trigger) and additional precision hits in the MDT and CSC chambers are required. A two stage procedure is in place, resulting in muons that are reconstructed using algorithms that are very close to the offline

---

[5] $p_T^{varcone30}$ is defined as the scalar p_T sum of all tracks in a cone of size $\Delta R = \min(0.3, 10\,\text{GeV}/p_T^\mu)$ around the muon.

reconstruction procedure [68]. More details on the specific trigger requirement used for selecting muons for this analysis are given in section 5.3.

Muon efficiency

Similar to the procedure described for calculating the overall efficiency for electrons, the muon efficiency ϵ_{muon}, is the product of the individual reconstruction, identification, isolation and trigger efficiencies. The correction factors for MC events to match the muon efficiency in data are calculated in samples of $Z \rightarrow \mu\mu$ and $J/\psi \rightarrow \mu\mu$ events. The reconstruction efficiency for muons is shown as a function of p_{T} in figure 3.7. This is valid for all muons within the $|\eta| > 0.1$ range.
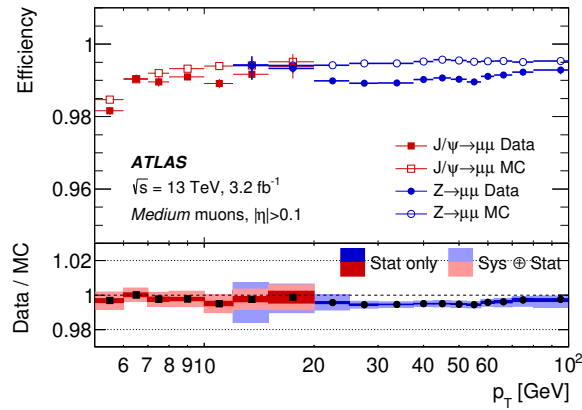
Figure 3.7: Reconstruction efficiency for *Medium* muons as a function of the muon p_{T} [67].

3.3.3 Jets

Jets are collimated sprays of particles that originate from quark and gluon production via fragmentation and hadronisation. In order to define a jet, the algorithm used for the reconstruction of the jet must be specified. Correct identification and measurement of jets is crucial since it translates the information recorded from the interaction of stable particles with the detector to the physics at parton level. All jet reconstruction algorithms must be infrared and collinear safe. This means that the number of reconstructed jets in an event should not depend on the appearance of additional collinear splittings or soft emissions [69].

In ATLAS the anti-k_t algorithm [70, 71] is used. The anti-k_t is a sequential recombination algorithm. The starting point of the reconstruction is calculating distances between particles (or pseudojets) and also the distance of each entity with respect to the beam (d_{iB}). These can be written as:

$$d_{ij} = \min(k_{ti}^{-2}, k_{tj}^{-2}) \frac{\Delta_{ij}^2}{R^2},$$

$$d_{iB} = k_{ti}^{-2},$$

where Δ_{ij} is the distance between particles i and j in the $y - \phi$ plane and k_{ti}, k_{tj} are the transverse momenta of particle i and j respectively. R is the radius parameter; it gives a good indication of the

geometrical scale of the reconstructed jet. In ATLAS, jets with $R = 0.4$ are typically used.[6] If $d_{ij} < d_{iB}$, particles i and j are merged and the created pseudojet is added back to the list of input objects. The previous steps are repeated until $d_{ij} > d_{iB}$, in which case object i is identified as a final state jet.

The anti-k_t algorithm is infrared and collinear safe and results in approximately circular jets. Because of the definition of the distance measure d_{ij}, the anti-k_t algorithm starts by clustering hard particles, meaning that the jet will be seeded by the hardest particles and soft particles will be added to the jet subsequently. Other jet reconstruction algorithms, such as Cambridge-Aachen or k_t show different behaviour (the clustering is done independent of the energy of the particle or the clustering of the soft particles is done first). More details on these and also cone algorithms cam be found in [69].

ATLAS reconstructs jets with $p_T > 30$ GeV in the $|\eta| < 4.5$ region. The default procedure for jet reconstruction uses topo-clusters as input objects but combining calorimeter information with information from the tracking detectors is also being investigated [72]. The energy of the topo-clusters is calibrated at the EM scale.

In order to match the energy scale of reconstructed jets to that of simulated stable particles within a jet (also called truth level jet), a jet energy scale (JES) calibration is performed. The role of this procedure is to account for differences in jet measurements due to different structure of the detector in different regions, non-compensating calorimeters, dead material in the detector, jet reconstruction algorithm and pile-up events. The JES consists of several steps that are applied in sequence and that are presented in detail below. These combine MC based methods and data-driven techniques.

The **origin correction** shifts the four-momentum of the jet such that the jets originates from the hard-scattering primary vertex. The energy of the jet remains unchanged after this correction.

Pile-up corrections are applied in order to make the momentum measurement of the jet independent of pile-up conditions due to multiple pp interactions. This includes two steps: first the p_T of each jet is adjusted by subtracting the expected pileup contribution according to the area of the jet; after that any residual dependence on N_{PV} and $\langle \mu \rangle$ is corrected for. The area-based correction is applied to the jet four-momentum, without changing its η and ϕ coordinates.

In order to have uniform position and energy measurements for jets, independent of the jet direction and momentum, **jet energy scale and η calibrations** are performed. Biases can occur when a jet crosses transition regions between calorimeters or layers with different granularities. The calibration is done by correcting the jet response[7] with respect to the jet p_T and η.

The last correction that is derived using MC samples is the **global sequential correction**, GSC. This tries to reduce the dependency of the jet response on the flavour of the parton that initiated the jet. This is done by correcting the jet response dependence on quantities such as the number of tracks associated to a jet, fraction of jet energy measured in the first layer of the hadronic calorimeter and others.

In situ **techniques** are used to account for remaining differences in the jet energy scale, as well as discrepancies between data and MC. These are performed by requiring well-defined reference objects that are momentum-balanced with a jet [73]. The correction factor is calculated as the difference in jet response between data and simulation and is only applied on data. In this case, the response of a jet is derived relative to the reference object.

Different sources of uncertainties are considered for all steps in the JES determination. These can be seen in figure 3.8, along with the different components. The overall uncertainty is below 5% for very central jets across the whole p_T range. In the region of interest for this analysis, with jets that have p_T between 30 GeV to 150 GeV, the uncertainty is below 3%. More details on the impact of jet

---

[6] Jets with $\Delta R = 1$ (large-R jets) are also used in analyses with boosted topologies.

[7] The jet response is defined as the ratio between the transverse momentum of the reconstructed jet and the transverse momentum of the jet at truth level.

uncertainties on the result of this analysis are given in section 6.3.
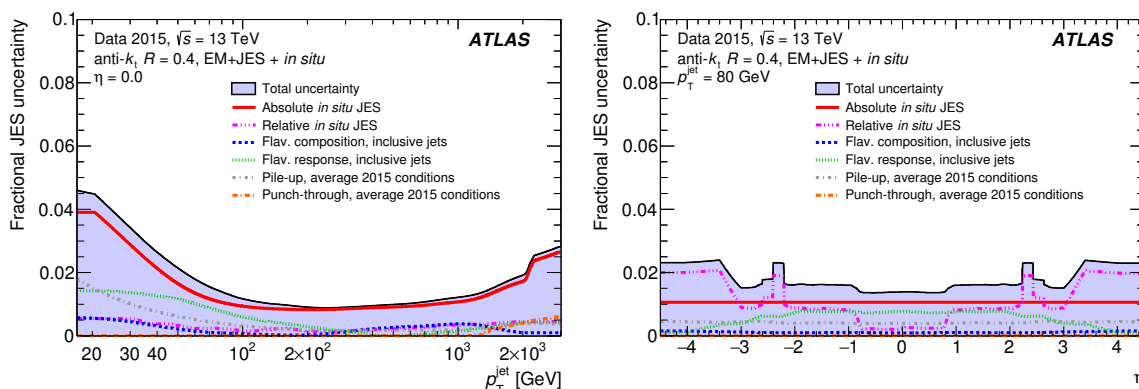
Figure 3.8: Combined JES uncertainty for anti-k_t calibrated jets as a function of jet p_T at $\eta = 0$ (left) and as a function of η for $p_T = 80$ GeV. The systematic uncertainty sources included are related to pile-up, punch-through corrections, flavour composition and response and uncertainties propagated from the in situ calibration [74].

In order to reduce pile-up effects, a discriminant called the jet-vertex-tagger (JVT) is implemented for identifying the jets that originate from the hard scattering interaction. This is constructed using a two-dimensional likelihood method. The input variables for the tagger are related to the ratio between the transverse momentum carried by tracks associated to a jet that are matched to the hard scattering vertex and the total transverse momentum of all matched tracks [75].

A cut on the JVT discriminant is applied for jets with $p_T < 60$ GeV and $|\eta| < 2.4$. This has a pile-up jet rejection of 98 %, while still being 92 % efficient.

Overlap removal

The overlap removal procedure is applied in order to avoid double counting when detector signals are used in the reconstruction of more than one physics object. In the first step, if a jet is found within $\Delta R = 0.2$[8] of an electron, it is removed from the event. After this, if an electron-jet pair with $\Delta R < 0.4$ is identified, the electron will be discarded from the event record. A similar procedure is used for muons, with additionally requiring the jets in the first step to have maximum 3 associated tracks.

Jet flavour tagging

b-tagging of jets is defined as the process of identifying if a jet contains a b hadron. Separating b-jets from jets that are produced by light-flavour partons is very important for data analysis because it offers a good handle for suppressing backgrounds containing only light-flavour jets. In order to correctly identify such jets, one can make use of the distinct features of b hadrons, such as the long lifetime, high mass and decay multiplicity, as well as the harder b-quark fragmentation function.

Several algorithms have been developed in ATLAS in order to improve b-tagging. All of them use as input reconstructed tracks left by the charged particles in the detector. The recommended b-tagging algorithm used in Run 2 is called MV2 and combines information from several others algorithms. All of them will be briefly discussed below; more details can be found in [76].

---

[8] For the overlap removal procedure the ΔR distance is calculated using rapidity and not pseudorapidity.

Impact parameter based algorithms, such as IP2D or IP3D, rely on the fact that the lifetime of weakly decaying b hadrons is approximately 1.5 ps. Because of that, the tracks produced in b-hadron decays will not point towards the hard-scattering interaction point, but will be displaced. For each of the input tracks, two important quantities can be calculated. These are the $r - \phi$ distance of closest approach between the track and the primary vertex, d_0, called the transverse impact parameter and the longitudinal impact parameter, $z_0 \sin \theta$, that is defined as the longitudinal distance between the primary vertex and the track at the point of closest approach in the $r - \phi$ space. Both quantities are expected to be larger for tracks that originate from b hadrons. The significances of these variables, d_0/σ_{d_0} and $z_0 \sin \theta/\sigma_{z_0 \sin \theta}$, are used for constructing probability density functions from Monte Carlo simulations. The last step is computing a log-likelihood discriminant to separate between different jet flavours. This is defined as $\sum_{i=1}^{N} \log \frac{p_i}{p_j}$, where the sum runs over all N tracks in the jet and p_i, p_j are the probability density functions for the different jet flavour hypotheses. For example, when separating b jets from light-flavour jets, p_b and p_u are used. One can perform a similar procedure for separating b- from c-jets or c- from light-flavour jets.

Secondary vertex finding algorithms, denoted SV, rely on the fact that at least one additional displaced vertex with respect to the hard-scattering interaction point should be present in a b-hadron decay. The algorithm checks all track pairs inside a jet in order to find possible secondary vertices. A veto is used for discarding track pairs that pass this criteria but also are consistent with the hypothesis of a secondary vertex due to long-lived particle decays, photon conversion or hadronic interactions with the detector material.

JetFitter is a decay chain multi-vertex reconstruction algorithm that reconstructs the b hadron decay chain inside a jet. It finds a common line for the primary vertex and the secondary vertices that are potentially created by b- and c-hadron decays. This gives information about the flight path of b hadron.

Information from the previously described taggers is combined in MV2 algorithms using multivariate analysis techniques. A boosted decision tree (BDT) is used for separating the "signal" (b jets) from "background" (c- and light-flavour jets). The analysis presented in this thesis uses the MV2c10 version of this MVA based tagger. This is optimised in order to increase c-jets rejection, while still having a high light-flavour jet rejection, by using a 7% fraction of c-jets in the background training sample. The previously recommended version of the tagger used a 20% c-jets fraction (referred to as MV2c20).

Several quantities are defined in order to quantify the performance of a tagging algorithm. The b-tagging efficiency, ϵ_b, is defined as the efficiency for a jet containing a b hadron to be correctly identified by the tagging algorithm. The rejection is defined as the inverse of the efficiency, indicating the number of light-flavour jets in which one will be wrongly identified as a b jet.

BDT cut value	b-jet efficiency [%]	c-jet rejection	light-flavour jet rejection	τ rejection
0.6459	77	6	134	22

Table 3.2: Properties of the MV2c10 b-tagging algorithm at the 77% operating working point [76].

In order to select b-tagged jets, different cuts on the BDT discriminant are investigated for defining working points for which the efficiency has a specific value (when measured in a $t\bar{t}$ sample). For example, the 77% working point that was used for selecting the b-tagged jets used in this analysis, is defined such that the b tagging efficiency is kept constant at $\epsilon_b = 77\%$. The corresponding values for the c- and light-flavour jet rejection are listed in table 3.2. The numbers are evaluated using a $t\bar{t}$ MC simulated sample in which both top quarks decay semi-leptonically. Figure 3.9 shows the b-tagging efficiency (left) and c-tagging rejection (right), as a function of jet p_T, comparing the MV2c10 configur-

ation (labeled as "2016 config") and the MV2c20 tagger ("2015 config"). While the *b*-tagging efficiency is similar between the two configurations, the *c*-tagging rejection is significantly improved across the whole p_{T} spectrum.
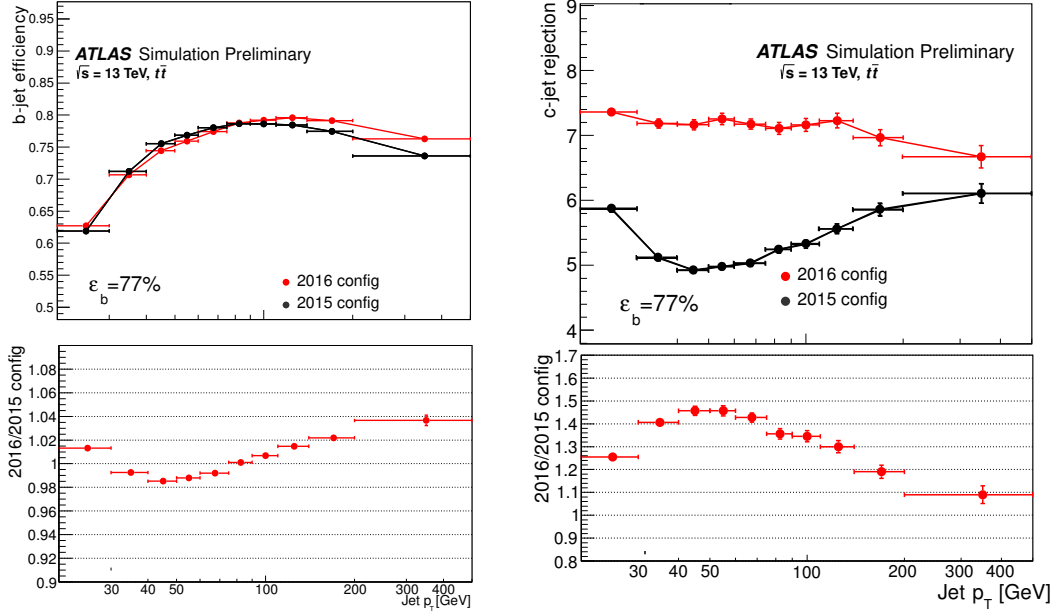
Figure 3.9: *b*-tagging efficiency (left) and *c*-jet rejection (right) evaluated in $t\bar{t}$ simulated events. The MV2c10 and MV2c20 vaersions of the tagger are compared. [76].

3.3.4 $E_{\mathrm{T}}^{\mathrm{miss}}$ reconstruction

For the reconstruction of missing transverse momentum, fully calibrated electrons, muons, photons, hadronically decaying tau leptons and jets are used. In addition to these hard objects, the soft hadronic activity must be taken into account. This is done by considering all the tracks reconstructed in the inner detector that are associated to the primary vertex but are not included in the hard object reconstruction [77].

The components of the $E_{\mathrm{T}}^{\mathrm{miss}}$ term are calculated as:

$$E_{x(y)}^{\mathrm{miss}} = E_{x(y)}^{\mathrm{miss},e} + E_{x(y)}^{\mathrm{miss},\gamma} + E_{x(y)}^{\mathrm{miss},\tau} + E_{x(y)}^{\mathrm{miss},\mu} + E_{x(y)}^{\mathrm{miss, jets}} + E_{x(y)}^{\mathrm{miss, soft}},$$

where the $E_{x(y)}^{\mathrm{miss, i}}$ terms represent the inverse $x(y)$ momentum components of object i. The order in which the objects are considered is the same as the terms in the formula. For examples, the photons passing specific quality and kinematic criteria will be added to the $E_{\mathrm{T}}^{\mathrm{miss}}$ calculation if the signal does not overlap with any of the previously added electrons.

Using the two components, two observables are constructed. The $E_{\mathrm{T}}^{\mathrm{miss}}$ magnitude is calculated as:

$$E_{\mathrm{T}}^{\mathrm{miss}} = \sqrt{(E_x^{\mathrm{miss}})^2 + (E_y^{\mathrm{miss}})^2}.$$

The direction is specified by the corresponding azimuthal angle, ϕ^{miss}, defined as:

$$\phi^{\text{miss}} = \tan^{-1}(E_y^{\text{miss}}/E_x^{\text{miss}}).$$

The performance of reconstructing E_T^{miss} is evaluated both in data and MC simulation. This consists of evaluating the resolution and response for the reconstructed E_T^{miss}. Samples with and without real missing energy are used. This include $W \to e\nu$ and $Z \to \mu\mu$ events respectively.

The response gives an impression about how much the reconstructed E_T^{miss} differs from the expectation value. For events with low activity, the response is non-linear[9] due to observation biases. These occur because the experimental conditions do not always allow for the p_T reconstruction of all objects coming from the hard scatter and, additionally, all reconstructed p_T contributions suffer from limited resolution. This effectively leads to a non-vanishing E_T^{miss} calculation even for events in which no undetected particles were present.

The E_T^{miss} resolution is defined as the width of the distribution of $E_{x(y)}^{\text{miss}}$ and the difference with respect to the true missing transverse momentum components. It was observed that the resolution worsens with increasing pile-up and also increases for events with high $\sum E_T$ [78].

---

[9] A non-linear response depends on the truth E_T^{miss} or other quantities related to the hard scatter activity.

Data and Monte Carlo Simulated Samples

In order to extract information from *pp* collision data and test SM predictions, reliable MC simulated samples that reflect our knowledge of particle interaction and production must be used. By comparing the recorded data with these simulations, one can test the SM hypothesis, as well as search for new physics. This chapter starts with details about the dataset that was used for this analysis. The second half of the chapter is dedicated to MC simulations. Firstly, a brief overview of how MC simulation works is included. Details about the samples used in this analysis for modelling the signal and background processes are given in the last section.

4.1 Data sample

This analysis was performed on *pp* data collected by the ATLAS detector during its 2015 and 2016 operations. In this time, a dataset larger than the full Run 1 dataset was collected. Figure 4.1 shows the total LHC delivered luminosity as well as the amount recorded by the ATLAS experiment. An efficiency of 93 % and 92 % was achieved for 2015 and 2016, respectively.

Each ATLAS dataset consists of several *runs*. These are uninterrupted periods of time in which the detector is recording data. A unique run number is assigned at the start of the respective run. Typically an ATLAS run corresponds to one LHC cycle. After the beams that are circulating through the accelerator are dumped (safely terminated) and the energy is ramped down, a setup period follows in order to prepare for the next beam injection. A probe beam is circulated before the beams that will be used for physics. Once the physics beams are injected, their intensities are gradually increased until they reach the nominal operation point. Afterwards, the energy is ramped up until it reaches 6.5 TeV per beam. In preparation for the collisions, the beams are squeezed and adjusted. At this point, the LHC declares the physics beams as stable and proton–proton collision data can be recorded by the detector. In figure 4.1, the LHC delivered luminosity is measured from the moment when stable beams are declared until a request is made to the experiments to switch to safe mode and prepare for beam dump.

An ATLAS run is usually started when the physics beam are injected and ends when the physics beams are dumped. However, the inner detectors undergo a warm-start procedure after stable beams are declared. This is needed for ramping up the high-voltage on the tracking detectors and turning on the pre-amplifiers of the pixel detectors. This procedure is one of the reasons why ATLAS records less luminosity than the amount delivered by the LHC. Another reason is the inefficiency of the data acquisition system.
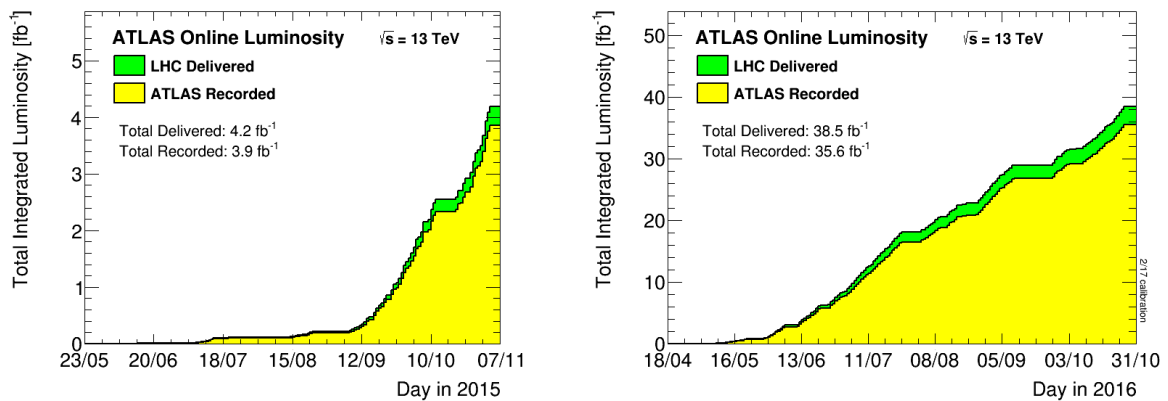
Figure 4.1: Total integrated luminosity for the 2015 (left) and 2016 (right) operations [79].

The luminosity measurement in ATLAS is done by several dedicated detectors, such as the LUminosity measurement using a Cherenkov Integrating Detector (LUCID) or the Beam Control Monitor (BCM). These measure the luminosity bunch-by-bunch. This can be done by event counting or hit counting. In event counting, every bunch crossing is scanned through a set of criteria in order to check if it is consistent with the occurrence of at least one inelastic collision and is categorised accordingly. Hit counting algorithms identify the number of detector signals that pass a preset threshold. An alternative method of determining the luminosity is the counting of well reconstructed events coming from processes that have a very precisely known cross-section, such as $Z \rightarrow \mu\mu$. Details about these procedures, along with descriptions of the ATLAS luminosity detectors can be found in [80] and [81].

However, the amount of data recorded by ATLAS is not the total luminosity used for physics analyses. A *good run list* (GRL) is compiled by data quality experts in order to identify the runs (and luminosity blocks[1] inside a run) for which the detector was fully operational. This analysis was performed on data passing all recommended quality criteria and selected based on the GRL for physics analysis. This corresponds to a total integrated luminosity of $36.1\,\mathrm{fb}^{-1}$, out of which $3.3\,\mathrm{fb}^{-1}$ have been recorded in 2015 and $32.8\,\mathrm{fb}^{-1}$ in 2016.

4.2 Monte Carlo simulation

Monte Carlo simulation is a key tool in high energy physics, for both theorists and experimentalists. Simulated samples are used for estimating the feasibility of certain measurements by predicting event numbers, topologies and background contributions as well as for studying detector features, requirements or response.

The structure of a *pp* collision event in MC generation can be divided in five main parts that will be described below. These are related to the different stages that occur from the parton collision to the detected final state particles.

Hard interaction In order to simulate the hard scattering process the matrix element of this interaction has to be calculated and the phase space integration must be performed including selection requirements. The PDFs of incoming partons are taken into account and perturbation theory is used for the amplitude calculation. Several collaborations are working on the determination of parton distribu-

---

[1] ATLAS data is recorded in luminosity blocks. This is a time unit for data-taking and its duration is typically around one minute.

tion functions using experimental data, including all available electron–proton and proton–(anti)proton collision data. The PDFs are derived by performing global fits up to NNLO in QCD.

Parton showering The partons carry colour charge and hence can radiate additional gluons. These in turn can also emit radiation, giving rise to a shower predominantly consisting of soft gluons. In order to reproduce the formation of such parton showers, MC generators use sequential algorithms that evolve the shower in terms of a certain variable (relative transverse momentum, virtuality, etc.), from the hard-scattering until a cutoff scale (related to the hadronisation scale).

Hadronisation The hadronisation process refers to the property of partons to form bound states (hadrons). These new particles can be seen in the detector. There are several models that try to explain how this process occurs and are implemented in different MC generators. The most extensively used hadronisation models are the Lund string model [82] and the cluster model [83].

Underlying event All hadronic activity that is not involved in the hard scattering process represents the underlying event. Events in which no hard scattering process occurs are called minimum bias events. However, the underlying event does not only consist of these type of events. Additionally, multiple parton interactions can occur. These happen if secondary interactions between the beam remnants take place.

Unstable particle decays After hadronisation, along with stable hadrons[2], unstable resonances can be created. These decays are modelled according to the corresponding known decay information and branching ratios.

The MC generation results in a set of events with well defined, stable, final state particles for which all the kinematic information is known. At this point, all relations between particles are also known (decay product/ mother particle). This is referred to as *truth level*. Before being used for analysis however, the generated events must go through the detector simulation.

Several multipurpose generators are available and differ by key parameters, such as choice of hadronisation model or evolution and splitting variable for the parton showering. A comparison between the most popular generators can be found in [85]. Each of these models introduces free parameters. The optimisation of these parameters in order to reproduce measured observables is called tuning. A set of such optimised parameters is often referred to as a "MC tune".

In ATLAS, the programs used more often for the generation of the matrix element are Powheg [86–88], MadGraph5_aMC@NLO [89], Herwig 7 and Sherpa. For parton showering (including hadronisation, fragmentation and underlying event), Pythia (versions 6 [90] and 8 [91]), Herwig 7 and Sherpa are available.

4.2.1 MC samples for processes of interest

In order to estimate the *tZq* signal and background contributions and their uncertainties, several MC generated samples are used. More information of why these particular background processes were selected, is given in section 5.1.

Details on each generated sample (including the PDF sets that were used) are given below. For processes including top quarks, the top-quark mass was set to 172.5 GeV in the generation process.

Simulation of the signal sample

The generation of the signal events was done using MadGraph5_aMC@NLO, while for the parton shower and hadronisation simulation Pythia 6 was used (with the Perugia2012 set of tuned paramet-

---

[2] Typically, in this context, a particle is "stable" if it has $c\tau \geq 10$ mm. This is also valid for strange hadrons such as $K, \Lambda, \Sigma^{\pm}, \Omega, \bar{\Sigma}^{\pm}$ and Ξ [84].

ers [92]). The *tZq* process is simulated in the four-flavour scheme at LO precision in QCD. The PDFs used are CTEQ6L1 [93] and are as well LO.

Interference between the *tZq* process and *WZ* production can occur. This was not taken into account when generating the *tZq* sample and is not considered in this analysis. The choice of renormalisation and factorisation scale is driven by the fact that the scale dependence is dominated by the external *b*-quark coming from gluon splitting. Because of that, a dynamic scale is used, with $\mu_{\mathrm{r}} = \mu_{\mathrm{f}} = 4\sqrt{m_b^2 + p_{\mathrm{T},b}^2}$ [94].

Some MC generators output events with an associated weight that has to be applied in order to correctly normalise the sample. It was observed that when generating a NLO *tZq* sample, over 40 % of events have a negative weight, thus causing a significant loss in statistics. Because of that, a LO sample was preferred.

Differences between the LO and a NLO *tZq* MC sample were investigated and the shapes between the kinematic distributions agree within 10 %. Since the difference between the LO and NLO cross-section is significant (approximately 30 % of the LO cross-section), the *tZq* sample is normalised to the NLO cross-section. This is calculated using MADGRAPH5_aMC@NLO, with the NNPDF3.0_NLO_AS_0118 NLO PDF [42] and it is found to be 800 fb, with an uncertainty of $^{+6.1}_{-7.4}$%. The calculated uncertainty includes the renormalisation and factorisation scale choice effects. The NLO cross-section calculation is also done in the four-flavour scheme.

Simulation of the background samples

Details of all simulated samples are given in table 4.1. This includes the name of the generator, parton shower, PDF set and MC tune for each process.

In order to account for detector effects and evaluate the acceptance on the signal and background, the full detector response is simulated using GEANT4 [95, 96]. Pile-up conditions are taken into account by simulating multiple inelastic collisions and overlaying them over each of the MC events. The pile-up simulation is done using PYTHIA 8.

Process	MC generator	Parton shower	PDF set	Tune	Order
WZ	SHERPA 2.1.1	SHERPA	CT10	-	LO
ZZ	SHERPA 2.1.1	SHERPA	CT10	-	LO
$t\bar{t}$	POWHEG	PYTHIA 6	CT10	Perugia2012	NLO
tW	POWHEG	PYTHIA 6	CT10	Perugia2012	NLO
$t\bar{t}Z$	MADGRAPH5_aMC@NLO	PYTHIA 8	NNPDF2.3LO	A14	NLO
$t\bar{t}H$	MADGRAPH5_aMC@NLO	PYTHIA 8	NNPDF2.3LO	A14	NLO
tWZ	MADGRAPH5_aMC@NLO	PYTHIA 8	NNPDF3.0_NLO	A14	NLO
Z + jets	SHERPA 2.2.1	SHERPA	CT10	-	NLO

Table 4.1: Summary of background MC generated samples.

4.2.2 Reweighting of Monte Carlo simulated events

Event-by-event reweighting

In order to correctly reproduce the data-taking conditions, as well as replicate the efficiency of selecting different physics objects, in the simulated samples, event-by-event correction factors are applied to the

MC generated events. The total event weight can be written as:

$$w_{\text{event}} = w_{\text{MC}} \times w_{\text{pile-up}} \times w_{\text{lepton}} \times w_{\text{JVT}} \times w_{\text{trigger}} \times w_{b\text{-tagging}}.$$

w_{MC} is the MC event weight. This needs to be applied because it is the sum of these weights that will give the correctly estimated number of events for that sample.

When the MC sample is generated, a certain pile-up profile is assumed. If this does not match the one observed in data, a $w_{\text{pile-up}}$ term is introduced in order to reweight the sample accordingly. Since the LHC operations at the start of Run 2 exceeded expectations and reached record intensity, $\langle\mu\rangle$ was also larger than the one used for MC simulation. The pile-up profile for the 2015 and 2016 datasets is shown in figure 4.2. The average number of interactions per crossing was 13.7 and 24.2 for 2015 and 2016, respectively.
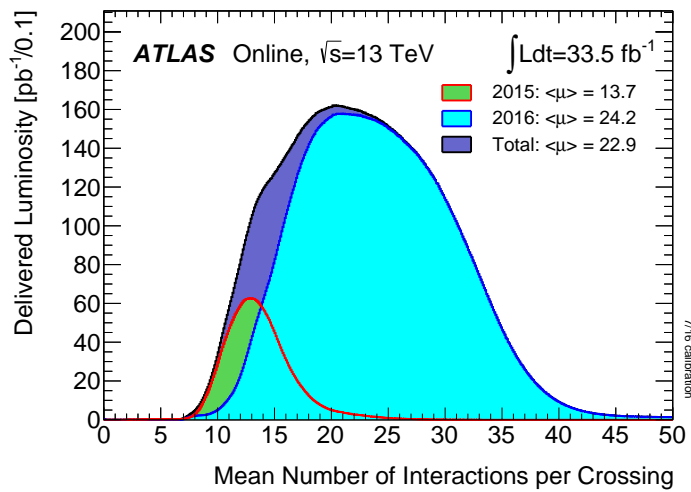
Figure 4.2: Luminosity weighted plot of the mean number of interactions per crossing for the 2015 and 2016 datasets [97].

The following weights are related to certain reconstruction or selection steps of the events or the physics objects that could lead to different efficiencies in MC and in data. These need to be accounted for by dedicated SFs. The w_{lepton} term is related to the efficiency of reconstructing, identifying and requiring a certain lepton isolation. This has been already discussed in detail in section 3.3.1. This term is applied by multiplying the individual weights corresponding to each of the leptons selected in the event.

Differences in data and MC efficiencies when applying a cut on the JVT discriminant (described in the previous chapter) are taken into account by applying the w_{JVT} weight. Selected events are required to pass certain trigger criteria. Any mismatch related to the trigger selection efficiencies in data and MC are corrected for by applying the w_{trigger}. Because the events passing the analysis selection criteria are required to have a b-tagged jet, the $w_{b\text{-tagging}}$ weight also needs to be applied.

Luminosity weighting

One of the advantages of using MC generated events for simulating physics processes is that one can produce samples with very high statistics. The number of simulated events is only limited by the available computing time and resources. However, in order to correctly estimate the contribution of a certain

process to a dataset, the luminosity of the MC sample must match the luminosity of the collected data. Because of that, MC events in a sample must be corrected using a factor defined as:

$$w_{\text{lumi}} = \sigma_{\text{process}} \mathcal{L}/N_0,$$

where σ_{process} is the cross-section of the specific physics process, $\mathcal{L}$ is the integrated luminosity of the data sample and N_0 is the number of events in the original MC sample.

Event selection and background estimation

This chapter presents the *tZq* final state for which the analysis is performed as well as the strategy for selecting events that match the signal signature in order to maximise the potential for discovery.

The first section summarises the possible decay topologies in *tZq* events. In section 5.2, the processes that can yield a similar final state (background processes) as the signal are discussed. Based on that, a phase space region that is enriched in signal events is defined (this is referred to as the Signal Region – SR). The preselection applied to the physics objects is discussed in section 5.3 and the criteria applied in order to select events in the SR are presented in section 5.4. The final part of the chapter presents the methods used to estimate the background contributions, with emphasis on the estimation of background processes that involve a fake or non-prompt lepton in the final state. The last section shows how these estimations are checked in dedicated validation regions (VRs).

5.1 *tZq* trilepton final state

This analysis searches for events in which a single top-quark is produced in association with a Z boson. However, both of these particles are not stable and can only be observed via their decay products. As mentioned in section 2.3.1, the top quark decays almost exclusively into a W boson and a b quark. In turn, the W boson decays either leptonically, into a charged lepton and the corresponding neutrino, e.g. $W^- \to e^- \nu_e$, or hadronically, $W^- \to q\bar{q}$. The Z boson can decay into a pair of opposite sign, same flavour leptons, hadonically or into neutrinos (sometimes called invisible decay). The corresponding branching ratios for the above mentioned final states, as well as the probability of the combined states are summarised in figure 5.1. Due to lepton universality, the probability for a particle decaying to a final state involving leptons is equal for the three lepton families (electron, muons and taus). However, the tau lepton is observed in the detector only through its decay products. The mass of the τ is large enough to allow decays with final states that include hadrons. This happens in roughly 65% of the cases. The rest of events are evenly split between two possible leptonic decays: $\tau^- \to e^- \bar{\nu}_e \nu_\tau$ and $\tau^- \to \mu^- \bar{\nu}_\mu \nu_\tau$. In this analysis only events including leptonic τ decays are considered. In accordance with that, the branching ratio numbers shown in figure 5.1 for all decays involving leptons do not include the τ hadronic decays.

The efficiency of correctly reconstructing and measuring charged leptons is much higher than that of hadronic objects. Additionally, a *tZq* final state involving leptonic decays is more difficult to be reproduced by background processes with higher cross-sections. Because of these reasons, the analysis was performed after selecting candidate events in which both the top quark and the Z boson decay

Z boson decay modes

	$Z \to \ell^+\ell^-$ 7.8%	$Z \to \text{invisible}$ 20%	$Z \to qq$ 69.9%
$t \to bW \to b\ell\nu$ 25.3%	**2%**	5.1%	17.7%
$t \to bW \to bqq$ 67.4%	5.3%	13.5%	47.1%

$\ell = e, \mu, \tau \to e/\mu \; \nu_{e/\mu} \nu_\tau$

Figure 5.1: Branching ratios for the top quark and Z boson decays. The probability for each combination of particles in the *tZq* final state is also given. Only final states including leptonic decays of the τ lepton are included. The channel in which this analysis is performed is underlined in blue.

leptonically. Although this combination only happens in 2% of *tZq* produced events, it is this channel that has yielded the best signal to background ratio and thus, the best potential for discovery. An example Feynman diagram for this decay chain is shown in figure 5.2. The *tZq* final state consists of three charged leptons[1], two jets (one of which is originating from a *b* quark) and missing transverse momentum.
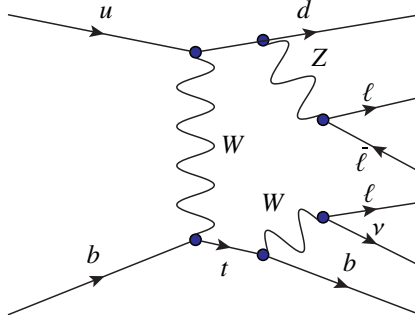
Figure 5.2: Feynman diagram for LO *tZq* production, with the top quark and Z boson decaying to final states involving charged leptons.

5.2 Sources of background

The background processes that can lead to a final state similar to the one previously described can be classified according to the number of prompt (or real) leptons in the final state. A prompt lepton is defined as originating from a decay of a τ lepton or a massive boson. Similar to *tZq*, some background processes will include three prompt leptons in the final state. Other background events are due to processes with a dileptonic final state, that pass the trilepton requirement because they have an additional non-prompt (or fake) lepton. These leptons come from decays of bottom or charm hadrons, leptons from kaon or pion decays or even electrons coming from photon conversions. Additionally, jets can be misidentified as electrons. The procedure to estimate backgrounds that include a non-prompt lepton is

---

[1] From here on, unless stated otherwise, "leptons" will be used to refer to electrons and muons only.

described in detail in the second half of this chapter.

The backgrounds involving only real leptons are diboson (*WW*,*WZ* or *ZZ*), $t\bar{t}V$ (*V* = *Z*, *W*), $t\bar{t}H$ and *tWZ* production. The contribution for each of these backgrounds is estimated from Monte Carlo simulated samples that are normalised to their SM cross-sections.

Diboson production

Events in which two bosons (*W* and/or *Z*) are produced represent one of the main backgrounds for the *tZq* selection. In particular, *WZ* events with leptonically decaying bosons and additional jets will yield an identical final state to the *tZq* trilepton signature described above. Events coming from *ZZ* production contribute much less. A similar final state as *tZq* only occurs if both *Z* bosons decay leptonically and one of the leptons is either not reconstructed or fails the object selection criteria. Figure 5.3 shows example Feynman diagrams of the two processes.

Due to the use of a LO Monte Carlo generated sample for this background (as described in chapter 4), an additional normalisation factor is applied in order to improve data and MC agreement. The procedure for determining this factor is discussed in detail in the following section.

(a) WZ　　　　　　　　　　(b) ZZ
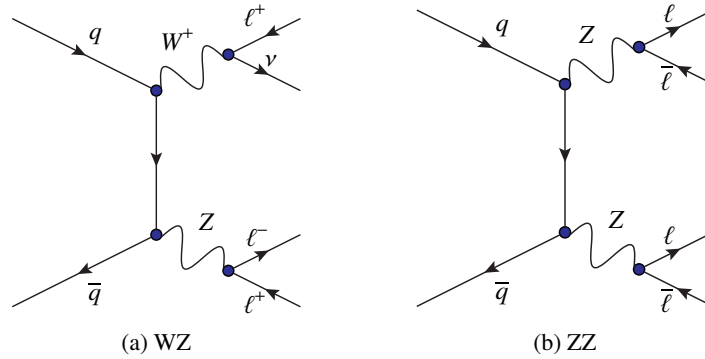
Figure 5.3: Example Feynman diagrams for diboson processes with final states involving charged leptons.

$t\bar{t}V$ and $t\bar{t}H$ production

Events in which a top-quark pair is produced in association with a heavy boson can also pass a *tZq* targeted selection. In particular, $t\bar{t}Z$ events can have a very similar signature, since the final state already includes a top quark and a *Z* boson. The cross-section for such processes is also higher than that of the signal. A Feynman diagram for the $t\bar{t}Z$ process can be seen in figure 5.4. The associated production of a pair of top quarks and a Higgs boson will have a very small contribution due to its low cross-section and small branching ratio for Higgs boson decays involving leptons.

tWZ production

The production of a top quark along with a *W* and *Z* boson is a process that has not been experimentally measured so far and is predicted to have a very small cross-section, around 12.2 fb [98]. However, its final state can be very similar to the trilepton *tZq* signature for a leptonically decaying *Z* and *W* boson (either the one produced in the hard scattering or the one coming from top-quark decay). Nevertheless, this process will yield a higher jet multiplicity.

Figure 5.5 shows the latest ATLAS measurements for SM production cross-sections and compares them to the available theoretical predictions. The signal, *tZq*, is labeled on the plot as *tZj* and has one
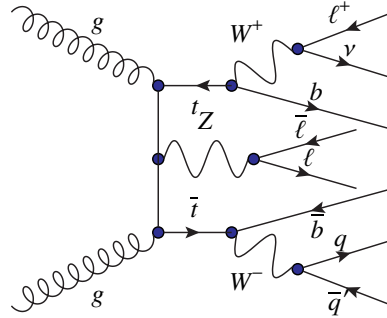
Figure 5.4: Example Feynman diagram for $t\bar{t}Z$ production with a final state involving charged leptons.
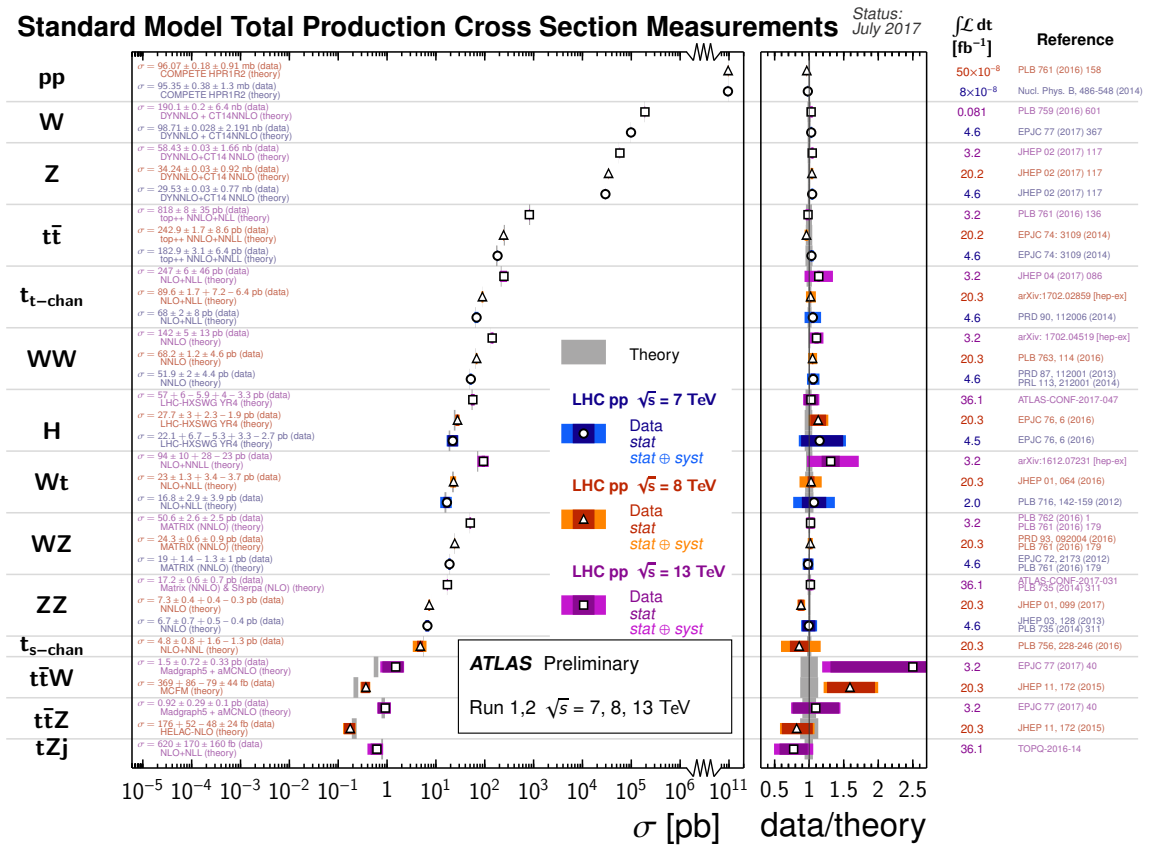
Figure 5.5: Summary of several SM total production cross-section measurements, corrected for leptonic branching fractions, compared to the corresponding theoretical expectations [99].

of the lowest cross-sections compared to all other processes. All the backgrounds described before that have experimentally been measured are included in the plot. For the *WZ* process, which is the dominant source of background, a cross-section of 50.6 ± 2.6(stat.) ± 2.0(syst.) ± 0.9(th.) ± 1.0(lumi. fb) was measured at 13 TeV, in agreement with the NNLO theoretical prediction [100]. The $t\bar{t}Z$ cross-section measurement yields 0.92 ± 0.29(stat.) ± 0.1(syst.) fb [40]. The cross-sections for processes that give rise to non-prompt lepton background, $t\bar{t}$ and Z + jets, are several orders of magnitude higher compared to the *tZq* cross-section.

5.3 Event preselection

The way physics objects are reconstructed in the ATLAS detector was already described in section 3.3. Once these are reconstructed for all events, a preselection is made by applying certain requirements in order to keep only events in which hard scattering collisions occurred, with well reconstructed physics objects, as well as discard events with very different final states compared to the *tZq* final state. This is applied on all MC and data samples and the selection is done in the order described below.

In order to minimise biases in data caused by detector operation, the first requirement that is applied is for the events to be collected during a lumi block marked as good for physics in the GRL. Additionally, only events for which no noise bursts in the LAr and Tile calorimeters occurred during the data taking are kept.

All selection criteria are applied on events at reconstructed level. At least one primary vertex needs to be identified for the event to be considered.

Only jets reconstructed using the anti-k_t algorithm with $R = 0.4$ and that have passed the JVT selection and overlap removal procedure (described in section 3.3.3) are considered. Additional quality criteria specifically designed for anti-k_t jets are available in order to distinguish jets with high p_T that originate from pp collisions and jets from non-collision interactions such as beam induced background, cosmic ray showers or calorimeter noise. These are documented in [101]. If, for an event, any of the jets that pass the previous requirements does not pass the additional jet cleaning quality criteria, the whole event is discarded. This ensures an efficiency of selecting jets from proton-proton collisions above 99.5 % (99.9 %) for $p_T > 20\,\text{GeV}(100\,\text{GeV})$.

Because the *tZq* final state involves leptons, a trigger requirement is applied that includes a logical OR combination of single electron and muon triggers. Details on the Run 2 ATLAS available triggers can be found in [102]. Only events in which at least one of the leptons is matched to one of the triggers in table 5.1 are kept. The trigger names specify the p_T requirement (in GeV) at the HLT level (and L1 level if the trigger requires both HLT and L1 information), as well as the isolation criteria for the considered lepton.

	2015 Triggers	2016 Triggers
Electrons	HLT_e24_lhmedium_L1EM20VH HLT_e60_lhmedium HLT_e120_lhloose	HLT_e26_lhtight_nod0_ivarloose HLT_e60_lhmedium_nod0 HLT_e140_lhloose_nod0
Muons	HLT_mu20_iloose_L1MU15 HLT_mu50	HLT_mu26_ivarmedium HLT_mu50

Table 5.1: Single electron and muon triggers for 2015 and 2016 data.

Events in which at least one muon is flagged as having p_T reconstruction that is not consistent between

the ID and the MS are discarded. The efficiency of this veto is higher than 99 % up to the TeV range in muon p_T.

In the final step of the preselection, events are required to have at least two leptons with p_T above 15 GeV and at least one jet with p_T above 25 GeV. All the selected lepton objects must pass identification and isolation criteria corresponding to the *Tight* operating points described in section 3.3.1 (for electrons) and section 3.3.2 (for muons).

5.4 Signal region definition

The SR definition is designed to select *tZq* candidate events with a trileptonic final state and, at the same time, minimise as much as possible the number of events coming from background processes. This is done by applying certain selection criteria (cuts) on the kinematic variables of the physics objects corresponding to the final state particles, as well as requirements on the reconstructed intermediate particles (the Z and the top quark). Complementary to the SR, by applying specific sets of cuts, validation and control regions (CRs) are defined. CRs are used either for deriving normalisation factors or for estimating the non-prompt lepton background. VRs are defined such that they have a small signal contamination and that they are enriched in events coming from the process that is being validated.

For the SR, the selected physics objects are three leptons, one *b*-tagged jet, one untagged jet and missing transverse momentum. The Z boson is reconstructed by selecting two opposite sign, same flavour (OSSF) leptons. For events in which two such pairs can be identified, the two leptons with the invariant mass closest to the Z boson mass are used for reconstructing the Z boson. The remaining lepton, missing transverse momentum and *b*-tagged jet are combined for reconstructing the top quark. The untagged jet is then assumed to be the jet coming from the spectator quark in the hard scattering process. Since it is expected to be emitted at high η, it is referred to as the *forward jet*.

A summary of the SR definition is given in table 5.2. The first step in the selection is requiring exactly three leptons passing different p_T thresholds. Studies have shown that a higher p_T threshold for the softest lepton would further increase the signal to background ratio by reducing the contribution from Z + jets events, but overall this would not bring an improvement in the final result. Out of the three selected leptons, at least one opposite sign, same flavour pair is required.

Table 5.2: Summary of the requirements applied for selecting events in the signal region.

3 leptons with $|\eta| < 2.5$ and $p_T > 15$ GeV
$p_T(\ell_1) > 28$ GeV, $p_T(\ell_2) > 25$ GeV, $p_T(\ell_3) > 15$ GeV
≥ 1 OSSF pair
2 jets, $|\eta| < 4.5$
1 *b*-jet, $|\eta| < 2.5$
$p_T(\text{jet}) > 30$ GeV
$|m_{\ell\ell} - m_Z| < 10$ GeV
$m_T(\ell_W, \nu) > 20$ GeV

Exactly two high-p_T jets are selected. These are allowed to be anywhere within the $|\eta| < 4.5$ range in order to also select jets going in the forward direction. One of the two jets must be *b*-tagged by passing the 77 % tagging working point and should be in the central region of the detector ($|\eta| < 2.5$).

Requiring the invariant mass of the two leptons associated to the Z boson (OSSF pair) to be within a 20 GeV window around $M_Z = 91.2$ GeV reduces all background processes that do not have a Z boson,

such as $t\bar{t}$ and tW.

In order to separate events in which no leptonically decaying W boson is produced, and because neutrino related information is only available in the transverse plane, one can use the reconstructed transverse mass of the W boson, $m_\mathrm{T}(\ell_W, \nu)$. This is defined as:

$$m_\mathrm{T}(\ell_W, \nu) = \sqrt{2p_\mathrm{T}(\ell)p_\mathrm{T}(\nu)\left[1 - \cos\Delta\phi\,(\ell, \nu)\right]}.$$

For processes that include a $W \rightarrow \ell\nu$ decay, this distribution is expected to peak at values close to the mass of the W boson. This will, however, not be exactly at 80 GeV due to detector effects and the fact that only the transverse information is used.

Selecting events with $m_\mathrm{T}(\ell_W, \nu) > 20$ GeV, improves the signal to background ratio by rejecting events in which no W boson is produced, especially the Z + jets non-prompt lepton background.

Figure 5.6 shows how the SR composition changes after applying each of these cuts. Each pie-chart is constructed using the number of SR events after applying the cut listed above the diagram. The Z + jets contribution is not included because it is estimated using a fully data-driven procedure and hence it is only defined in the region of phase space in which it was derived. This gives a representation of how the signal over background ratio evolves and improves after each cut is applied.

After preselection, the number of $t\bar{t}$ and diboson selected events is significantly larger compared to the signal. Requiring exactly two jets, one of which has to be b-tagged, helps with reducing the diboson background. The $t\bar{t}$ contribution is considerably reduced when selecting events with exactly three leptons. The signal contribution becomes visible after that, constituting a significant fraction of the selected events. The requirement for having an OSSF lepton pair with invariant mass close to the Z boson mass visibly enhances the fraction of events coming from processes that include a Z boson (such as tZq and WZ) by minimising the $t\bar{t}$ contamination.

Complementary to figure 5.6, the efficiency of each cut on the signal and background processes is shown in figure 5.7. This is calculated as the number of events passing the respective cut divided by the number of events before applying the cut. Again, the cuts are applied sequentially, e.g. the efficiency of requiring exactly three leptons is calculated relative to the number of events that have already passed the jet related selection criteria. As a rule of thumb, for every selection criteria the efficiency on the signal should be higher than the efficiency of the backgrounds. This would indicate that by applying the cut, a larger fraction of the background is discarded than signal, thus improving the overall S/B. The efficiency in data is shown in black. There are several cuts that have very low efficiency in data, meaning that a lot of the previously selected events will be discarded, however, as long that the signal fraction is improved, this is not a problem. The signal efficiency of the last four cuts is very hight, above 90 %. In the bins in which the signal line is not visible, it is because it overlaps with the highest entry in that bin (e.g. for the "OSOF pair" cut, the signal and diboson efficiencies are equal and very close to 1).

By applying a similar selection as for the SR, CRs are defined for deriving a normalisation factor for the diboson contribution and performing the $t\bar{t}$ and Z + jets non-prompt lepton background estimation. In addition to that, two dedicated VRs are defined in order to check signal and background modelling. One of them is enriched in $t\bar{t}$ events and the second one validates the modelling of the diboson background, as well as the Z + jets estimation. The definitions for all VRs and CRs are described relative to the SR definition, in the following subsections.
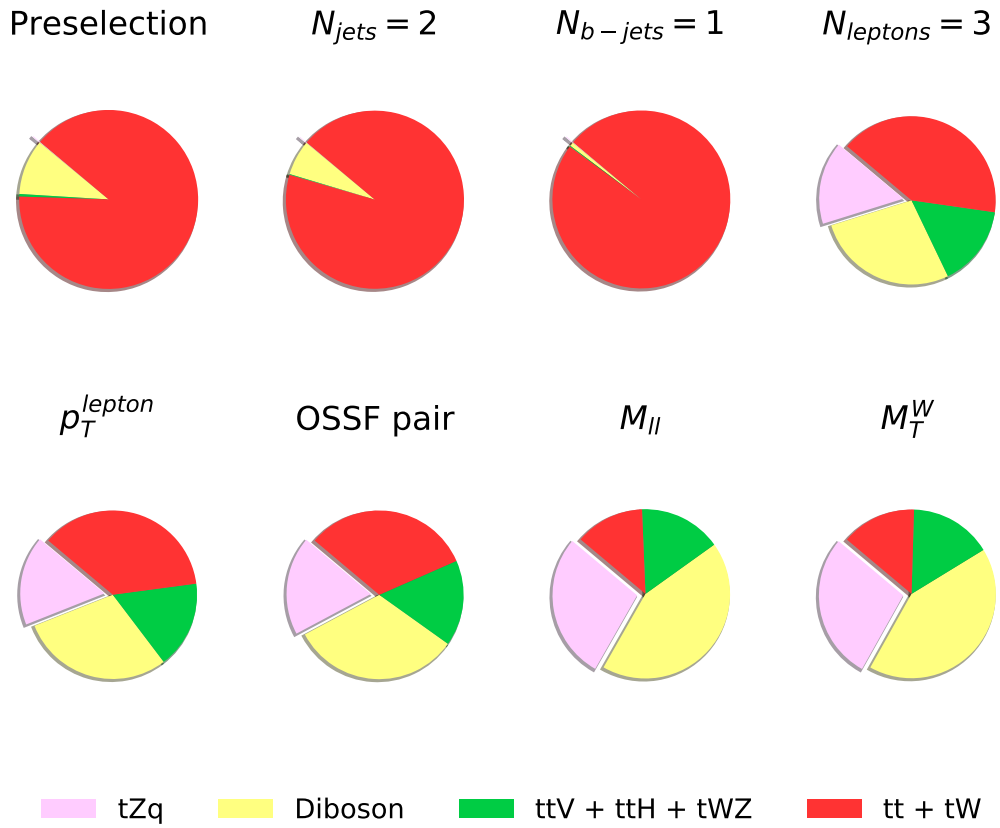
Figure 5.6: SR composition evolution after applying selection criteria.
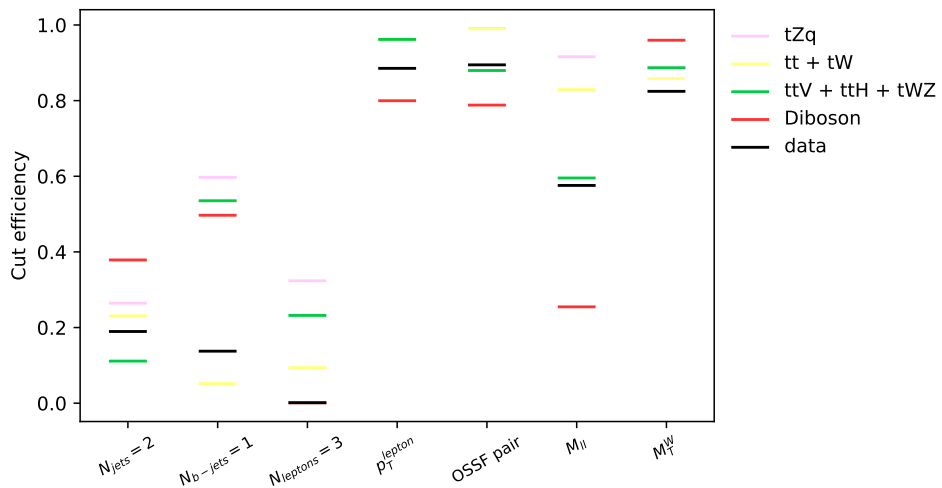
Figure 5.7: Efficiency of each SR selection requirement on the signal and background processes.

5.5 Background Estimation

5.5.1 Diboson normalisation correction

Diboson events form the largest background for the *tZq* trilepton final state. When selecting regions of phase space dominated by diboson events, it was observed that the number of diboson MC events obtained using the SHERPA generator consistently underestimates the number of observed events. Therefore, in order to correctly evaluate the diboson contribution in the SR, a dedicated CR is used to derive a normalisation scale factor. This region must have minimal signal contamination and be dominated by diboson events. Additionally, it is important to reduce the number of Z + jets events in order to separate the diboson normalisation effects and not be biased by the Z + jets data-driven estimation uncertainty.

The diboson CR region has very similar selection cuts to the ones of the signal region described in table 5.2. In order to increase the number of *WZ* events, only one jet is required (and no requirement on the jet flavour is applied). Additionally, in order to reduce Z + jets contamination, a cut is applied on $m_\mathrm{T}(\ell_W, \nu)$[2]. This is required to be above 60 GeV. The $m_\mathrm{T}(\ell_W, \nu)$ distribution in the diboson CR is shown in figure 5.8. The normalisation SF is calculated as the ratio between the data and MC prediction in this region and is found to be 1.47.
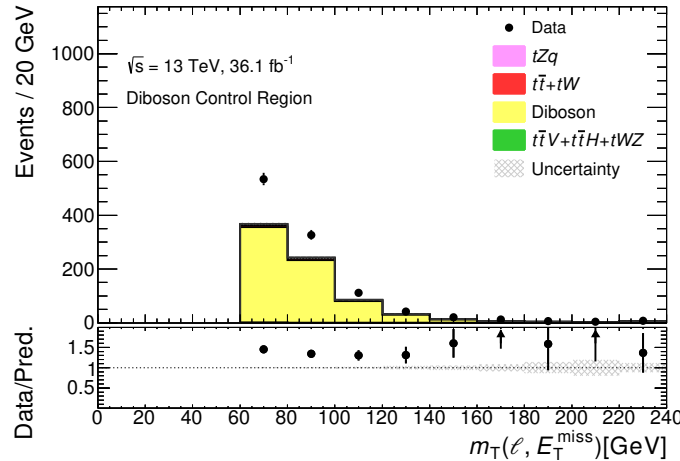
Figure 5.8: Distribution of the $m_\mathrm{T}(\ell_W, \nu)$ variable in the diboson CR.

In order to check how the chosen $m_\mathrm{T}(\ell_W, \nu)$ cut changes the normalisation, the scale factor was recalculated for events passing different $m_\mathrm{T}(\ell_W, \nu)$ thresholds. Increasing the cut value up to 80 and 100 GeV gives SF values consistent with the nominal one within ±0.08. This is included as a systematic uncertainty on the diboson contribution. An additional uncertainty derived from comparing this estimation with one obtained using a NLO generated sample is also added. This is discussed in more detail in section 6.3.

---

[2] This variable is chosen because it offers very good separation between diboson and the Z + jets background, with the non-prompt background mostly populating the low $m_\mathrm{T}(\ell_W, \nu)$ region.

5.5.2 Non-prompt lepton background estimation

The *tZq* final state includes three real leptons (electrons or muons), coming from a *W* or *Z* boson or a τ lepton. However, dilepton events with an additional non-prompt or fake lepton[3] can also pass the selection. In the case of electrons, these can be from decays of bottom or charm hadrons, photon conversions (non-prompt) or jets with large energy depositions in the ECAL that are misidentified as electrons (fake leptons). Non-prompt muons can originate from semileptonic decays of heavy flavour objects, decays of charged hadrons in the tracking volume or in hadronic showers, or from particles that are produced in high-energetic hadronic showers that are not stopped in the HCAL [103].

The two sources of non-prompt lepton background for this analysis are $t\bar{t}$ and Z + jets events. Example Feynman diagrams for both processes can be seen in figure 5.9.

(a) $t\bar{t}$
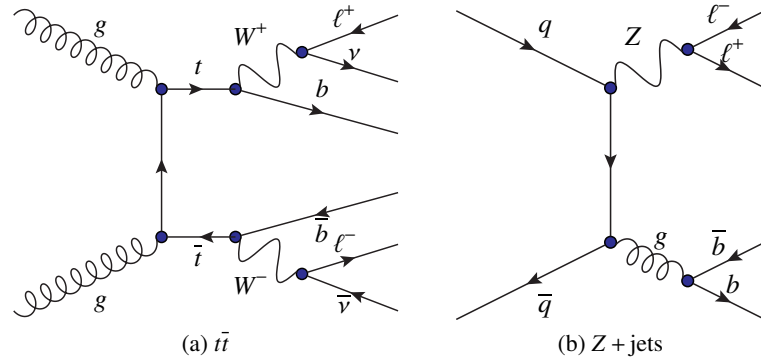
(b) Z + jets

Figure 5.9: Example Feynman diagram for LO $t\bar{t}$ and Z + jets production, including subsequent decays to final states involving charged leptons.

The cuts applied for the signal region selection are designed to reduce non-prompt lepton background contributions as much as possible but since this is still non-negligible, the correct number of events must be estimated. Because this background category includes different sources for the production of non-prompt leptons, it is difficult to reliably model the shape and normalisation just based on MC simulation. Because of that, data-driven techniques are typically employed.

The two contributions are evaluated separately according to the process of origin. For Z + jets, a purely data-driven technique is used (namely the fake-factor method), while for the $t\bar{t}$ events estimate, a data/ MC SF is derived in a dedicated CR and subsequently applied to the $t\bar{t}$ MC predicted events in the SR. Both methods and their results are described in the following sections.

Non-prompt lepton origin in trilepton final states

In order to better understand the non-prompt lepton background, the origin of these leptons in the trilepton final state is investigated. This is done by accessing truth level information using the
`MCTruthClassifier` tool [104]. The study is performed for leptons passing the signal region selection.

For $t\bar{t}$ events, the plots showing the origin of the three selected leptons can be seen in figure 5.10, separated for events in which the non-prompt lepton is an electron and a muon. The leptons are labelled according to how they are sorted in the event reconstruction procedure, by indicating their associated final-state particle when assuming a *tZq* final state. Although this association is not particularly meaningful in a $t\bar{t}$ sample (because a Z boson does not exist), the same notation is used in order to be

---

[3] This background contribution will be simply referred to as the non-prompt lepton background, since this is the dominant component. Fake leptons from misidentified jets are also included.

consistent with similar studies performed for the $Z + \text{jets}$ background and the rest of the analysis. The highest transverse momentum lepton candidate from the OSSF pair is labelled as "Z lepton 1" and is shown in blue and the second highest p_T lepton is shown in green ("Z lepton 2"). The lepton associated to the W boson is depicted in yellow ("W lepton").

In a $t\bar{t}$ sample, if the lepton is prompt, its origin should be a W boson. Figure 5.10 shows that for all events, this is the case for "Z lepton 1". Non-prompt leptons are identified as the softest Z lepton candidate in over 65 % of the cases or as the "W lepton" in the remaining 35 %.

Additionally, the plots indicate that the dominant source of non-prompt leptons are heavy-hadron decays. An example Feynman diagram of a semileptonic b decay can be seen in figure 5.11.
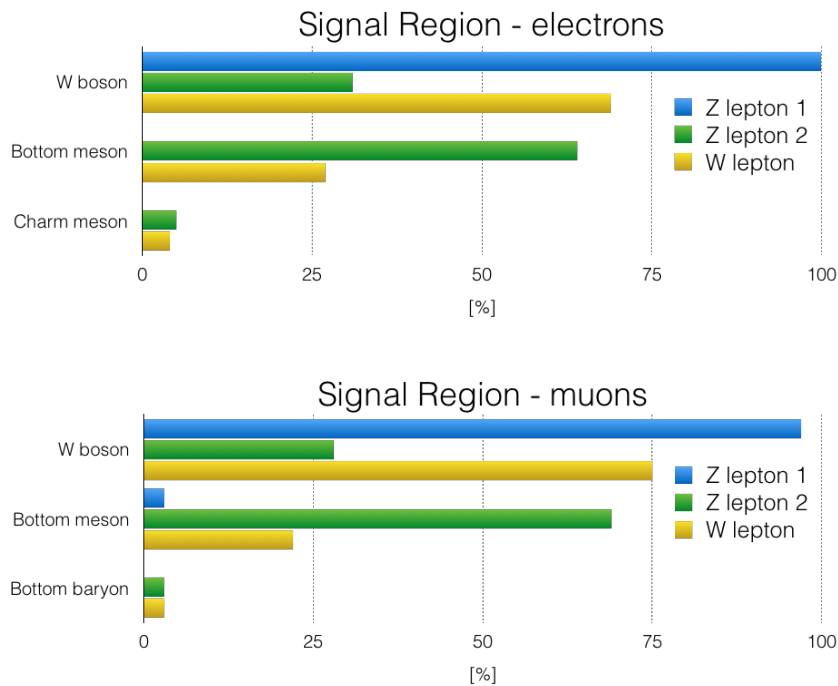
Figure 5.10: Origin of the SR leptons in the $t\bar{t}$ sample. The top plot includes events that have a non-prompt electron and the bottom plot non-prompt muon events. The particle of origin is shown on the y axis.
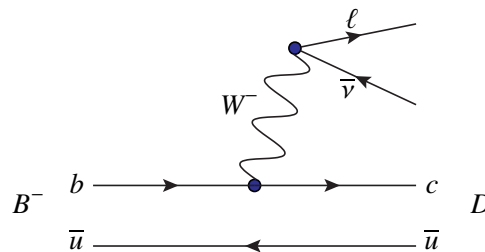
Figure 5.11: Example Feynman diagram of a semileptonic decay of a B meson.

$t\bar{t}$ background estimation

In order to estimate the number of $t\bar{t}$[4] events passing the SR selection due to having an additional non-prompt lepton, a data/MC SF is derived for correcting the number of events estimated from the MC generated sample.

A dedicated control region ($t\bar{t}$ CR) is defined that is enriched in such events. This is used for the derivation of a global SF that can be applied to correct the $t\bar{t}$ MC estimation in the signal region. Two cross-checks consisting of deriving flavour dependent scale factors, as well as p_T dependent factors are presented in appendix C.1. In order to ensure that the origin of the non-prompt leptons is similar in the SR, CR and the region that will be used to validate the SF, truth-level studies were performed for the $t\bar{t}$ VR and CR, showing very similar results as the ones in figure 5.10. These are included in appendix C.1.

The $t\bar{t}$ CR keeps the same selection as the signal region, but instead of requiring one OSSF lepton pair, it selects events that have a pair of leptons with opposite sign and different flavour (OSOF) and discards any events in which an OSSF lepton pair can be found. This requirement completely eliminates the contribution of Z + jets events from this control region, making sure that the estimation is reliable for $t\bar{t}$ events. The $t\bar{t}$ purity in this CR is very high (over 80 %) and the signal contamination is minimal.

In this dedicated control region, a data/MC scale factor is derived using

$$\text{SF}_\text{data/MC} = \frac{N_\text{data} - N_\text{MC}^{\text{all-}t\bar{t}}}{N_\text{MC}^{t\bar{t}}} \,, \tag{5.1}$$

where N_data is the number of events observed in data, $N_\text{MC}^{\text{all-}t\bar{t}}$ is the sum of all other MC predictions (diboson, $t\bar{t}V + t\bar{t}H + tWZ$ and tZq) and $N_\text{MC}^{t\bar{t}}$ is the predicted number of $t\bar{t}$ events. This data/MC factor is then used to correct the $t\bar{t}$ MC contribution in the SR.

Control plots showing the observed data and MC predictions in the $t\bar{t}$ CR are shown in figure 5.12.
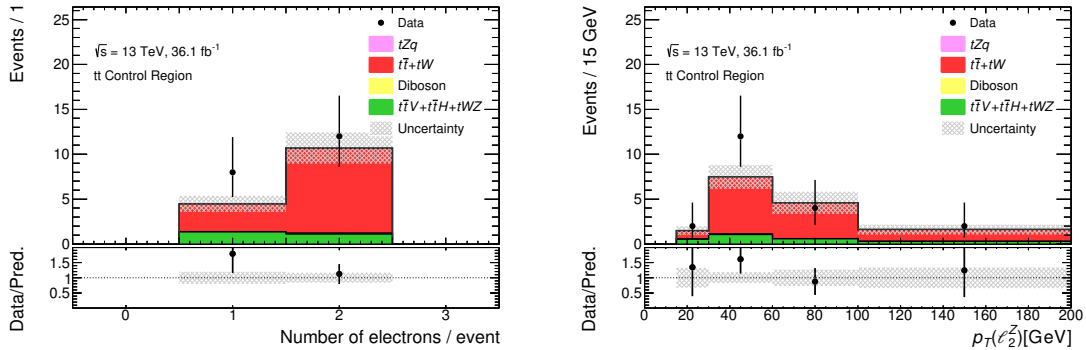
Figure 5.12: Comparison of data and MC predictions for the number of electrons per event (left) and the p_T of the softest lepton associated to the Z boson (right), in the $t\bar{t}$ CR used for extracting the data/MC scale factor. The uncertainty band includes only statistical uncertainties.

Because the selection was kept identical to the SR, a cut is still applied on the invariant mass of the OSOF lepton pair. In order to increase statistics, this cut can be relaxed to higher values than the nominal 20 GeV window around the 91 GeV mass. The $t\bar{t}$ CR suffers from low statistics, so the effect

---

[4] This also includes a very small contribution from tW events (less than 3 %). This is added to the $t\bar{t}$ sample and will not be mentioned explicitly.

of changing the cut value can have a considerable effect on the SF and must be investigated. The mass distribution for this region and the calculated SFs are shown in figure 5.13. The SFs are plotted as a function of the considered mass window cut around $m_Z = 91$ GeV. The final SF is then chosen as the average between factors derived from events with leptons in the Z-mass window of total width between 20 and 60 GeV. The uncertainty on the SF is obtained by propagating the statistical error on the number of observed and predicted events, resulting in a final SF of 1.21 ± 0.51.
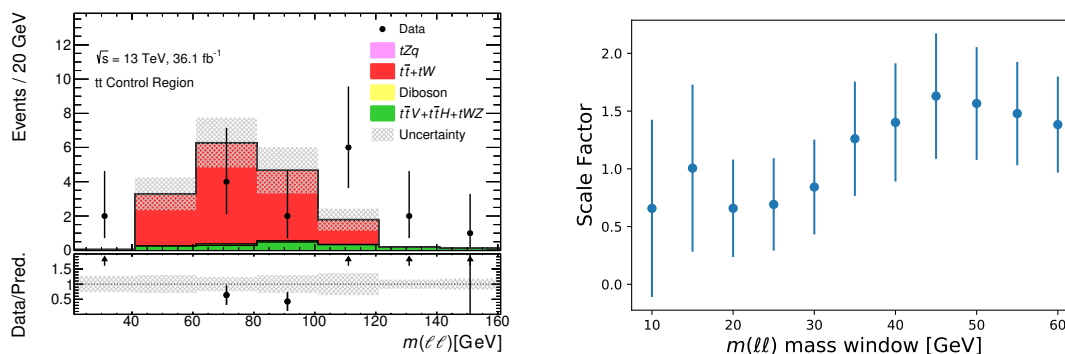
Figure 5.13: Left: comparison of data and MC predictions for the invariant mass of the two leptons associated with the Z boson in the $t\bar{t}$ OSOF CR used for extracting the data/MC scale factor. The uncertainty band includes only statistical uncertainties. Right: dependence of the $t\bar{t}$ scale factor on the mass window cut around the Z-boson mass peak. The value on the x-axis is the total width of the window.

Z + jets background estimation using the fake-factor method

In order to estimate the normalisation and shape of the Z + jets non-prompt lepton background, a data-driven technique is used. The *fake-factor* method relies on the assumption that the probability of a non-prompt lepton to pass isolation criteria is constant in regions of phase space that are close to each other. A fake factor can be derived from data in a region that is enriched in Z + jets events that have at least one non-prompt lepton (FF region). This is applied to a dedicated region that has the same selection as the SR but in which one of the lepton passes looser identification criteria (SR-LTT), resulting in a complete estimation of the non-prompt lepton contribution in the SR.

A schematic representation of how the FF and the SR-LTT regions are defined is shown in figure 5.14. The fake-factor region is obtained by inverting the cut on the reconstructed transverse mass of the lepton and neutrino. This is required to be greater than 20 GeV in the SR and smaller than 20 GeV for the FF selection. The LTT and TTT labels refer to the number of leptons in an event passing tight isolation criteria (3 for TTT regions and 2 for LTT).

Here, "Loose" and "Tight", refer to a combination of identification and isolation criteria based on the already defined working points that were discussed in section 3.3.1 and section 3.3.2. As shown in table 5.3, requirements for defining Tight electrons consist of passing "TightLH" electron identification, while Loose ones require only the "MediumLH" identification. For muon identification, the "Medium" selection operating point is used for both the Tight and Loose selections. In terms of isolation, for both tight electrons and muons, the Gradient working point is used, while for Loose (both $e^{\pm}$ and $\mu^{\pm}$) no isolation criteria are required.

In the FF region, if all three selected lepton objects used in the analysis are Tight, this is labelled as the FF-TTT region. When selecting events passing similar kinematic cuts but one of the leptons is required
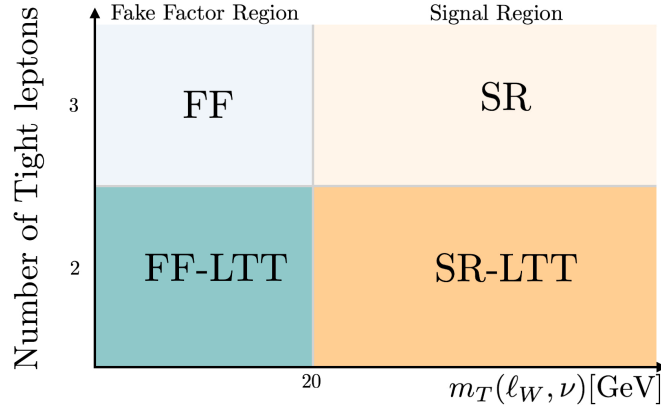
Figure 5.14: Schematic view of the definition of the control and fake-factor regions.

to be Loose-not-Tight[5], the region is called FF-LTT. Similarly, the SR-LTT will be the SR equivalent for which exactly one of the three leptons passes the Loose criteria, but not the Tight ones.

	Loose		Tight	
	Definition	Isolation	Definition	Isolation
Electrons	MediumLH	None	TightLH	Gradient
Muons	Medium	None	Medium	Gradient

Table 5.3: Definition of electron and muon selection criteria for loose and tight leptons.

The fake factor is calculated using

$$FF = \frac{N_{\mathrm{TTT}}^{\mathrm{FF}}}{N_{\mathrm{LTT}}^{\mathrm{FF}}}, \qquad (5.2)$$

where $N_{\mathrm{TTT}}^{\mathrm{FF}}$ gives the number of events in the FF region in which all leptons pass the Tight isolation and identification criteria and $N_{\mathrm{LTT}}^{\mathrm{FF}}$ stands for the events in the FF region in which one of the leptons only fulfils the Loose requirements. In order to obtain the total number of Z + jets events in the signal region, this factor will be applied to events in the SR-LTT region.

Because of the very high efficiency of identifying the two leptons coming from a Z boson, in almost all Z + jets events, the remaining lepton is usually a non-prompt lepton. As a result of trying to fit all events to a *tZq* topology, this lepton is referred to as the lepton associated to the W boson and denoted ℓ_W. The fake factor is derived in p_{T} bins of ℓ_W.

This assumption, as well as the non-prompt lepton origin in all the previously defined regions, was checked at truth level again using the `MCTruthClassifier` tool. For SR-LTT the results are shown in figure 5.15 for events in which the non-prompt lepton is an electron and a muon respectively. Similar plots for the FF regions can be found in appendix C.2, showing very consistent behaviour to the ones presented below. In both the $e^{\pm}$ and $\mu^{\pm}$ channels, the leptons coming from a Z boson are correctly associated after event reconstruction in over 90 % of the cases. This validates the assumption

---

[5] Tight leptons are a subset of the Loose category. In order to have orthogonal samples, the Loose leptons selected are required to not pass the Tight criteria.

that the non-prompt lepton is usually associated to the *W* boson. Furthermore, the origin of the non-prompt leptons can be seen. This is, as expected, in most cases, the semileptonic decay of heavy flavour particles. Leptons for which the origin cannot be identified by the `MCTruthClassifier` are labelled with "Undefined" origin.
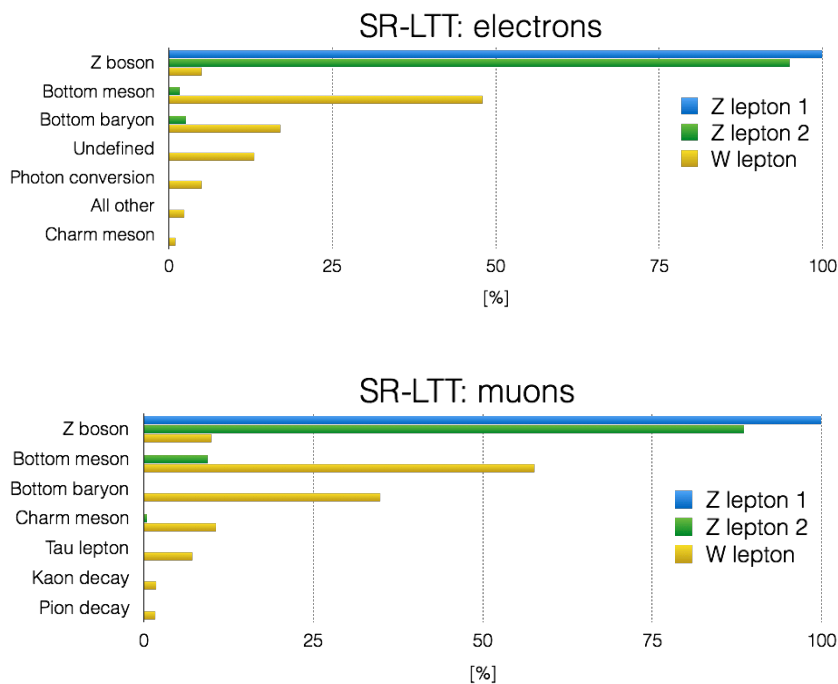
Figure 5.15: Origin of the leptons in the Z + jets sample for events in SR-LTT that have a non-prompt electron (top) or muon (bottom).

The distributions of the numerator and denominator used in the fake-factor definition are shown separately for electrons and muons in figure 5.16. The diboson contribution includes the SF discussed in section 5.5.1. The $t\bar{t}$ background is also corrected with a data/MC SF following the procedure described in the previous section. Because of the very low statistics in the last bins, as well as the very small Z + jets contamination, the last three bins are merged when calculating the fake factors, and only two factors are calculated (for non-prompt leptons with p_T lower than 30 GeV and above 30 GeV). The total number of events for these regions can be found in the first two columns of table 5.4 (for non-prompt electrons) and table 5.5 (for non-prompt muons).

The calculated fake factors are shown in figure 5.17. For a correct estimation of the Z + jets contribution, the events coming from other processes (either involving three prompt leptons or $t\bar{t}$ events) have to be subtracted from the data before extracting the factors. Especially in the LTT control region, the main contribution comes from $t\bar{t}$ events that have one fake lepton. In order to properly subtract this background, the same procedure as presented in section 5.5.2 is applied, namely a data/MC scale factor is calculated from a $t\bar{t}$ fake-enriched region and is then applied to the $t\bar{t}$ events in the SR-LTT region. This scale factor is derived from events that have one OSOF lepton pair and which have exactly one lepton passing the Loose criteria. For better determination of the fake factors, the $t\bar{t}$ scaling is also derived in the same bins of the transverse momentum of the lepton associated to the *W* boson as the fake factors. The corresponding distributions in the $t\bar{t}$ OSOF LTT region, as well as the derived $t\bar{t}$ scale factors can
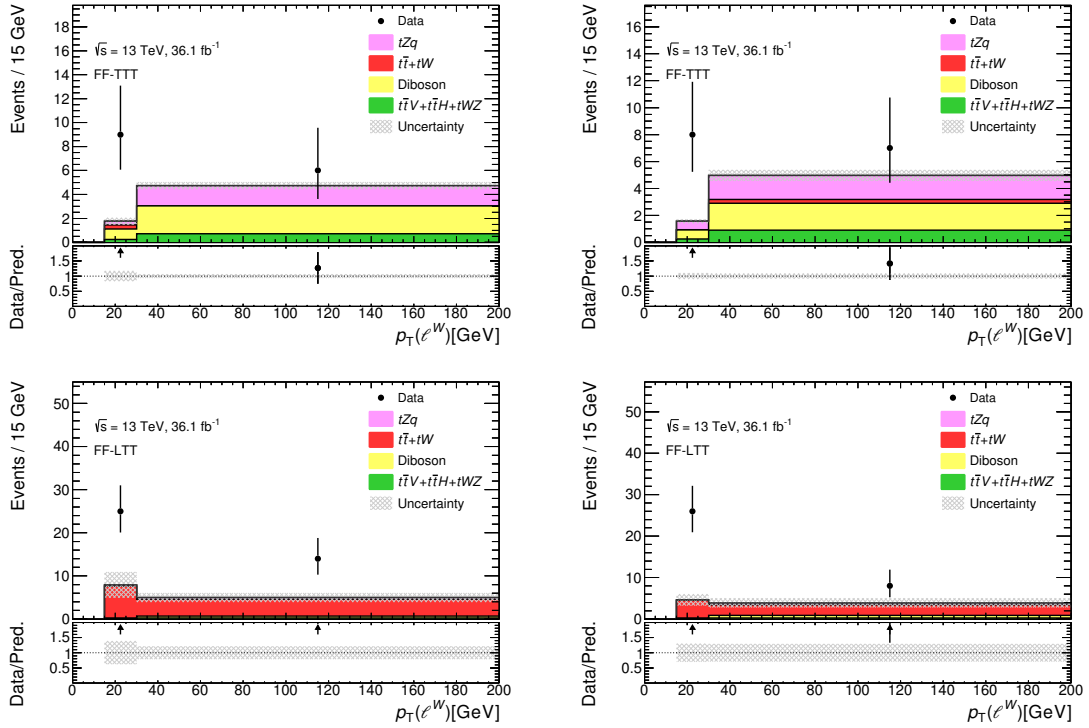
Figure 5.16: Control distributions for the Z + jets FF region, showing the p_T of the lepton associated to the W boson. The top row shows events in FF-TTT region in which the non-prompt lepton is an electron (left) or a muon (right). The bottom row shows the FF-LTT plots. The uncertainty band includes only statistical uncertainties.

Process	FF region (TTT)			FF region (LTT)			CR region (LTT)		
$t\bar{t}V + t\bar{t}H + tWZ$	0.9	±	0.1	0.3	±	0.0	2.8	±	0.1
Diboson	4.7	±	0.5	0.9	±	0.2	8.5	±	0.9
$t\bar{t}$	0.3	±	0.3	11.4	±	3.2	75.9	±	6.2
tZq	1.5	±	0.1	0.5	±	0.1	4.0	±	0.2
Total expected	7.5	±	0.6	13.0	±	3.2	91.1	±	6.3
Data	15			39			163		

Table 5.4: Number of observed and expected events in which the fake lepton is an electron, in the different regions used in the fake-factor method. The numbers of $t\bar{t}V + t\bar{t}H + tWZ$, diboson, $t\bar{t}$ and tW as well the number of tZq events are from the MC simulation.

Process	FF region (TTT)	FF region (LTT)	CR region (LTT)
$t\bar{t}V + t\bar{t}H + tWZ$	1.1 ± 0.1	0.3 ± 0.0	2.4 ± 0.1
Diboson	3.9 ± 0.5	1.2 ± 0.3	6.1 ± 0.7
$t\bar{t}$	0.3 ± 0.3	6.7 ± 1.8	44.5 ± 3.8
tZq	1.8 ± 0.1	0.5 ± 0.1	3.5 ± 0.1
Total expected	7.2 ± 0.6	8.8 ± 1.8	56.4 ± 3.9
Data	15	34	112

Table 5.5: Number of observed and expected events in which the fake lepton is a muon, in the different regions used in the fake-factor method. The numbers of $t\bar{t}V + t\bar{t}H + tWZ$, diboson, $t\bar{t}$ and tW as well the number of tZq events are from the MC simulation.
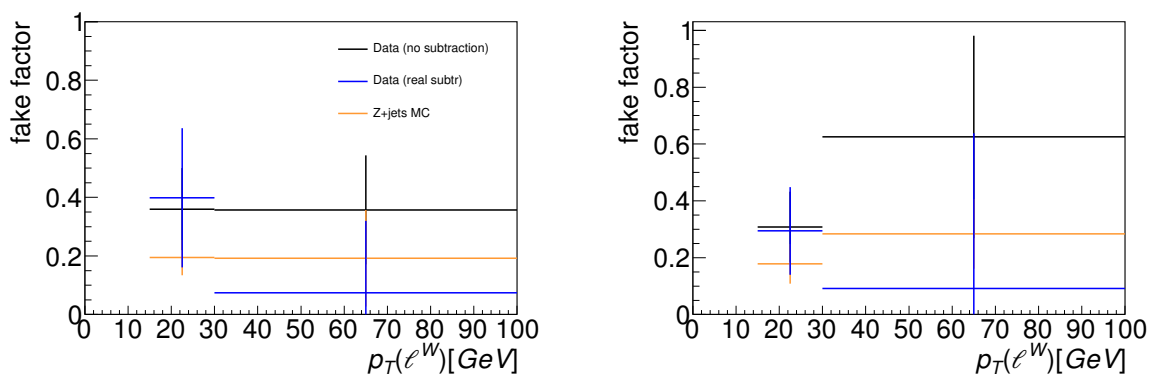
Figure 5.17: Fake factors derived in data, before (black) and after subtracting the contributions coming from backgrounds with three real leptons (blue) and in the Z + jets MC samples. On the left side, the electrons are shown and on the right side, the muon channel.

be found in appendix C.2. The resulting factors are compatible with the $t\bar{t}$ scaling derived for the SR within the calculated uncertainties.

For subtracting the contributions from backgrounds with three real leptons, the MC estimations are used. After the subtraction of all backgrounds from the LTT control region, the derived fake factors are applied to the remaining contribution in order to obtain the signal region Z + jets estimation.

The number of events in the SR-LTT region is given in the third column of table 5.4 and table 5.5 and control plots are shown in figure 5.18. These plots include the data/MC scale factors derived for the $t\bar{t}$ contribution. After taking that into account and applying the fake factors, the total estimated Z + jets contribution in the signal region is 28.1 ± 2.7 events with a non-prompt electron and 8.8 ± 1.3 events in the muon channel. The quoted uncertainty is only statistical and additional sources were studied and are discussed in the following subsection.
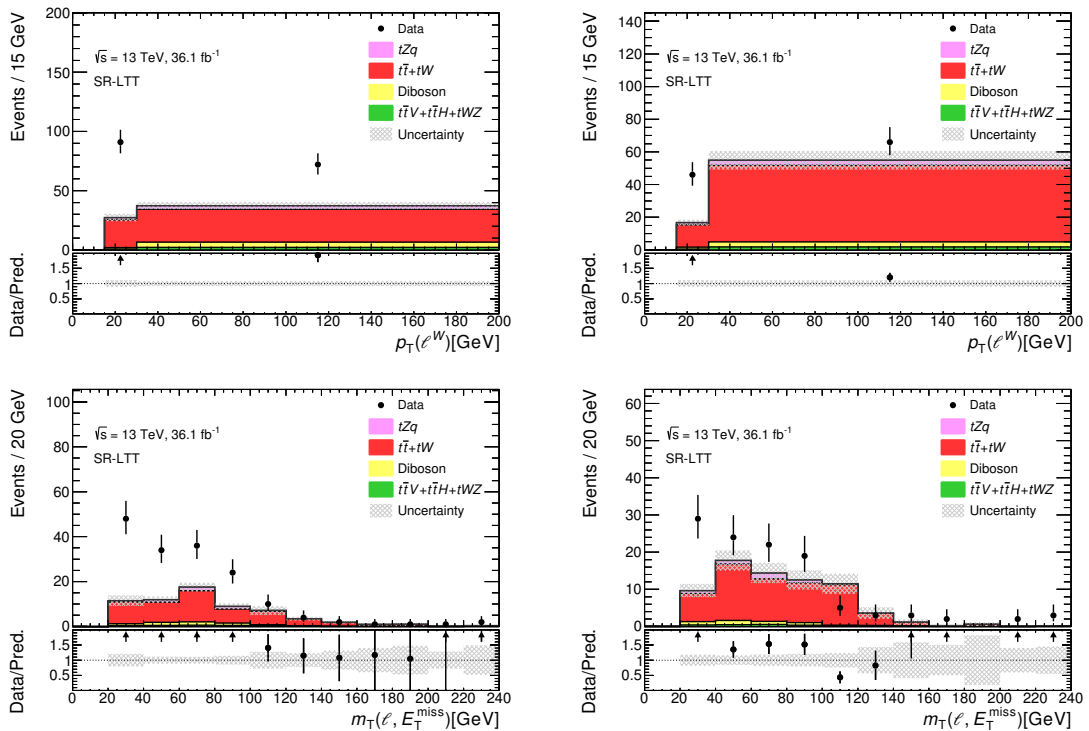
Figure 5.18: Distributions of the p_{T} of the lepton associated to the W boson (top row) and $m_{\mathrm{T}}(\ell_W, \nu)$ (bottom row) for the SR-LTT. The left-hand side plots include events that have a non-prompt electron, while in the right-hand side plots the lepton that we associate to the W boson is a muon. The uncertainty band includes only statistical uncertainties.

As a cross-check, the $t\bar{t}$ background contribution in the SR is estimated using the fake-factor method by applying the Z + jets fake factors to the $t\bar{t}$ contribution in the SR-LTT region. This results in 29.4 ± 11.8 events. Within the uncertainties this result is consistent with our default SR estimation of 18.1 ± 8.6. This comparison assumes similar behaviour for the non-prompt leptons in Z + jets and $t\bar{t}$ events, although the truth studies show that these are quite different in both origin and the final-state particle that they are associated to ($t\bar{t}$ non-prompt leptons are usually associated to the softer lepton coming from the Z boson, while in Z + jets events they are associated to the lepton from the W boson).

Uncertainties on the *Z* + jets background estimation

Three different sources of uncertainties on the Z + jets estimation are investigated and is discussed below. The first one is related to a validation of the method using MC. Additionally, the effect of changing the number of diboson events is also considered, as well as uncertainty due to the low statistics.

MC closure test

In order to validate the fake factor method, a MC closure test is performed. This consists of estimating the MC predicted Z + jets events in the signal region by using the fake factor method with simulated events only. The region for deriving the fake factor, as well as the region where the factor is applied have the same definitions as in the data-driven approach. The MC calculated fake factor was already shown in figure 5.17. This is then applied to the Z + jets MC prediction in the SR-LTT control region. The resulted total number of MC events is listed in table 5.6 and compared to the MC prediction for the Z + jets contribution in the signal region. Both numbers have large errors coming from limited statistics. The two results are consistent within the associated uncertainties.

Table 5.6: Comparison between the number of events obtained using the fake-factor method only using MC predictions (top row) and the Z + jets SHERPA MC prediction for the signal region.

	Total events
Fake-factor method	9.6 ± 2.5
MC prediction	6.3 ± 3.8

Normalisation of the diboson background

An additional source of uncertainty that is checked is the change in the number of diboson events. As the contributions coming from backgrounds that have three real leptons have to be subtracted when using the fake-factor method, a change in the final number of estimated Z + jets events can appear when modifying the diboson number of events. The scaling factor that is used for fixing the diboson normalisation is 1.47±0.08, therefore, the Z + jets contribution was re-derived using the upper and lower variations. This results in a very small overall effect. By scaling the diboson background by 1.39 and 1.55, the total number of estimated Z+jets events changed by less than 3.5 %.

Statistical uncertainty propagation

The dominant uncertainty comes from the very low statistics, especially in the all-tight fake-factor region. When propagating these errors to the fake factors, and finally to the Z + jets estimation, this results in an overall uncertainty of 40 %.

Adding a shape uncertainty based on the choice of p_T binning was also investigated. Because of the very low statistics, the estimation is done using only two bins, with the default bin boundaries at 15, 30 and 100 GeV. Two more configurations were tested (15-40-100 and 15-50-100) and it was observed that this had a negligible effect on the shape of the final discriminant used for extracting the tZq cross-section. Because of that, no additional uncertainty was applied.
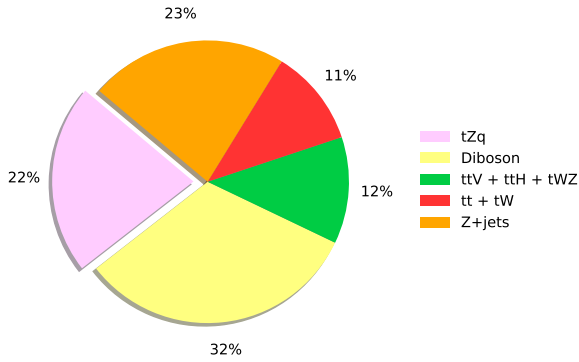
Figure 5.19: Signal and background composition in the SR. For Z + jets, the data-driven estimate is included. The normalisation for $t\bar{t}$ and diboson is corrected as explained in section 5.2.

5.6 Prediction and observation comparison in the signal and validation regions

In order to validate the background estimations, the agreement between data and MC predictions is checked in the SR, as well as the $t\bar{t}$ and diboson validation regions. For all the control plots and event yields tables that are presented in this section, the previously derived $t\bar{t}$ and diboson SFs are applied and for the Z + jets, the data-driven estimation is shown. The quoted errors include the statistical errors, as well as the additional uncertainties on the diboson, $t\bar{t}$ and Z + jets estimates. Any events falling outside the histogram range (overflow) are added to the rightmost bin.

Blinding strategy

Although in the following section the agreement between data and MC prediction is shown for the SR, it is important to note that the analysis was performed *blinded*. This implies that the data in the SR was not checked until the full analysis chain was fixed, including background estimation, neural network separation and fitting procedure. This is done in order to avoid biases in the analysis strategy such as choosing the background estimation that best matches the data. As an initial step in checking the background modelling, the agreement in the $t\bar{t}$ and diboson validation regions was checked.

The SR unblinding was done in two steps. First, a background dominated region was checked. This is defined by applying a cut on the multivariate analysis discriminant used to separate signal and background. The signal to background ratio in these selected events is approximately 0.08. Only after good data/MC agreement is observed for this region, the signal dominated part of the distribution is also unblinded. The plots for these two separated regions are included in appendix A.0.2 and appendix A.0.3.

Signal region

In the SR, 141 events are selected in data. Event displays for two of these events, that have a high probability of coming from tZq production, can be seen in appendix D.

The signal and background composition for this region is shown in figure 5.19. A significant tZq contribution is visible, with the signal amounting to 22 % of the total number of estimated events. The event yields in the SR, separated into four different channels based on the number of electrons and muons in the event ($\mu\mu\mu$, $e\mu\mu$, $ee\mu$ and eee), are given in table 5.7. Overall, good agreement is seen for all four channels. The largest difference is observed in the $e\mu\mu$ channel. This is possibly caused by a slight overestimation of the non-prompt Z + jets background.

The signal and background modelling of some kinematic variables is shown in figure 5.20 and figure 5.21. These control plots include all lepton combinations because of the limited statistics in the

individual channels. The choice of control plots is motivated by the fact that these variables are used in the multivariate analysis, as it is explained in detail in chapter 6. Other variables related to both the input objects, as well as the reconstructed top quark and Z boson were checked and showed no disagreement between data and MC predictions.

Process	$\mu\mu\mu$	$e\mu\mu$	$ee\mu$	eee
tZq	11.3 ± 0.4	9.2 ± 0.4	7.9 ± 0.3	6.8 ± 0.3
$t\bar{t} + tW$	5.2 ± 2.6	6.8 ± 4.5	3.3 ± 1.8	2.6 ± 1.5
$Z + \text{jets}$	4.2 ± 1.9	16.3 ± 6.9	4.6 ± 2.1	11.7 ± 5.0
Diboson	14.8 ± 4.5	14.8 ± 4.5	11.5 ± 3.5	11.5 ± 3.5
$t\bar{t}V + t\bar{t}H + tWZ$	5.5 ± 0.2	5.0 ± 0.2	5.0 ± 0.2	4.4 ± 0.2
Total prediction	41.1 ± 5.6	52.2 ± 9.4	32.3 ± 4.5	37.1 ± 6.3
Data	39	37	27	38

Table 5.7: Event yields in the SR, separated based on lepton flavour. The uncertainties include statistical uncertainties, as well as the additional estimated errors for $t\bar{t}$, diboson and $Z + \text{jets}$.

In figure 5.20, the top row shows properties of the forward jet. As expected, the $|\eta|$ distribution shows all background processes peaking at central values (and a good data/ MC agreement in this background dominated region), while most of the tZq events are expected to have higher η.

The middle row shows the mass distribution of the reconstructed top quark and the p_T of the lepton associated to the W boson. For $p_\text{T}(\ell^W)$, the $Z + \text{jets}$ background populates only the first bins of the distributions, since the non-prompt lepton is expected to have lower p_T. This is also consistent with the $m_\text{T}(\ell_W, \nu)$ distribution in which the $Z + \text{jets}$ background mainly shows up at $m_\text{T}(\ell_W, \nu) < 80\,\text{GeV}$, consistent with the expected non-prompt lepton behaviour and in agreement with the data.

Overall a good agreement between the data and the signal and background predictions is observed in all variables.

Validation regions

Two validation regions are defined. The first one aims at checking the $t\bar{t}$ estimation. This has identical cuts as the SR, except for the cut on the invariant mass of the OSSF lepton pair that is inverted. For the $t\bar{t}$ VR, $m_{\ell\ell}$ is required to be either lower than 81 GeV or above 101 GeV. The second validation region, that is enriched in diboson events, requires one jet and does not have any selection related to the number of b-tagged jets.

The signal and background composition in the two regions is summarised in figure 5.22. The tZq contribution is minimal in both.

Because the $t\bar{t}$ VR has the same selection as the SR region in terms of number of jets and b-tagged jets, the same factors as for SR were used for the estimation of the $Z + \text{jets}$ non-prompt lepton background. In the diboson VR however, the $Z + \text{jets}$ contribution is rederived using the fake-factor method. The fake factors are applied to events in the diboson VR that have a loose-not-tight lepton. The choice for completely recalculating the non-prompt lepton background in this region is motivated by the fact that, in comparison to the SR, no cut is applied on the number of b-tagged jets. Since the origin of non-prompt leptons is mainly semileptonic b decays, it is likely that selections related to heavy flavour jets in the event will have an impact on the total number of events with non-prompt leptons.

The first six variables that were shown for the SR are shown in figure 5.23 for the diboson VR and
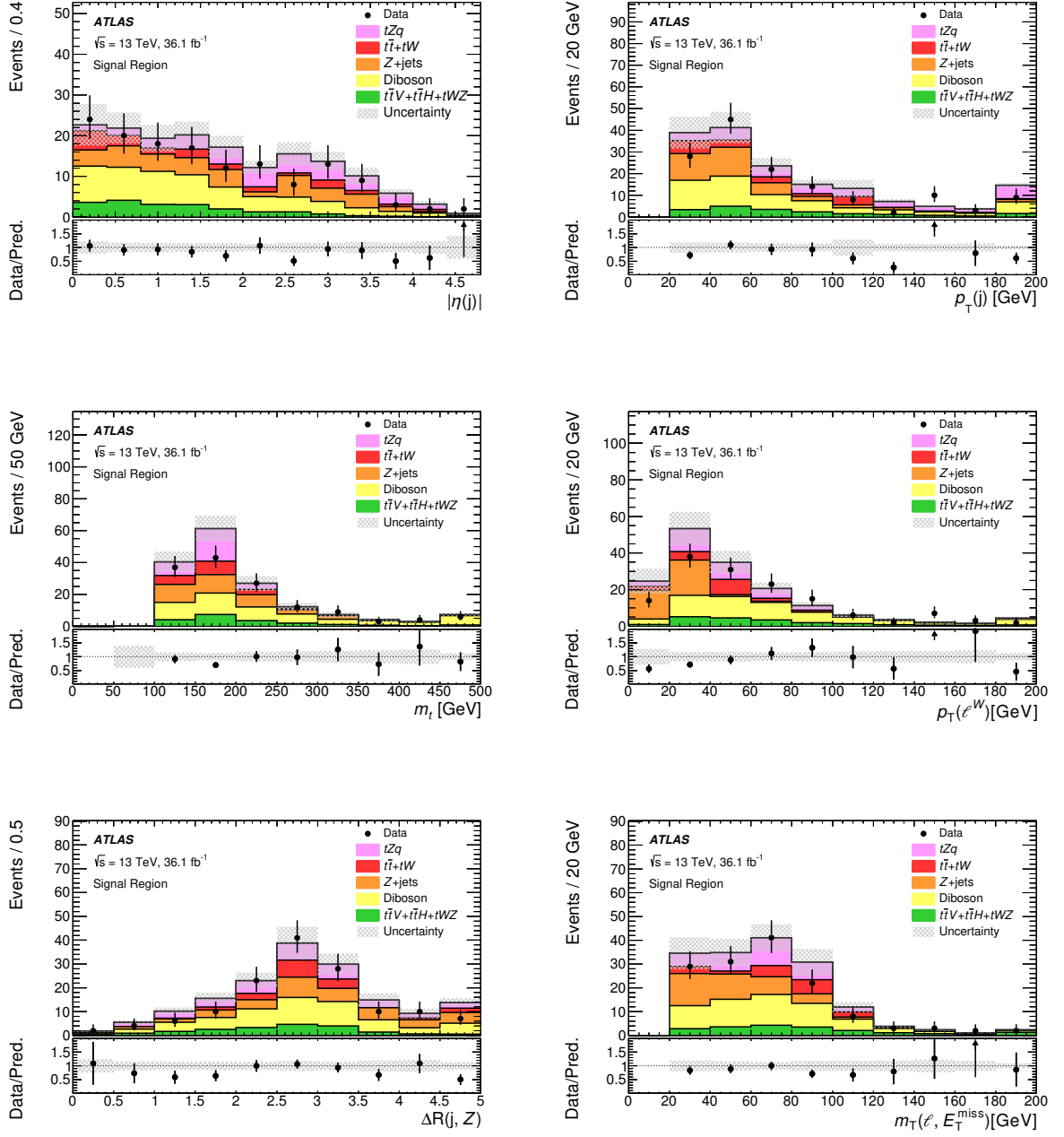
Figure 5.20: Comparison of the data and the signal+background model in the signal region for selected variables. The uncertainty band includes the statistical uncertainty and the uncertainties on the backgrounds derived in section 5.5.
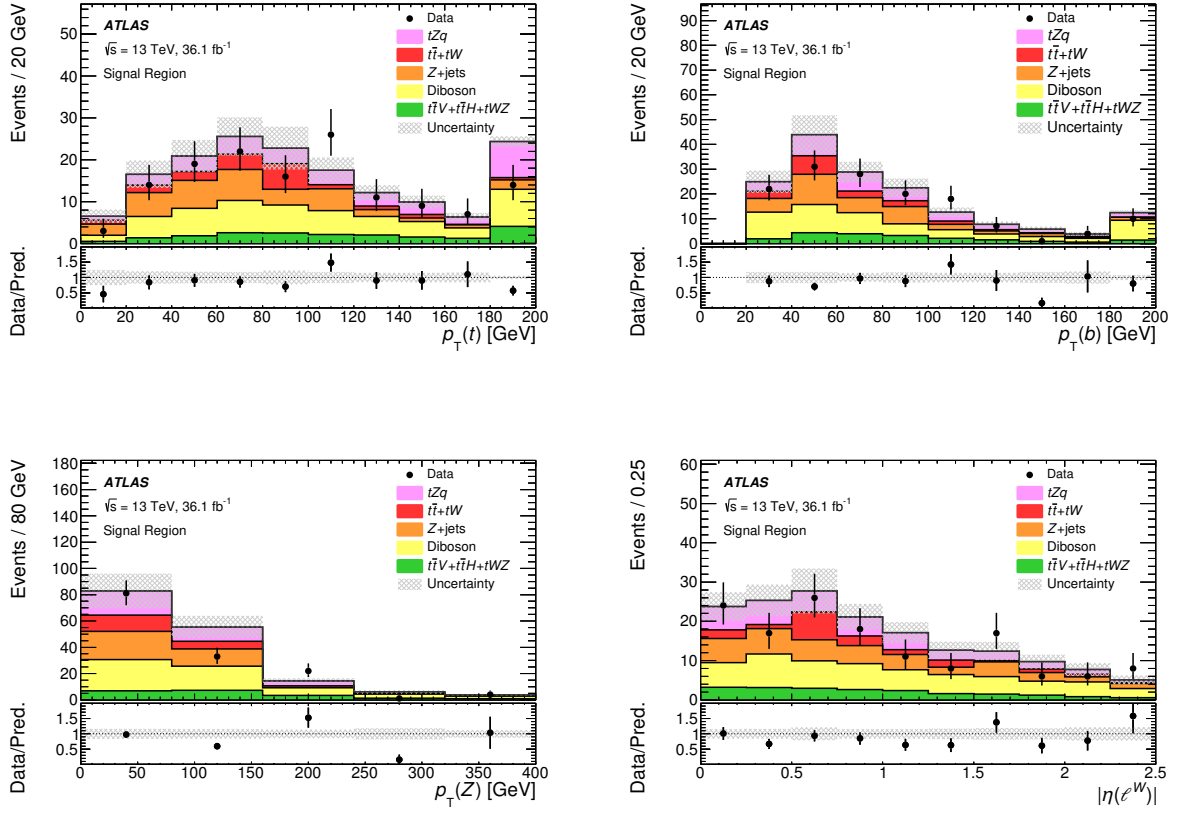
Figure 5.21: Comparison of the data and the signal+background model in the signal region for selected variables. The uncertainty band includes the statistical uncertainty and the uncertainties on the backgrounds derived in section 5.5.
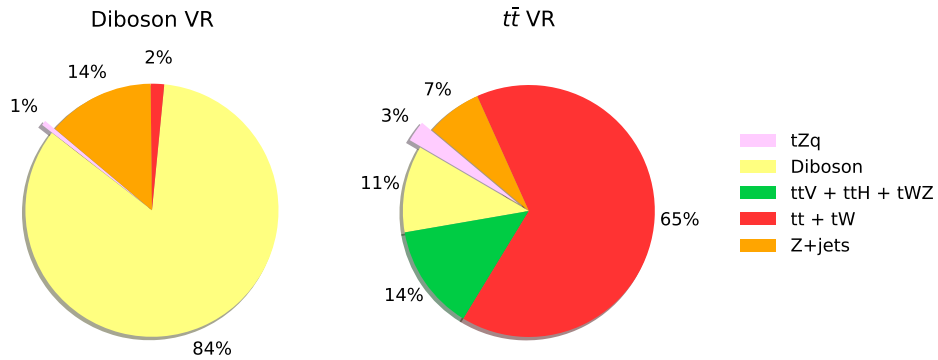
Figure 5.22: Signal and background composition in the diboson and $t\bar{t}$ validation regions. The uncertainty band includes the statistical uncertainty and the uncertainties on the backgrounds derived in section 5.5.

figure 5.24 for the $t\bar{t}$ VR. Good agreement between data and MC can be seen. More VR control plots, as well as the event yields tables for both regions, are included in appendix A.

For the diboson VR, since not all events are required to have a b-tagged jet, variables related to the top-quark or the b-jet are calculated only for a subset of events in which the jet in the event is identified as originating from a b quark. In this case, variables related to the forward jet are also not defined. If the jet selected in this region is not b-tagged, then the b-jet variables are undefined and the top quark is not reconstructed. This explains the different background composition and lower number of events in the m_t in distribution shown in figure 5.23.
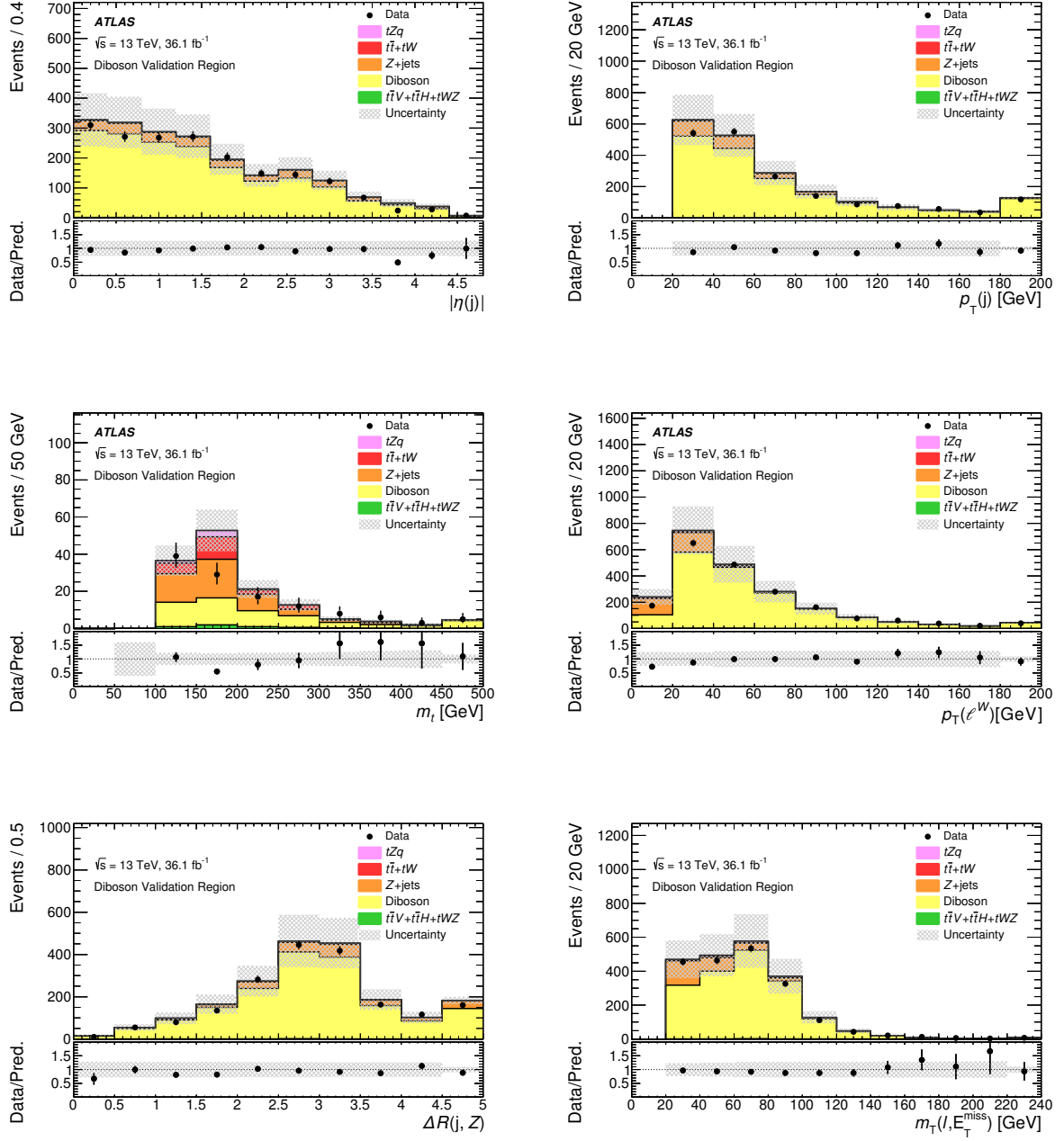
Figure 5.23: Comparison of the data and the signal+background model in the diboson validation region for selected variables. The uncertainty band includes the statistical uncertainty and the uncertainties on the backgrounds derived in section 5.5.
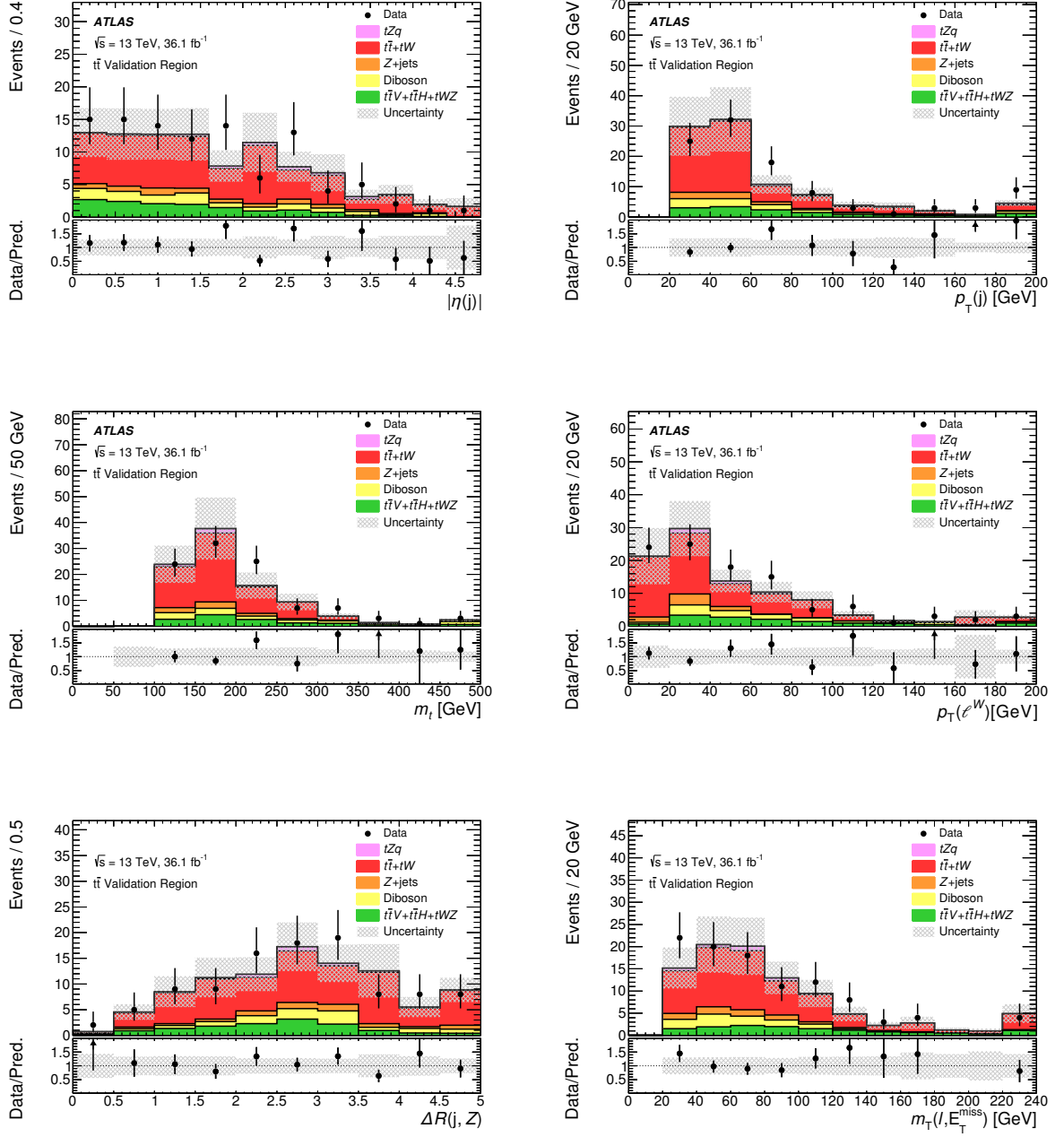
Figure 5.24: Comparison of the data and the signal+background model $t\bar{t}$ validation region for selected variables. The uncertainty band includes the statistical uncertainty and the uncertainties on the backgrounds derived in section 5.5.

Analysis

This chapter aims to give an overview of the procedure and tools used for extracting a cross-section measurement using the data and the expected signal and background events selected as described in the previous chapter. The actual results of the analysis will be presented and discussed in chapter 7.

Section 6.1 gives a short overview of the overall analysis strategy in order to put into context and motivate the techniques and methods described thereafter. Section 6.2 presents the signal and background separation procedure, including a basic description of multivariate classification algorithms (MVAs), with emphasis on the particular setup used in the analysis for obtaining the final discriminant. Section 6.3 gives details about how systematic uncertainties that can modify the rate of the signal and background processes and the shape of the final discriminant are estimated. Several sources of systematic uncertainties are also discussed. The last step of the analysis consists of performing a binned likelihood fit on the MVA output in order to extract the tZq cross-section and estimate the statistical significance of the result. The details of this procedure are described in section 6.4.

6.1 Cross-section measurement analysis strategy

The goal of this analysis is to measure the cross-section of tZq production, as well as estimate the statistical significance of this result. The significance is related to the probability of observing a certain number of events under a certain hypothesis. For this analysis, it is the background-only hypothesis. If the probability is small, the hypothesis is rejected and this will translate to a measurement with large statistical significance. In order to maximise this, it is important to have the signal to background ratio as high as possible, as well as finding variables in which the signal and the background are well separated. This first requirement is achieved by optimising the SR definition as discussed in chapter 4. The second requirement is fulfilled by using a multivariate classification algorithm (in this case an artificial neural network, NN) and constructing a discriminant variable that will have very different values, usually -1 and 1, for background-like and signal-like events respectively.

The NN discriminant is the distribution that will be used for the cross-section measurement. How this distribution (and the number of expected events for each of the signal and background processes) changes due to several systematic uncertainties needs to be evaluated.

This information is included in a binned likelihood fit and a statistical analysis is performed. The goal of it is to extract the observed number of tZq events and its associated uncertainty. This directly translates into a cross-section measurement. The total uncertainty of the result is also calculated.

6.2 Signal and background separation

Most high-energy physics analyses need to solve a classification problem; this is identifying whether the events that we observe (data) are signal or background (or more precisely, how likely it is that these events are signal or background). For most cases, applying selection requirements on individual variables will not be enough to identify a region of phase space in which the observed data is very likely to consist of only signal or only background events.

Because of that, MVA techniques are widely used nowadays in this field. Based on how known events are distributed in the full multidimensional observable space, such algorithms are able to learn to correctly classify other events. For the task at hand, this translates to using all available information (kinematic distributions of the final state particles, reconstructed quantities related to the intermediate particles, general properties of the event) in known signal and background samples, to learn the features of such events and, when presented with a new, unclassified dataset, be able to assign a certain "score" to these events that gives information on how likely it is that this event belongs to one of the two classes[1].

6.2.1 Multivariate analysis techniques: artificial NN

For this analysis, the MVA technique used is an artificial NN. This is a classification algorithm that consists of several *nodes* that have a neuron-inspired structure and are organised in *layers*. Each node can receive input (either from other nodes or externally) and can calculate an output. A variety of networks can be constructed depending on the flow of information through the network, as well as the organisation of the nodes and layers. Here, the focus is kept on the description of a multi-layer network with a feed-forward structure[2]. This is illustrated in figure 6.1, for a network with one layer that passes external information to the network (input layer), one layer that transfers information between the input and output layers (hidden layer) and one layer with a single node (output layer).
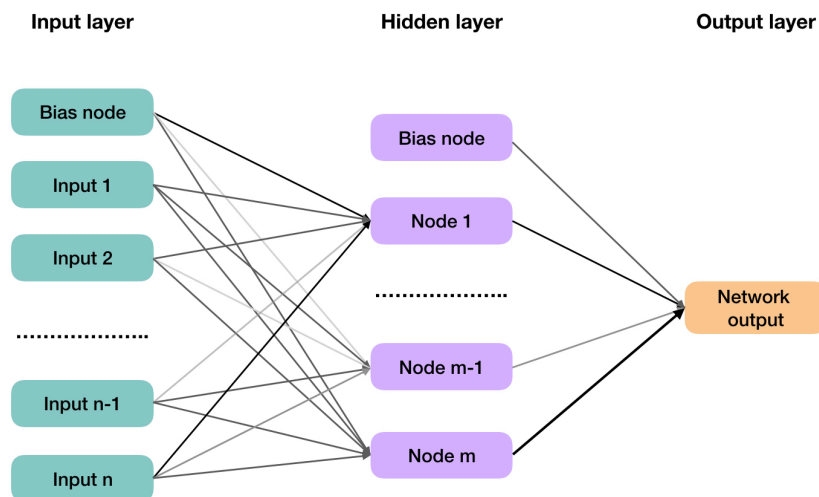
Figure 6.1: Structure of a feed-forward neural network with one hidden layer.

The number of nodes in the input layer is fixed by the number of input parameters and one additional

---

[1] MVA techniques can also be used for multi-class classification. In this thesis only binary classification algorithms are described.

[2] In feed-forward neural networks, information only flows in one direction, from the input layer, through hidden layers and into the output layer.

bias node. The role of the bias node is to add a constant value for the nodes in the next layer, thus allowing the classifier to linearly shift the decision boundary. In the hidden layer, the number of nodes can be optimised by the user. Each of the inter-layer connections is assigned a weight that quantifies the importance of the input parameter with respect to the other input parameters. In the example shown in figure 6.1, the network is given a set of features (variables), $X = x_1, x_2, ...x_n$. Taking a closer look at node j in the hidden layer, this will have an output that can be written as:

$$x_j = \mathcal{F}(w_{0j} + \sum_{i=1}^{n} w_{ij}x_i),$$

where w_{0j} corresponds to the bias term and w_{ij} is the weight of the input feature x_i. $\mathcal{F}$ is called the activation function. This output is used for deciding whether the node will be considered as activated by outside connections. Popular choices for activation function in classifiers are the sigmoid function $h(t) = 1/(1 + e^{-t})$, or $h(t) = \tanh(t)$.

In order to have predictive capabilities, the network must undergo a training phase. This means that given a set of input parameters with known correct classifications, the network must find the set of weights that correctly classify the data. Technically this is done by minimising a loss function that quantifies the level of disagreement between the correct classification and the obtained output. Initially, all weights are assigned randomly. An output is calculated with these random weights and compared with the known result. The error is then propagated back through the network. The weights are adjusted accordingly using algorithms such as gradient descent [105] in order to reduce the error at the output level. This procedure is repeated using all the entries in the training samples. The NN training with the previously calculated weights can then applied to a dataset with unknown classification.

One of the things that need to be checked is that the network is not overtrained. This occurs when the NN starts learning detailed features that actually come from statistical fluctuations. Some protection against that is usually built into the NN architecture by including regularisation parameters that penalise events with large weights or a procedure to randomly drop nodes in the network.

The NeuroBayes package

For the training of the *tZq* signal against background events, the NeuroBayes package is used [106, 107]. This includes an implementation of a complex preprocessing procedure and a feed-forward NN with one hidden layer. For this classification purpose, the output of this package yields the Bayesian posterior probability of the data to be signal-like.

The role of the preprocessing step is to help the network in the minimisation step by avoiding problems related to the complexity of performing optimisation in many dimensions. Variables can be preprocessed both globally and individually. For the training used in this analysis, all variables were transformed simultaneously. In the first step each variable is decorrelated and normalised. Afterwards, the variables are transformed to Gaussian distributions with width 1 and mean 0. The variables are also sorted according to their separation power. This is quantified using a significance determined in an iterative procedure by removing each variable one at a time and recording the loss of total significance that is observed once that particular variable is removed.

Additionally, NeuroBayes includes advanced regularisation techniques based on Bayesian statistics and outputs several figures of merit that are used to check that the network is not overtrained.

6.2.2 NN training to separate *tZq*

A NN is trained to distinguish *tZq* events from events coming from the background processes. The training is done using MC generated samples. Because it has very low statistics, the $t\bar{t}$ sample is not used. All other backgrounds are included.

The NeuroBayes parameters were optimised in order to maximise signal and background separation. The final configuration that was used sets the number of nodes in the hidden layer to 14.

A list of 26 variables is used as input for the preprocessing procedure. This includes all kinematic variables of the final objects, classified according to the final state particle that they are associated to, as well as variables related to the reconstructed top quark and *Z* and *W* bosons. Only variables with significance above 3σ are used in the training.

The variables that are selected in the preprocessing step and then used in the NN training are shown in table 6.1, along with the corresponding significance. It is important that for all these variables, the data is well modelled by the MC predictions. These were checked for the SR and already shown in figure 5.20 and figure 5.21.

Table 6.1: Variables used as input to the neural network, ordered by their separation power.

Variable	Significance(σ)	Definition
$\lvert\eta(\mathrm{j})\rvert$	18.95	Absolute value of untagged jet η
$p_\mathrm{T}(\mathrm{j})$	18.53	Untagged jet p_T
m_t	15.22	Reconstructed top-quark mass
$p_\mathrm{T}(\ell^W)$	8.87	p_T of the lepton from the *W*-boson decay
$\Delta R(\mathrm{j}, Z)$	6.66	ΔR between the untagged jet and the *Z* boson
$m_\mathrm{T}(\ell, E_\mathrm{T}^\mathrm{miss})$	5.25	Transverse mass of *W* boson
$p_\mathrm{T}(t)$	3.86	Reconstructed top-quark p_T
$p_\mathrm{T}(b)$	3.12	Tagged jet p_T
$p_\mathrm{T}(Z)$	3.06	p_T of the reconstructed *Z* boson
$\lvert\eta(\ell^W)\rvert$	3.05	Absolute value of η of the lepton coming from the *W*-boson decay

In order to better understand why this particular set of variables is chosen, their shape is compared for all signal and background processes. This is shown in figures 6.2 to 6.3. All distributions are normalised to the total number of events in the respective sample. The low statistics $t\bar{t}$ sample is shown with a dashed line. The two most significant variables are related to the untagged jet. The η and p_T of this object help with separation against all other backgrounds; the *tZq* shows a higher p_T, as well as an angular preference towards the forward direction. Variables related to the top quark, such as m_t or $p_\mathrm{T}(t)$, help differentiate between the signal and diboson or Z + jets events. Other variables, such as $\lvert\eta(\ell^W)\rvert$, $m_\mathrm{T}(\ell_W, \nu)$ and $p_\mathrm{T}(\ell^W)$, are particularly good in separating the signal from Z + jets events, since, for this background, the lepton associated to the *W* boson is the non-prompt lepton.

By combining information from all these distributions, the NN achieves maximum separation between signal and all backgrounds included in the training.

Training results

A figure of merit for the NN training described above is given in figure 6.4. This shows how the signal efficiency varies with respect to the overall efficiency. The orange line (right side of the plot) corresponds to the case in which the events are not sorted (they are randomly distributed), for the case in which the
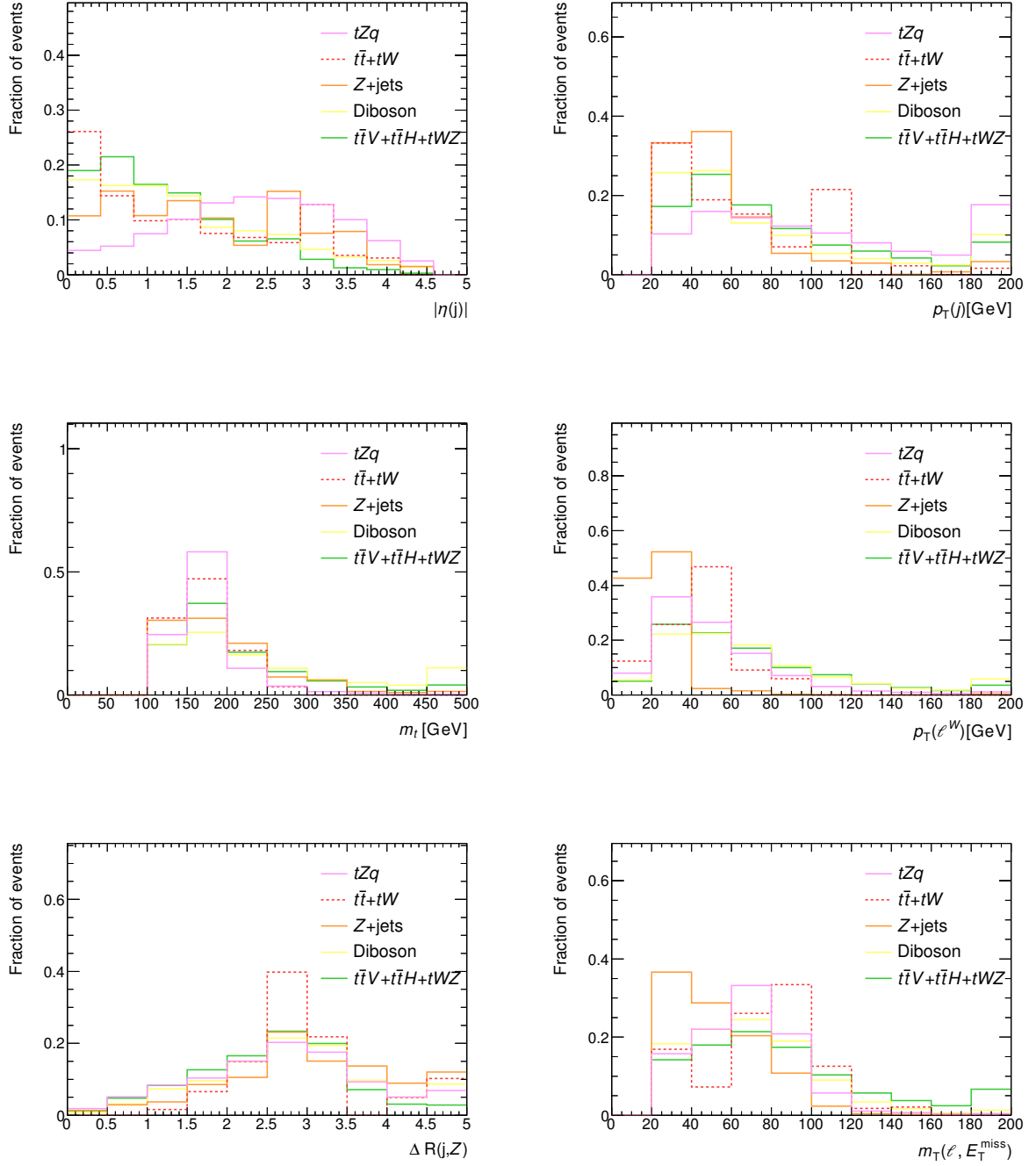
Figure 6.2: Comparison of the signal and background shapes for the neural network training variables in the SR. All the plots are normalised to the total number of events in that sample.
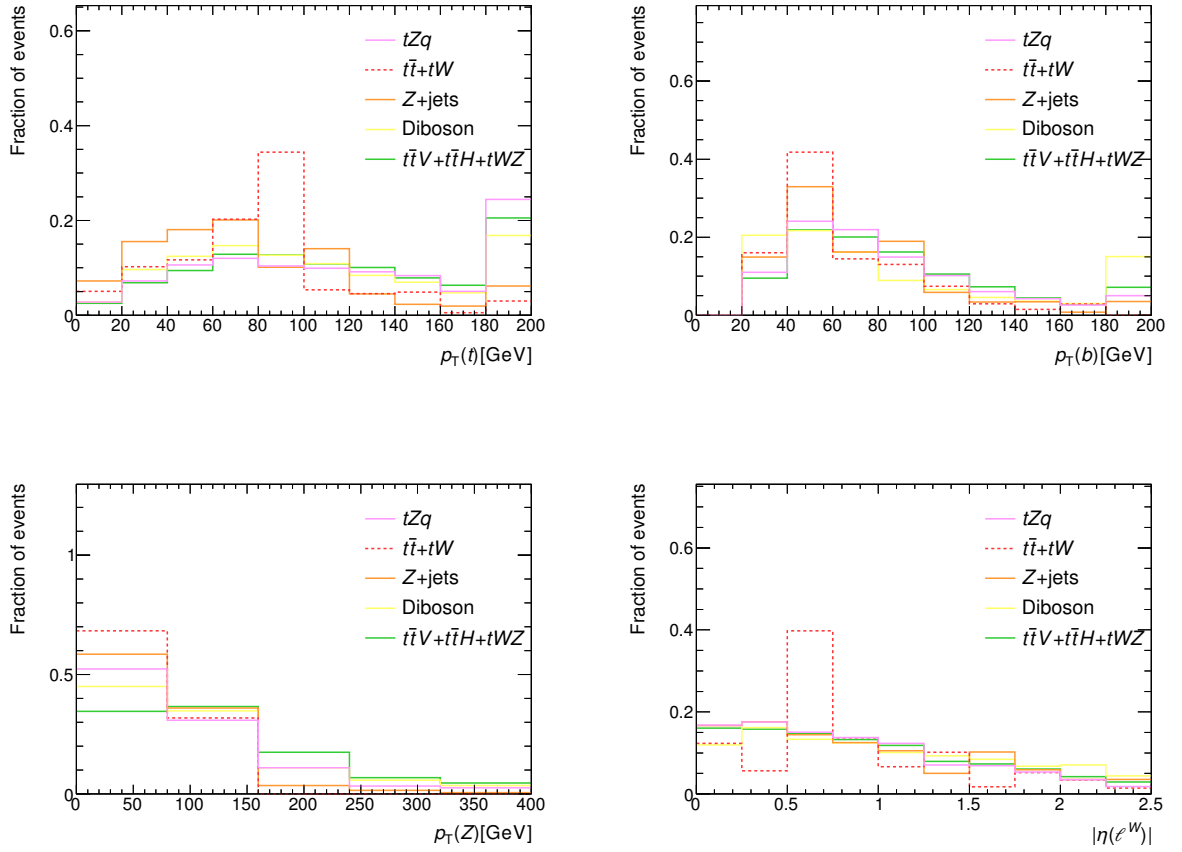
Figure 6.3: Comparison of the signal and background shapes for the neural network training variables in the SR. All the plots are normalised to the total number of events in that sample.

signal and background contributions are equal. In this situation, if one applies a cut on the NN output that will remove half of the events (50% efficiency), this will result in a loss of half of the signal events (50% signal efficiency). The green line (left side of the plot) is the ideal result for a network in which all events are correctly sorted. The blue curve is what is obtained for the NN training used in the analysis. This shows very good separation between signal and background, with the area under the curve being 38.1% out of a maximum possible of 50%.
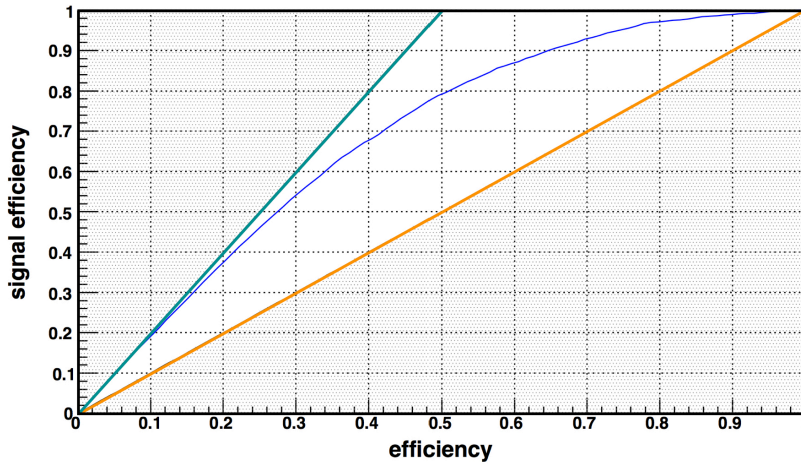
Figure 6.4: Signal efficiency vs. total efficiency plot for the NN training used to separate signal and background events.

The shape of the NN discriminant obtained by applying the NN training to all signal and background samples is shown in figure 6.5. The plot shows for each sample, the fraction of events in each bin of the network output. The number of bins is optimised in order to achieve the best expected significance of the final result. The usual [-1,1] range of the network is mapped to positive values, between 0 and 1, due to inability of the program used for the binned likelihood fit to handle negative values. All backgrounds have NN output values close to 0 and the contamination in the signal dominated region ($O_{NN} > 0.8$) is minimal. Because it was not included in the training sample, the $t\bar{t}$ background has a somewhat flatter distribution compared to all other backgrounds but it still does not have a significant impact in the last two bins of the discriminant.

In order to validate the multivariate analysis procedure, the same NN training is applied on events from the VRs. This is shown in figure 6.6 for the diboson VR (left) and $t\bar{t}$ VR (right). The signal and background samples are normalised to the SM predictions. Good agreement between data and MC is observed as well as a consistent behaviour of the NN when it comes to identifying signal and background like events in completely independent data samples and in different regions of phase space.

For the diboson VR, the variables used in the training cannot all be simultaneously calculated, since only events with one jet are selected. If the jet is not b-tagged, all variables related to the forward jet will be correctly defined. Top quark related variables, as well as $p_{\text{T}}(b)$, are assigned a preset value that is interpreted by NeuroBayes as being undefined. If the jet in the event is b-tagged, the reverse strategy is applied, with all the untagged jet related variables being flagged as undefined.
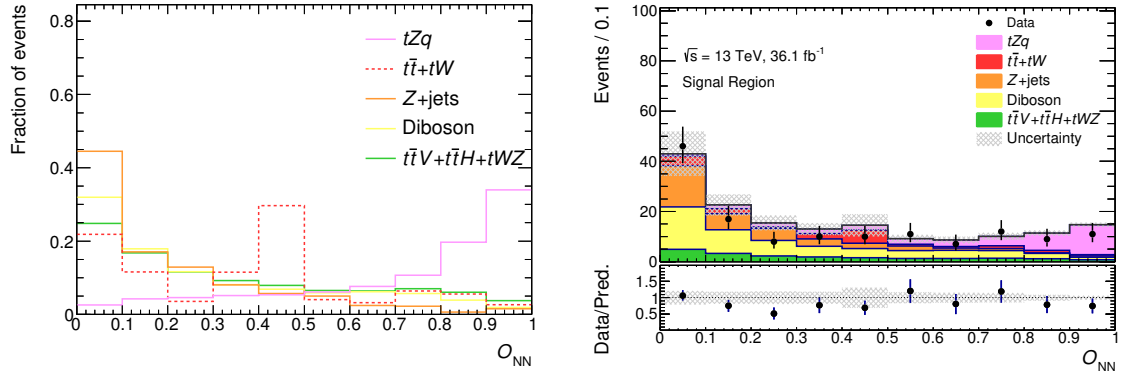
Figure 6.5: Neural network discriminant distribution in the SR as overlay (left) and stack plot (right). The overlay plot shows the comparison of the signal and background distributions normalised to the total number of events in each sample. The uncertainty band includes the statistical uncertainty and the uncertainties on the backgrounds derived in section 5.5.
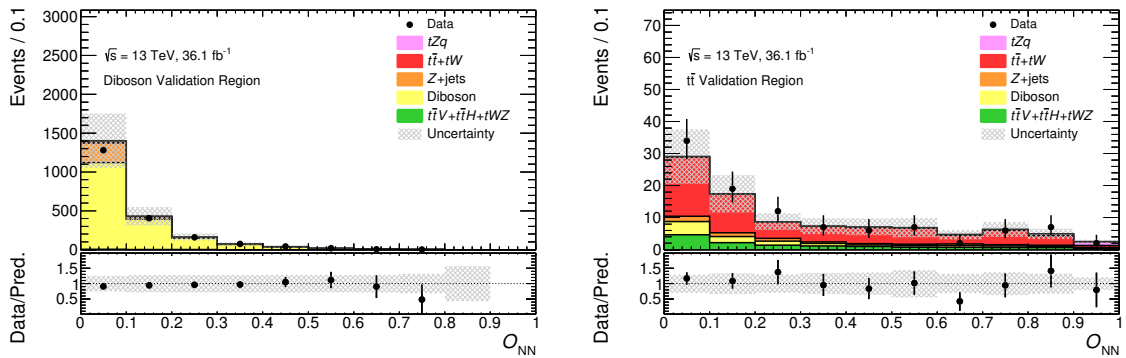
Figure 6.6: Neural network output distribution of the events in the diboson (left) and $t\bar{t}$ (right) validation regions. Signal and backgrounds are normalised to the expected number of events. The uncertainty band includes the statistical uncertainty and the uncertainties on the backgrounds derived in section 5.5.

6.3 Systematic uncertainties

Broadly speaking, systematic uncertainties are any uncertainties that are not directly caused by data statistics. Typically, any step that is performed in the analysis can introduce an uncertainty on the final measurement. The different sources of systematic errors that are taken into account in this analysis are discussed below.

In order to evaluate the impact of each uncertainty, systematic variations of $+/-1\sigma$ around the nominal value are considered. These are referred to as the up and down variations of the systematics. The effect of each of the uncertainties is reflected in a change of signal and background rates and changes in the shape of the NN discriminant that is used for signal extraction. For example, an uncertainty on the cross-section of a process will only change the total number of events estimated for that process (rate uncertainty), while varying a quantity such as the jet energy scale could change the events that pass the SR selection, effectively modifying the number of events in each bin of the NN discriminant by different amounts (shape uncertainty).

6.3.1 Sources of systematic uncertainties

Several sources of systematic uncertainties are considered and their effect on both signal and background predictions is evaluated. These arise due to imprecise knowledge of the detector acceptance, calibrations and resolutions, choice of input parameters in the MC simulations, imprecise measurement of the luminosity or uncertainties on the method used for background estimation.

Object reconstruction and calibration related uncertainties

Different sources of systematic uncertainties related to the reconstruction and calibration of physics objects are considered.

Common methods for accurately measuring the properties of a reconstructed object (such as the energy scale or resolution) include using events with "clean" topologies (leptonically decaying Z bosons for lepton properties, dijet or Z/γ+jets events for jets) and then comparing results between data and MC simulations. Uncertainties on these measurements can arise from the choice of MC generators, selection criteria or poor data/MC agreement.

- **Lepton reconstruction, isolation and identification efficiencies**
  The procedure for obtaining the electron and muon reconstruction, identification and triggering efficiencies was presented in section 3.3. The MC efficiencies are corrected in order to match the ones in data via dedicated scale factors. This is done by selecting events that have a clear leptonic signature, such as $Z \rightarrow \mu^+\mu^-$ and $Z \rightarrow e^+e^-$ events. In order to measure the efficiencies in these samples, a set of selection criteria is applied to minimise background contamination and any remaining background contribution needs to be estimated. The uncertainty on the lepton SFs is derived by varying these selection criteria, as well considering the uncertainty on the background estimation.

- **Lepton momentum scale and resolution**
  For both electron and muons, the determination of the momentum scale and resolution is done using $Z \rightarrow \ell\ell$ and $J/\psi \rightarrow \ell\ell$ events For muons, separate components of the uncertainty are evaluated for the ID and MS [108].

- **Jet energy scale**

  The JES measurement procedure was discussed in section 3.3.3 and an overview of the total associated uncertainties was shown in figure 3.8. The JES uncertainty is evaluated by changing the energy scale of the reconstructed jets and has a total of 80 individual terms that are propagated from different steps in the calibration and additional studies. The majority (67 of them) come from the in situ calibration techniques, either from propagation of lepton and photon related uncertainties, MC simulation or sample statistics. The other terms are related to pile-up treatment, determination of jet flavour or punch-through corrections.

  For easier implementation and evaluation in analyses, the complete set of uncertainties undergoes a global reduction procedure, that leads to a smaller number of nuisance parameters. The configuration used for the *tZq* analysis has 19 NPs. This is done by reducing the 67 in situ related NPs to 6. 5 of them correspond to the leading components in terms of magnitude, while the last one is the quadratic sum of the rest of the parameters [109].

- **Jet energy resolution**

  Several sources of systematic uncertainty can modify the measured energy resolution of a jet. These are mainly related to the in situ methods used for the determination of the resolution. This is done in systems in which the jet is p_T balanced against a well measured object (Z +jet, γ+jet, dijet). The ATLAS recommendations for the JER uncertainty are an extrapolation of Run 1 uncertainties. This procedure also contributes to the total uncertainty [110]. All components are combined into a single JER nuisance parameter.

- **Jet flavour tagging**

  Several nuisance parameters are used for the parametrisation of the uncertainty on the flavour tagging efficiency of the MV2c10 tagger. They are separated into different bins related to b-tagging, c-tagging and light-flavour jet-tagging efficiencies. Additionally, uncertainties resulting from using jets above the p_T calibration range are also taken into account.

  The b-tagging efficiencies and mis-tag rates have been measured in data using the same methods as described in [111, 112] and updated using the 2015 data set.

- **JVT**

  An uncertainty associated to the JVT scaling factor is assigned. This is estimated by taking into account differences observed when using different MC generators in Z + jets events, statistical uncertainty and additional uncertainty due to residual pile-up contamination.

- **Missing transverse momentum**

  Uncertainties on the determination of the E_T^{miss} are taken into account. In total three components are included. These are derived from data MC comparisons of the p_T balance between the soft and hard E_T^{miss} components. Uncertainties due to the scale and resolution (parallel and perpendicular to the p_T (hard) axis) are covered [78]. Uncertainties related to the jet energy scale and resolution are also propagated to the E_T^{miss} calculation.

- **Pile-up reweighting**

  The uncertainty due to the pile-up reweighting procedure (that was discussed in section 4.2) is obtained by varying the nominal factor used for correcting the $\langle\mu\rangle$, according to the official ATLAS recommendations. The μ rescaling factor is changed from 0.91 to 0.84 and 1.0.

Background rate uncertainty

The normalisation uncertainties assigned to the backgrounds that include a non-prompt lepton were discussed in section 5.5.2. These are 42 % for the $t\bar{t}$ background and 40 % for Z + jets.

An uncertainty on the normalisation of the diboson background is derived by comparing the nominal estimation in the SR obtained with the LO SHERPA samples with the estimation obtained using an alternative set of NLO POWHEG MC samples. The difference is evaluated after the MC is scaled according to the procedure described in section 5.5.1. This results in a prediction for the SR of 52 diboson events using SHERPA and 37 events using POWHEG. This corresponds to a 29 % difference and is rounded up to a final 30 % uncertainty on the diboson normalisation.

For the $t\bar{t}V$, $t\bar{t}H$ and tWZ contributions, the MC samples are used and normalised to their predicted cross-sections. An uncertainty of 13 % on the rate of these background processes is assigned, accounting for the choice of scale and PDF in the cross-section calculation [89].

MC related uncertainties

- **Modelling uncertainties**
  Effects coming from MC modelling are evaluated by comparing different MC generators or varying parameters at event generation level. For the diboson background, in order to check the difference between NLO and LO generated events, the SHERPA and POWHEG +PYTHIA samples are used. The effect on the normalisation was discussed in the previous section, resulting in a rate uncertainty. The shapes of the NN discriminant were compatible using the two samples so no shape uncertainty was assigned for the diboson background.

  For $t\bar{t}Z$, in order to assess if there is any significant uncertainty due to the choice of showering algorithm, two different samples are compared and the effect on the NN output shape was studied. The default MADGRAPH + PYTHIA 8 samples were compared with an alternative set of samples generated with SHERPA 2.2. The shape of the NN discriminant was compatible between the two samples; no additional shape uncertainty was assigned for the $t\bar{t}Z$ background.

  For the $t\bar{t}$ background, the modelling uncertainties were evaluated by comparing different MC generated samples. The low statistics in the $t\bar{t}$ samples makes it difficult to distinguish statistically significant effects on the shape of the NN distributions of the two samples. Because of that, the shape uncertainty due to the modelling of this background was not included.

  The signal modelling uncertainties have the largest impact on the result of this analysis. The effect of the choice of scale and additional radiation is evaluated using alternative MC signal samples. These have simultaneous variations of the renormalisation and factorisation scales and the amount of radiation included. A scale change by a factor of two is combined with a set of tuned parameters with lower radiation, while for the sample with both scales modified by a factor of 0.5, a set of parameters with higher radiation compared to the nominal is used. These combinations are chosen because they conservatively cover the effects coming from the choice of scale and radiation. The NN output distribution for the signal sample, along with the up and down scale variations are shown in figure 6.7. This uncertainty has a significant effect on the number of signal events; this is particularly visible in the high O_{NN} bins.

- **PDFs**
  Additionally, for tZq, the uncertainties due to the parton distribution functions are investigated. This is done according to the PDF4LHC recommendations and uses 30 eigenvectors of the PDF4LHC15 NLO PDF set [113]. The effects of changing the PDF are evaluated by reweighting
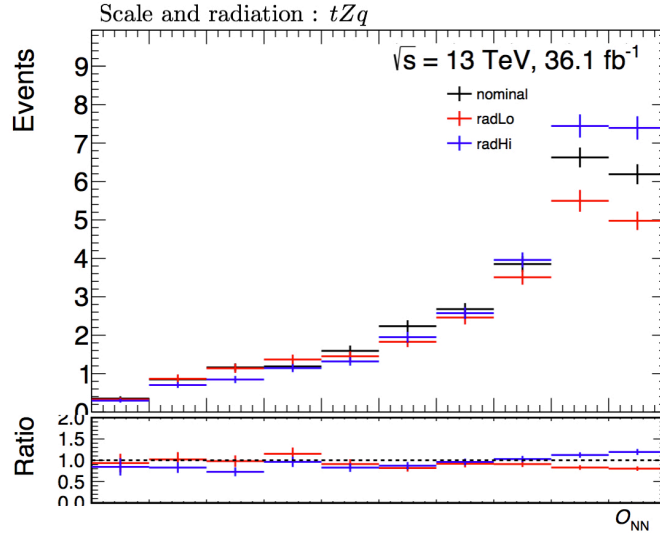
Figure 6.7: Comparison of the nominal *tZq* NN output distribution and the up and down variation of the scale and radiation signal uncertainty.

events using each of the eigenvectors. The overall effect on the signal rate and shape of the NN discriminant is small.

- **MC statistics**
  Because the MC samples have limited statistics, the effect of statistical fluctuations is considered. This is done using the Barlow-Beeston light method [114] and accounts for statistical fluctuations in the number of signal and brackground predicted events in each bin of the NN discriminant.

Luminosity

An uncertainty on the luminosity measurement is provided by the ATLAS collaboration. For the 2015 and 2016, this is 2.1 %. This is evaluated using the strategy presented in [80], from a calibration of the luminosity scale using *x*–*y* beam-separation scans performed in August 2015 and May 2016.

6.3.2 Systematic uncertainties evaluation

Rate uncertainties

For each uncertainty affecting the rate of a process, the relative variation of the signal and background acceptance of the up and down variation of the systematic uncertainties with respect to the nominal can be calculated. This will be denoted by $\delta^{\pm}$ for the up and down variation respectively. This effectively shows the estimated effect of each uncertainty on the rate of a particular process. The rate changes for signal and all backgrounds are summarised in table 6.3 for both positive and negative variations of the uncertainties. This table does not include the background rate uncertainties that are assigned to individual processes. These are listed in table 6.2 and have been discussed in more detail in section 6.3.1.

All rate uncertainties listed in table 6.3 have an effect of less than 10 %. The largest changes are seen for the JER. This causes a change of up to 8.8 % for the $t\bar{t}$ normalisation and has a 4 % effect on the signal. Similarly large changes are also caused by the JES parameter related to the flavour composition uncertainty. This has an effect of up to 6.4 % on the $t\bar{t}V + t\bar{t}H + tWZ$ template and 7.4 % on the $t\bar{t}$

normalisation. Because of this, it is expected that these uncertainties are among the ones that have a larger impact on the final result.

Process	Uncertainty
$t\bar{t} + tW$	42 %
$Z + \text{jets}$	40 %
Diboson	30 %
$t\bar{t}V + t\bar{t}H + tWZ$	13 %

Table 6.2: Summary of normalisation uncertainties for the background processes.

Shape uncertainties

Shape uncertainties are included for systematic sources that modify the shape of the NN discriminant. For all signal and background processes, templates using the positive and negative systematic variation are considered. However, before using these in the fit, a pruning and symmetrisation procedure is applied.

- **Pruning:** The pruning procedure is in place in order to avoid any overestimation of the shape uncertainties in samples that have very low statistics after performing the event selection. This ensures that if any of the upward or downward fluctuation is consistent with statistical noise, the corresponding shape template is not included in the fit. This is done by calculating:

$$p = \frac{1}{N_{\text{bins}}} \sum_{i}^{N_{\text{bins}}} \frac{(N^{i}_{\text{variation}} - N^{i}_{\text{nominal}})^2}{N^{i}_{\text{nominal}}},$$

where N_{bins} is the number of bins in the distribution (10 for the NN discriminant), N^{i}_{nominal} is the number of entries in bin i of the nominal template and $N^{i}_{\text{variation}}$ is the number of entries in bin i of the upward or downward variation of the systematic under investigation.

  Different threshold values for p were tested and a value of 0.005 was chosen because it ensures the removal of all templates that are consistent with statistical fluctuations. For systematics that have a calculated $p < 0.005$, the shape component will not be taken into account. The rate uncertainty is still taken into account. All of the shape systematics templates that are dropped by the pruning procedure are related to the $t\bar{t}$ background. This is explained by the fact that, after applying the SR selection, this sample has very low MC statistics.

  An example plot for a template with $p < 0.005$ is shown in figure 6.8. This shows the NN output distribution in the $t\bar{t}$ sample for the nominal and $\pm\sigma$ variations of the JES systematic uncertainty related to the jet flavour composition, before and after the pruning procedure is applied. The complete list of templates that are rejected by the pruning algorithm can be found in section 6.3.2.

- **Symmetrisation:** The symmetrisation of the templates is in place in order to avoid cases in which, due to low statistics, both upward and downward fluctuations of a systematic uncertainty are on the same side of the nominal template or in which asymmetric templates are included in the fit. These can lead to fit instabilities, as well as an overestimation of the uncertainties.

  All templates that are included in the fit are thus symmetrised around the nominal value. This procedure is done bin-by-bin. For bins in which the $+$ and $-\sigma$ variations are on opposite sides

Systematic	tZq δ^+	δ^-	diboson δ^+	δ^-	$t\bar{t}V + t\bar{t}H$ δ^+	δ^-	$t\bar{t}$ δ^+	δ^-
$e^{\pm}/\gamma$ Resolution	−0.1	0.0	0.3	0.1	−0.1	−0.1	1.5	−6.6
$e^{\pm}/\gamma$ Scale	0.0	0.1	−0.2	0.1	−0.2	0.0	−0.7	−4.5
JES BJES_Response	0.0	0.5	−0.2	0.0	0.3	−0.4	−1.7	1.6
JES EffectiveNP_1	0.5	−0.2	0.2	0.1	2.3	−3.1	−3.2	−0.4
JES EffectiveNP_2	0.4	0.0	−0.3	0.1	−0.6	0.4	−3.5	−1.7
JES EffectiveNP_3	0.0	0.0	0.1	−0.0	0.1	−0.1	−0.0	−1.6
JES EffectiveNP_4	−0.0	0.0	0.0	−0.0	−0.1	0.1	0.0	−0.0
JES EffectiveNP_5	−0.1	−0.1	−0.1	0.1	−0.1	−0.0	−1.6	−1.7
JES EffectiveNP_6	−0.0	−0.0	0.1	−0.1	−0.0	−0.2	−1.7	−1.6
JES EffectiveNP_7	0.0	0.0	0.0	−0.0	−0.0	−0.0	−0.0	0.0
JES EffectiveNP_8restTerm	−0.1	−0.1	0.1	0.1	−0.1	−0.0	0.0	−1.6
JES EtaIntercalibration_Modelling	0.8	−0.0	−0.6	−0.4	1.6	−2.8	−3.1	−0.2
JES EtaIntercalibration_NonClosure	0.2	−0.2	−0.0	−1.2	0.3	−0.6	−0.3	−0.0
JES EtaIntercalibration_TotalStat	−0.2	0.0	0.3	−0.3	0.5	−0.8	−3.1	−3.5
JES Flavor_Composition	1.8	−1.9	−0.7	−0.3	5.9	−6.4	−7.4	2.9
JES Flavor_Response	−0.3	0.8	−0.5	0.5	−2.3	1.4	−2.0	−1.4
JES Pileup_OffsetMu	0.3	0.2	0.2	−0.3	−0.6	−0.1	−0.0	−3.1
JES Pileup_OffsetNPV	0.4	0.1	0.2	−2.0	−0.0	−0.7	−1.6	0.2
JES Pileup_PtTerm	0.2	0.0	−0.1	−0.2	0.1	−0.4	−3.3	−0.0
JES Pileup_RhoTopology	0.9	−0.1	−0.3	1.2	4.1	−4.4	−6.6	1.4
Jet Energy Resolution	4.0	−4.0	1.0	−1.0	1.3	−1.3	−8.8	8.8
$E_{\mathrm{T}}^{\mathrm{miss}}$ Resolution (Para)	−0.0	0.0	0.7	−0.7	0.1	−0.1	0.0	0.0
$E_{\mathrm{T}}^{\mathrm{miss}}$ Resolution (Perp)	−0.3	0.3	0.3	−0.3	−0.1	0.1	0.7	−0.7
$E_{\mathrm{T}}^{\mathrm{miss}}$ Scale	0.1	0.1	−0.6	−0.4	0.1	−0.1	0.0	1.6
Muon ID	0.1	0.3	0.2	−0.1	0.2	0.0	0.0	1.9
Muon MS	−0.1	0.1	0.3	−0.6	0.1	0.0	0.0	3.9
Muon Scale	0.2	−0.1	0.0	−0.1	0.1	0.0	3.9	0.0
b-tagging NP B_0	2.6	−2.6	0.8	−0.9	0.5	−0.6	3.5	−3.5
b-tagging NP B_1	1.0	−1.0	0.2	−0.2	0.2	−0.3	0.9	−0.9
b-tagging NP B_2	−0.5	0.5	−0.1	0.1	−0.1	0.1	−0.6	0.6
b-tagging NP B_3	−0.1	0.1	0.0	−0.0	−0.0	0.0	0.1	−0.1
b-tagging NP C_0	−0.1	0.1	9.5	−9.6	−0.1	0.1	−0.1	0.1
b-tagging NP C_1	−0.1	0.1	2.7	−2.7	−0.0	0.0	0.0	−0.0
b-tagging NP C_2	−0.0	0.0	0.1	−0.1	0.0	−0.0	0.0	−0.0
b-tagging NP C_3	−0.0	0.0	0.5	−0.5	−0.0	0.0	−0.0	0.0
b-tagging NP Light_0	−0.1	0.1	6.2	−6.2	−0.0	0.0	0.5	−0.5
b-tagging NP Light_10	−0.0	0.0	−0.1	0.1	0.0	−0.0	−0.0	0.0
b-tagging NP Light_1	−0.0	0.0	−1.1	1.1	−0.0	0.0	−0.0	0.0
b-tagging NP Light_2	0.0	−0.0	−0.8	0.8	0.0	−0.0	0.1	−0.1
b-tagging NP Light_3	0.0	−0.0	0.2	−0.2	−0.0	0.0	0.3	−0.3
b-tagging NP Light_4	0.0	−0.0	0.1	−0.1	−0.0	0.0	0.0	−0.0
b-tagging NP Light_5	0.0	−0.0	0.1	−0.1	−0.0	0.0	0.1	−0.1
b-tagging NP Light_8	−0.0	0.0	0.1	−0.1	−0.0	0.0	0.1	−0.1
b-tagging Extrapolation	−0.0	0.0	−0.3	0.3	0.0	−0.0	0.0	0.0
b-tagging c Extrapolation	0.0	0.0	−0.1	0.1	0.0	−0.0	0.0	0.0
JVT weight	−0.1	0.1	−0.1	0.0	0.1	−0.2	−0.3	0.3
Electron Identification SF	−1.3	1.5	−1.4	1.6	−1.4	1.6	−1.2	2.1
Electron Isolation SF	−0.2	0.4	−0.3	0.5	−0.3	0.5	0.2	0.6
Electron Reconstruction SF	−0.2	0.4	−0.2	0.4	−0.2	0.4	−0.0	0.8
Electron Trigger SF	0.1	0.1	0.1	0.1	0.1	0.1	0.3	0.5
Muon Identification SF (stat.)	−0.2	0.4	−0.2	0.4	−0.2	0.4	0.0	0.8
Muon Identification SF - low p_{T} (stat.)	0.1	0.1	0.1	0.1	0.1	0.1	0.4	0.4
Muon Identification SF (syst.)	−1.2	1.4	−1.2	1.4	−1.1	1.4	−0.9	1.7
Muon Identification SF - low p_{T} (syst.)	0.1	0.1	0.1	0.1	0.1	0.1	0.4	0.4
Muon Isolation SF (stat.)	0.0	0.2	0.0	0.1	0.0	0.2	0.3	0.5
Muon Isolation SF (syst.)	−0.3	0.5	−0.3	0.4	−0.2	0.4	0.0	0.8
Muon TTVA SF (stat.)	−0.1	0.3	−0.1	0.2	−0.1	0.3	0.1	0.7
Muon TTVA SF (syst.)	−0.0	0.2	−0.1	0.2	−0.0	0.2	0.1	0.7
Muon Trigger SF (stat.)	0.0	0.2	0.0	0.1	0.1	0.2	0.3	0.5
Muon Trigger SF (syst.)	−0.0	0.2	−0.0	0.2	0.0	0.2	0.2	0.6
Pileup	2.5	−3.0	0.7	2.1	1.3	−1.2	−7.3	3.5

Table 6.3: The change in rate in % for each signal and background process due to the positive and negative variation of the systematic uncertainties. Uncertainties with an effect of < 0.1 % on all processes have been omitted.
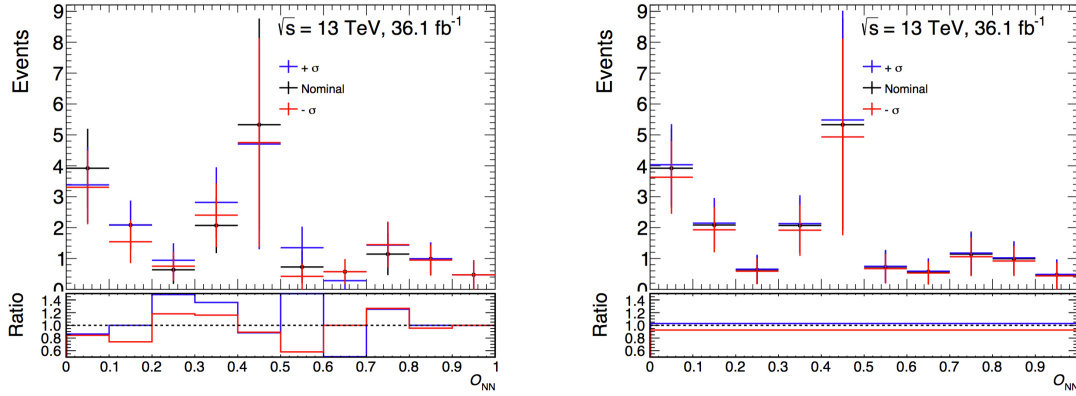
Figure 6.8: O_{NN} distribution of the $t\bar{t}$ sample for nominal and up and down variations of the jet flavour composition uncertainty, before (left) and (after) the pruning procedure.

Systematic	Sample
JES Flavor Composition	$t\bar{t}$
JES Pileup RhoTopology	$t\bar{t}$
JER	$t\bar{t}$
Pileup	$t\bar{t}$

Table 6.4: List of systematic uncertainties for which the shape variation is removed by the pruning algorithm

of the nominal value, the symmetric upward and downward assigned variations are equal to half of the difference between the initial values. This can be written as $\delta_{\text{symm.}}^{\pm} = x_{\text{nominal}} \pm |\delta_{\text{initial}}^{+} - \delta_{\text{initial}}^{-}|/2$, where $\delta_{\text{symm.}}^{\pm}$ are the upward and downward symmetrised variations in a bin, x_{nominal} is the nominal value in the respective bin and $\delta_{\text{initial}}^{\pm}$ are the unsymmetrised upward and downward systematic variations. If in the unsymmetrised template, the up and down variations are both on the same side of the nominal, the largest of the two will be kept and will be assigned symmetrically around the nominal value: $\delta_{\text{symm.}}^{\pm} = x_{\text{nominal}} \pm \max(\delta_{\text{initial}}^{+}, \delta_{\text{initial}}^{-})$.

For systematic uncertainties that have only one variation (such as JER), the available template is symmetrised around the nominal. Figure 6.9 shows the comparison between the nominal and the up and down JER uncertainty variations for the signal and background processes. For $t\bar{t}$, the shape uncertainty is dropped during the pruning procedure and only the rate uncertainty is kept.

6.4 Signal Extraction - Binned Likelihood Fit

In statistics, the likelihood is a measure of how compatible a considered hypothesis is, given the data. Maximum likelihood (ML) estimation is a common method that can be used in order to estimate parameters of a statistical model (e.g. the cross-section of a SM process) using some observation (e.g. *pp* collision data). The set of parameters that maximises the likelihood of observing the data is chosen. The short description of ML estimation is summarised from refs. [115] and [116]. In the most common implementations, instead of maximising a likelihood function $\mathcal{L}$, its negative logarithm, $-2\ln(\mathcal{L})$, is minimised. A common tool used for this minimisation process is Minuit [117].
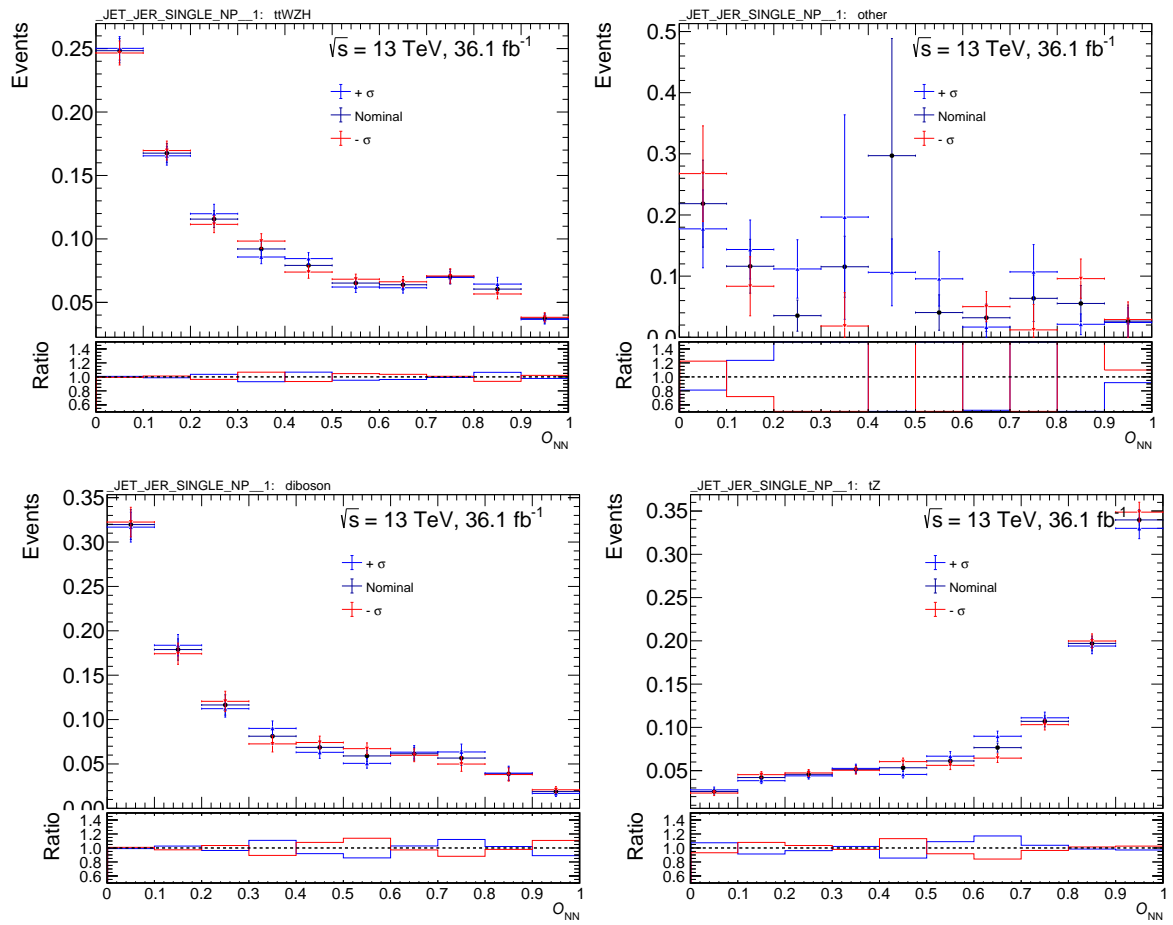
Figure 6.9: Comparison between nominal (in black) and the $+1\sigma$ (in blue) and -1σ (in red) variations of the JER uncertainty for the $t\bar{t}V + t\bar{t}H + tWZ$ and $t\bar{t}$ template (top row) and the diboson and tZq, bottom row.

Since in this analysis the selected events are organised in bins of the NN discriminant, the *tZq* cross-section is extracted by performing a binned likelihood fit. In particular, a profile likelihood fit is used. This includes the description of the systematic uncertainties in the likelihood function, $\mathcal{L}(\mu_{\text{sig}}, \vec{\theta})$. Here, μ_{sig} is the signal strength, defined as the ratio between the measured and the SM predicted *tZq* cross-section; $\vec{\theta}$ is the set of nuisance parameters introduced for characterising the impact of systematic uncertainties on the signal and background events.

The goal of the statistical analysis is to get an estimation of μ_{sig}, as well as its associated uncertainty. In order to do that, all known information about the processes and the uncertainties are included in the likelihood function. This can be expressed as:

$$\mathcal{L}(\mu_{\text{sig}}, \vec{\theta}) = \prod_{i=1}^{B} e^{-\nu_i} \frac{\nu_i^{n_i}}{n_i!} \prod_{j}^{\text{syst.}} \mathcal{G}(\theta_j^0 - \theta_j).$$

The first term reflects the fact that both data and simulation are Poisson processes and hence the probability of observing the data can be written using a Poisson term, where B denotes the number of bins in the distribution and for bin i, ν_i is the number of expected events and n_i is the number of observed events. ν_i can be written as the sum of the signal and background predictions for bin i: $\nu_i = \nu_i^{\text{sig}} + \nu_i^{\text{bkg}}$. The relation between the number of expected and observed signal events in bin i can be written as $n_i^{\text{sig}} = \mu_{\text{sig}} \nu_i^{\text{sig}}$.

The last term is introduced to parametrise the effect of the systematic uncertainties on the expected number of events. Under the assumption that the uncertainties are uncorrelated, this can be written as a product of probability distributions describing each of the systematic uncertainties. Here the uncertainties are parametrised using a Gaussian function with unit width. For each nuisance parameter j, θ_j^0 denotes the nominal value around which θ can be varied during the fit [118]. This is set to 0 for most of the nuisance parameters. According to this, a systematic variation of $\pm 1\,\sigma$ will correspond to a change of ± 1 on θ_j. The only exception are the nuisance parameters associated to the bin by bin MC statistical uncertainties (usually denoted with γ), that are set to 1.

Hypothesis testing is used in order to extract conclusions from a set of measured data. A test statistic must be chosen for determining how good the observations are in agreement with the predictions. The test statistic is defined as

$$q_\mu = -2 \ln[\mathcal{L}(\mu, \hat{\hat{\vec{\theta}}})/\mathcal{L}(\hat{\mu}, \hat{\vec{\theta}})],$$

where $\hat{\hat{\vec{\theta}}}$ is the conditional ML estimate for a particular μ, while $\hat{\mu}$ and $\hat{\vec{\theta}}$ are the global fitted values. For this application, the null-hypothesis that is tested is the "background only" hypothesis, for which $\mu_{\text{sig}} = 0$. q_0 is then used for calculating a p-value as

$$p_0 = \int_{q_{0,\text{obs}}}^{\text{inf}} f(q_0|0) dq_0.$$

This quantifies the compatibility between the observed data and the null-hypothesis in the asymptotic approximation [119]. A small p-value results in a rejection of the null-hypothesis. In particle physics, the significance of the result is often expressed through the number of standard deviations from the hypothesis prediction [120]. This is denoted with Z and is calculated from the p-value as:

$$Z = \Phi^{-1}(1 - p),$$

where Φ is the cumulative function of the unit Gaussian. In high energy physics, a Z-value of 5σ is

conventionally required in order to claim discovery. This corresponds to a p-value of 2.87×10^{-7} [115].

In order to evaluate the sensitivity of an analysis, the statistical procedure can be done without using the real data, but instead looking at a representative data set, referred to as *Asimov data* [119]. Generally, this is a data set for which the true values of parameters are recovered when using it in the estimation procedure. For the *tZq* analysis this translates to having a data set fully consistent with the SM expectation; this is obtained by adding the signal and background MC predictions. By construction, when performing the likelihood fit using this data set, the measured signal strength parameter will be equal to 1. The significance that is extracted using the Asimov data set is referred to as the expected significance and can be used for optimising the analysis strategy.

The statistical analysis procedure was performed using the `HistFitter` [118] framework. This is based on the `HistFactory` [121] and `RooStats` [122] software packages and provides a framework that is specifically tailored for building probability density functions, fitting and providing statistical interpretations of the results.

Results

This chapter presents the results of the *tZq* cross-section measurement. These are obtained using a binned profile likelihood fit that finds the best estimate of the the signal strength parameter, μ_{SIG}, that is used for calculating the *tZq* cross-section, as well as its associated uncertainties. In order to assess the results of the fit, comparisons between *pre-fit* and *post-fit* plots, event yields and uncertainties are studied. In pre-fit plots, all uncertainties are set to their nominal value and the signal and background rates are set to their SM prediction. In post-fit distributions[1], all parameters of the fit (signal strength and NPs associated with the systematics errors) are set to their fitted values. The normalisation of each background can also change within its associated uncertainties.

Section 7.1 summarises the expected fit results that are obtained by performing the binned likelihood fit on an Asimov dataset. The first part of the section gives a description of the uncertainty ranking plots and their interpretation; this general information applies also for the data fit results that are presented in section 7.2. Section 7.3 gives a discussion of the results, including a detailed comparison with the recent *tZq* cross-section measurement published by the CMS experiment.

7.1 Expected fit results

The expected result is extracted by fitting the NN output distribution using a binned profile likelihood fit on an Asimov dataset, discussed in section 6.4. This is obtained by setting all the predicted signal and background processes to their SM predictions.

The pre-fit and post-fit distributions of the NN discriminant are shown in figure 7.1. As the Asimov data, marked with black points in the plots, is the sum of the MC predictions, the fit does not modify the number of background events and yields a signal strength parameter of 1. However, performing this fit is useful for assessing the behaviour and impact of systematic uncertainties, as well as the sensitivity and discovery potential of the analysis. This is performed before looking at the data for any blinded analysis. This ensures that no biases are introduced in the analysis strategy by looking at the data points, while still getting an idea of the expected results.

---

[1] All post-fit plots shown in this chapter that have the "ATLAS" label, are included from [1].
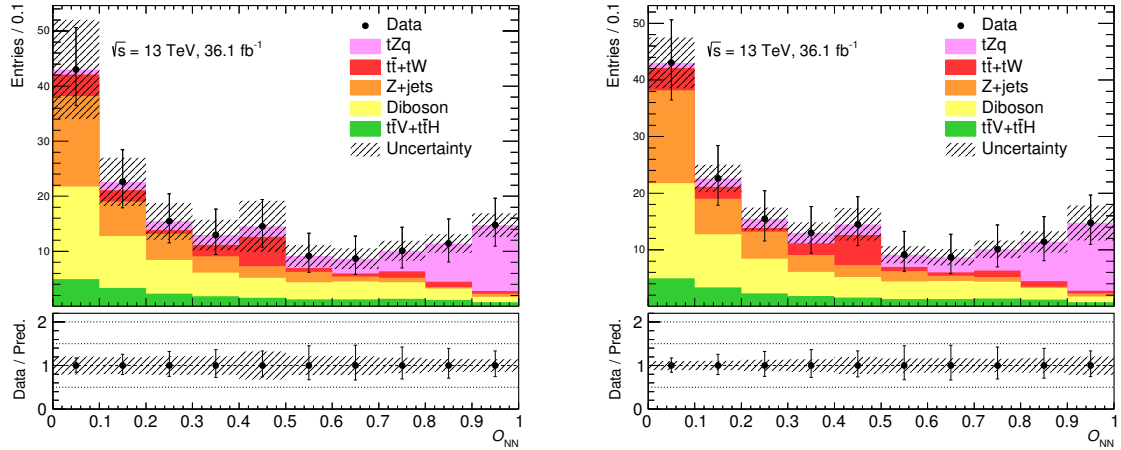
Figure 7.1: Pre-fit (left) and post-fit (right) neural-network output distributions in the signal region. The black points show the Asimov dataset. The error band includes the statistical and systematic uncertainties.

Systematic uncertainties

As already discussed in section 6.3, each systematic uncertainty has an associated nuisance parameter in the fit. All the parameters have a known pre-fit central value, θ_0, that is set to 0, and an uncertainty, $\Delta\theta$. After the fit is performed, two different quantities can be defined in order to understand what the fit learns about each of the systematic uncertainties from the data. One of these quantities is the *pull* of a NP. This is calculated as the deviation of the fitted parameter, $\hat{\theta}$, from its pre-fit central value, normalised by its nominal uncertainty, $(\hat{\theta} - \theta_0)/\Delta\theta$. When the central value is not modified by the fit (which is the case for an Asimov fit), the post-fit and pre-fit values are identical resulting in a pull value of 0. Additionally, the *constraint* of a certain parameter is checked. This can happen if the physics measurement can measure the systematic uncertainty better than the initial prescription. A large NP constraint can be an indication that the uncertainty is overestimated. For investigating whether a parameter is constrained by the fit, the post-fit uncertainties of the NP are checked relative to their pre-fit uncertainties. If this is smaller than 1, the uncertainty is constrained by the fit.

Another result of the fit is determining what the pre-fit and post-fit impact of each systematic uncertainty is on the signal strength. In order to do that, the fit is re-run for each of the NPs (while the other NPs are left free in the fit), fixing the central value of the parameter θ to its post-fit (pre-fit) value $\hat{\theta}$ modified by the upwards and downwards post-fit (pre-fit) uncertainties. The impact of that NP is then calculated as the difference between the μ_{SIG} obtained with the nominal NPs and the one calculated using $\hat{\theta}$.

For summarising the information that is extracted by fitting the data, all the characteristics discussed above are depicted in a single plot, shown in figure 7.2. The top axis is used to check the pull (black filled dots) and constraint (black line). An unconstrained parameter with no pull is shown with a dot centred at 0 and a width of ±1. The bottom axis is related to the pre-fit (in yellow) and post-fit (hatched blue box) impact of the uncertainties on μ_{SIG} that are shown with respect to the total error on the signal strength.

On the y-axis, the systematic uncertainties are sorted according to their pre-fit impact on μ_{SIG}. Only the largest ten systematic uncertainties are shown in the plot. A table containing the full list of systematic uncertainties and their impact on the number of signal events is included in appendix B.

The largest impact on the fit result comes from the uncertainty due to the signal scale and radiation.

This is expected to have a large effect because of the use of a LO MC signal sample. Given the fact that the event selection for the signal region requires exactly two jets, varying the amount of initial and final state radiation can lead to significant changes in the number of selected events, as well as a different shape of the final discriminant. This is observed when comparing the nominal signal O_{NN} distribution with the up and down variations, as shown in figure 6.7.
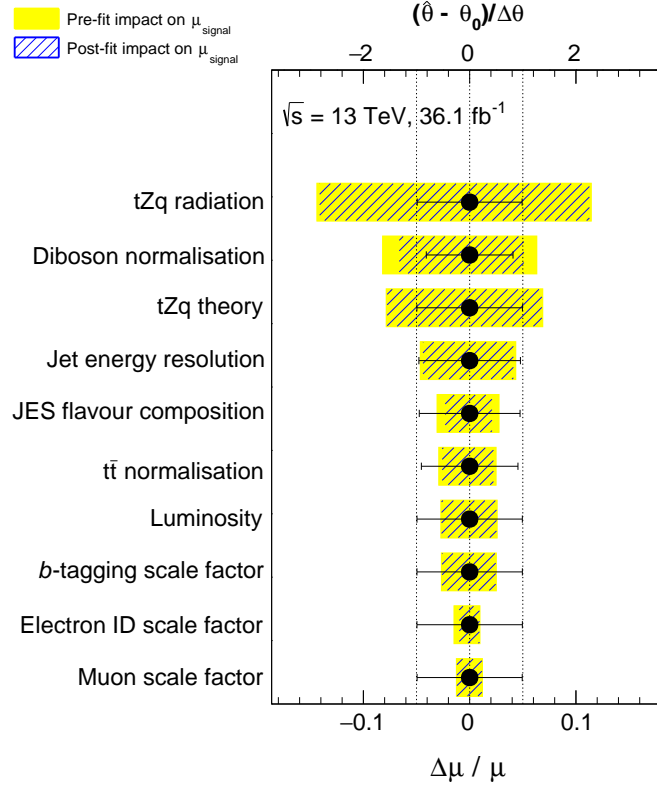
Figure 7.2: The pulls of the fitted NPs (black circles) along with their post-fit uncertainties (black lines), as obtained from the fit to the Asimov dataset, can be read on the top x-axis. The expected pre-fit (in yellow) and post-fit (as hatched blue boxes) impact of the systematic uncertainties on the signal-strength parameter μ_{SIG} is also shown can be read on the bottom x-axis. On the y-axis, the uncertainties are ranked according to their pre-fit impact on μ_{SIG}; only the largest ten uncertainties are included in the plot.

Overall, this uncertainty is expected to have an effect of more than 10% on the signal strength and is not constrained by the Asimov fit. The NP with the second largest impact is the diboson normalisation uncertainty. Pre-fit, the diboson rate had a 40 % uncertainty. The fit constrains this uncertainty to ±0.82 of its nominal value and the impact on the signal strength after the fit is 6 %.

tZq theory is an uncertainty accounting for the scale choice in the predicted signal cross-section calculation. This is introduced as a 7.4 % normalisation error on the *tZq* template and is taken into account when measuring the signal strength with respect to the predicted cross-section. When extracting the cross-section measurement however, this uncertainty is not included since the theoretical prediction uncertainty should not have an effect on the measured cross-section.

Since several variables flagged by the NN as having the best separation power are properties of the selected jets, it is expected that uncertainties related to the jet energy scale and resolution can have an impact on the shape of the NN discriminant and thus on the fit result. The JER has a 5 % post-fit

impact. The effect of the JES component related to the flavour composition is slightly lower. The fit constrains this uncertainty. An overestimation of it could be caused by the assumption that is made when calculating its pre-fit uncertainty. In this, the fraction of quark and gluon jets is assumed to be 0.5 ± 0.5. This could be improved by deriving the quark-gluon profile individually for each process in the selected region of phase space and reducing the assigned uncertainty. However, the effect of this NP on the final result is already very small, suggesting that with the current data sample no significant gain would be achieved by this approach.

For the $t\bar{t}$ background normalisation, a pre-fit uncertainty of 40 % is assigned for the $t\bar{t}$ template. This is slightly constrained by the fit and has an impact on μ_{SIG} of less than 4 %. This is also the case for the luminosity, that is set as a constant 2.1 % uncertainty for all signal and background predictions.

The last three uncertainties in the plot are related to the scale factors for b-tagging efficiency and electron and muon identification. All three NPs are unconstrained and have a very low impact on the signal strength.

Templates comparing the nominal and the up and down systematic variations of all the uncertainties discussed above, for the signal and background processes are included in appendix B.

Expected significance

The expected significance quantifies the compatibility of the background-only hypothesis with the observation (that in this case is set to be the SM signal plus background prediction). The significance obtained from the likelihood fit yields 5.2σ. This means that, if the observed data would perfectly match the predictions, it would be possible to discover tZq production with the current analysis.

7.2 Observed fit results

In order to extract μ_{SIG} and measure the tZq cross-section, a binned profile likelihood fit using the observed data events is performed on the NN output distribution. The pre-fit number of events, as well as the NN discriminant is shown in figure 7.3. 141 events are observed. This is compatible with the total estimated number of signal and background events, 163 ± 12. The bin by bin ratio between data and prediction is shown in the bottom panel of the NN output distribution. All bins show reasonable agreement indicating no background mismodelling.

Systematic uncertainties

The effect of the systematic uncertainties on the fit results are presented similarly to the Asimov results. The pulls and impacts of the uncertainties on μ_{SIG} are shown in figure 7.4. Again no significant pull of the NPs is observed. The diboson normalisation uncertainty is constrained in the fit. The NPs are ranked based on their pre-fit impact and the order is almost identical to the one obtained from the Asimov fit. In general, most of the systematic uncertainty comes from the background rates and signal radiation and scale uncertainty. Out of the uncertainties associated to the reconstruction of physics objects, only the jet related ones have a significant impact. The uncertainty due to the $E_{\mathrm{T}}^{\mathrm{miss}}$ soft term resolution is included in the plot, while the electron ID scale factor uncertainty, that appeared in the ranking plot of the Asimov fit, is dropped. These two NPs have very small and similar impact on μ_{SIG} and, since the number of NPs that are included in the plot is fixed to ten for better readability, small changes can occur in the order of the lower ranked uncertainties.

Additionally, the γ parameters associated to the bin by bin statistical uncertainty of the MC samples are checked and the result is shown in figure 7.5. The impact on μ_{SIG} is very low, with the largest effects
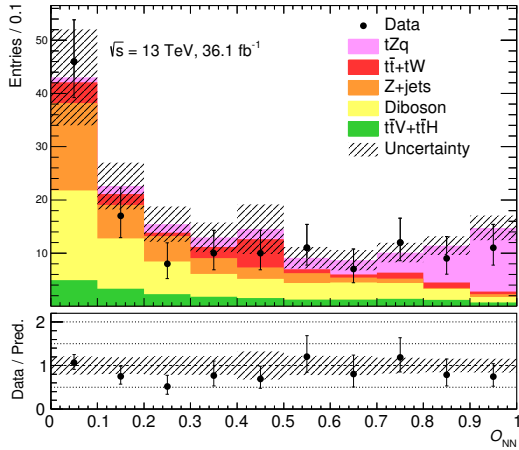
Channel	N_{events}
tZq	35 ± 9
$t\bar{t} + tW$	18 ± 7
$Z + \text{jets}$	37 ± 11
Diboson	53 ± 13
$t\bar{t}V + t\bar{t}H + tWZ$	20 ± 3
Total	163 ± 12
Data	141

Figure 7.3: Pre-fit NN output distribution (left) and event yields (right) in the SR. The quoted errors include the pre-fit statistical and systematic uncertainties.

coming from the signal dominated bins. The uncertainties in some of the bins, for example the 5th bin in the distribution (labelled "Bin 4" on the plot), are large. This can be traced to the larger fraction of events coming from the $t\bar{t}$ background. This sample has very low statistics (45 unweighted events total) and thus will yield a large statistical uncertainty.

Figure 7.6 shows the correlation matrix of all parameters included in the likelihood fit. Only uncertainties that have at least one correlation above 10 % are included. As it is shown in the plot, the diboson and $Z + \text{jets}$ normalisation uncertainties show the largest correlation among all NPs. These have a negative correlation of -0.54. This is understood because the two backgrounds combined account for over 70 % of the total number of background events and the two templates also have very similar shapes for the NN output distribution. Hence, if the fit would enhance one of them, the number of events from the other background would have to go down. Another NP pair that has a correlation higher than ± 0.3 is the $t\bar{t}$ normalisation and the MC statistics γ parameter in the fifth bin of the O_{NN} distribution (labelled as "MC stat O_{NN} (bin 4)" in the plot). As mentioned before, the sample driving the MC statistical uncertainty is the $t\bar{t}$ sample and the largest fraction of $t\bar{t}$ events is found in this particular bin. Hence, an anti-correlation between the $t\bar{t}$ normalisation and the MC stat. uncertainty in that bin is expected.

The tZq radiation uncertainty and μ_{SIG} also have a large correlation of -0.41. Since changing the signal scale and radiation directly modifies the number of selected tZq events, it is expected that this NP will have minor correlations to all other NPs but will have a strong effect on the signal strength parameter.

Another NP that is correlated with the signal strength is the diboson normalisation. These show a correlation of -0.23. Events coming from diboson production represent the dominating background in the signal region. Additionally, it is also the background with the largest number of events in each of the signal dominated bins of the NN discriminant. This means that in order to better fit the data, if the number of signal events is increased, the diboson contribution must be reduced, hence explaining the anti-correlation.

A summary of the effect of each systematic uncertainty on the number of fitted tZq events is given in table 7.1. All uncertainties related to a single physics object are added together (e.g. "Jets" includes all JES related NPs and the JER uncertainty). Even with this merging of some uncertainties, the tZq radiation is dominant, changing the number of signal events by up to 10 %.
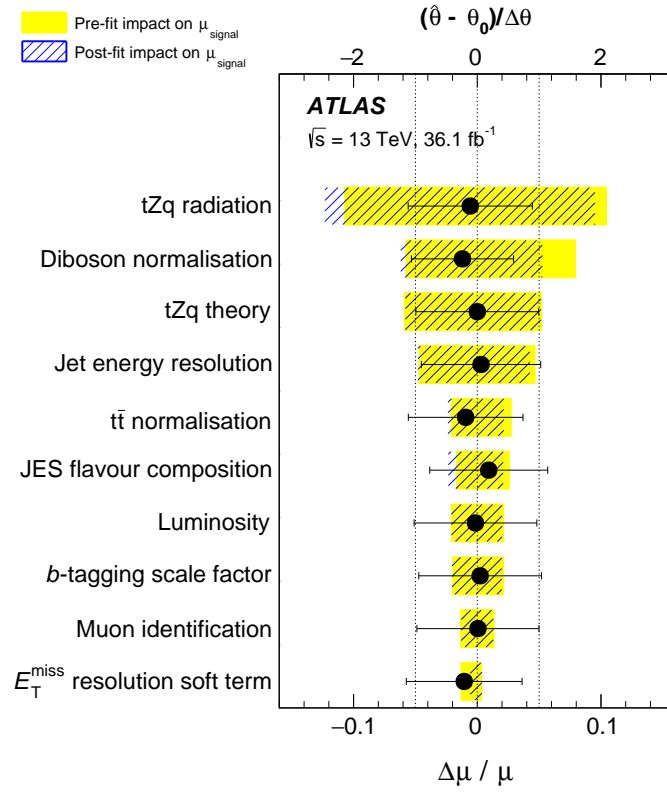
Figure 7.4: The pulls of the fitted NPs (black circles) along with their post-fit uncertainties (black lines), as obtained from the data fit, can be read on the top *x*-axis. The expected pre-fit (in yellow) and post-fit (as hatched blue boxes) impact of the systematic uncertainties on the signal-strength parameter μ_{SIG} is also shown can be read on the bottom *x*-axis. On the *y*-axis, the uncertainties are ranked according to their pre-fit impact on μ_{SIG}; only the largest ten uncertainties are included in the plot.

Source	Uncertainty [%]
tZq radiation	±10.8
Jets	±4.6
b-tagging	±2.9
MC statistics	±2.8
tZq PDF	±2.2
Luminosity	±2.1
Leptons	±2.1
$E_{\text{T}}^{\text{miss}}$	±0.3

Table 7.1: Breakdown of the impact of the systematic uncertainties on the number of *tZq* signal events in order of decreasing effect.
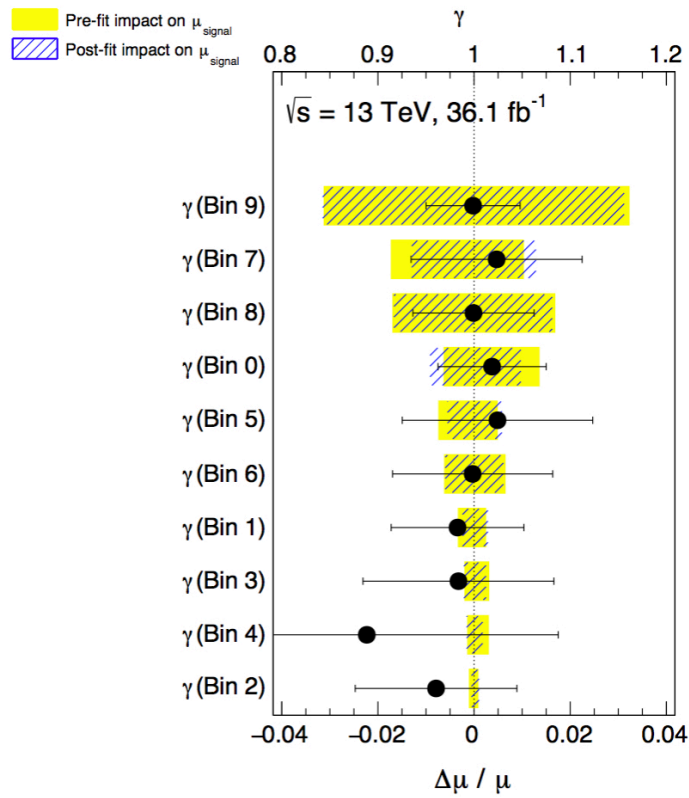
Figure 7.5: Ranked impact plots with pulls for the Monte Carlo simulation statistics NPs in each bin of the final discriminant when performing a fit to data. The expected pre-fit (in yellow) and post-fit (as hatched blue boxes) impact of the systematic uncertainties on the signal-strength parameter μ_{SIG} is shown can be read on the bottom x-axis. The pulls of the fitted NPs (black circles) along with their post-fit uncertainties (black lines) can be read on the top x-axis. On the y-axis, the uncertainties are ranked according to their pre-fit impact on μ_{SIG}.
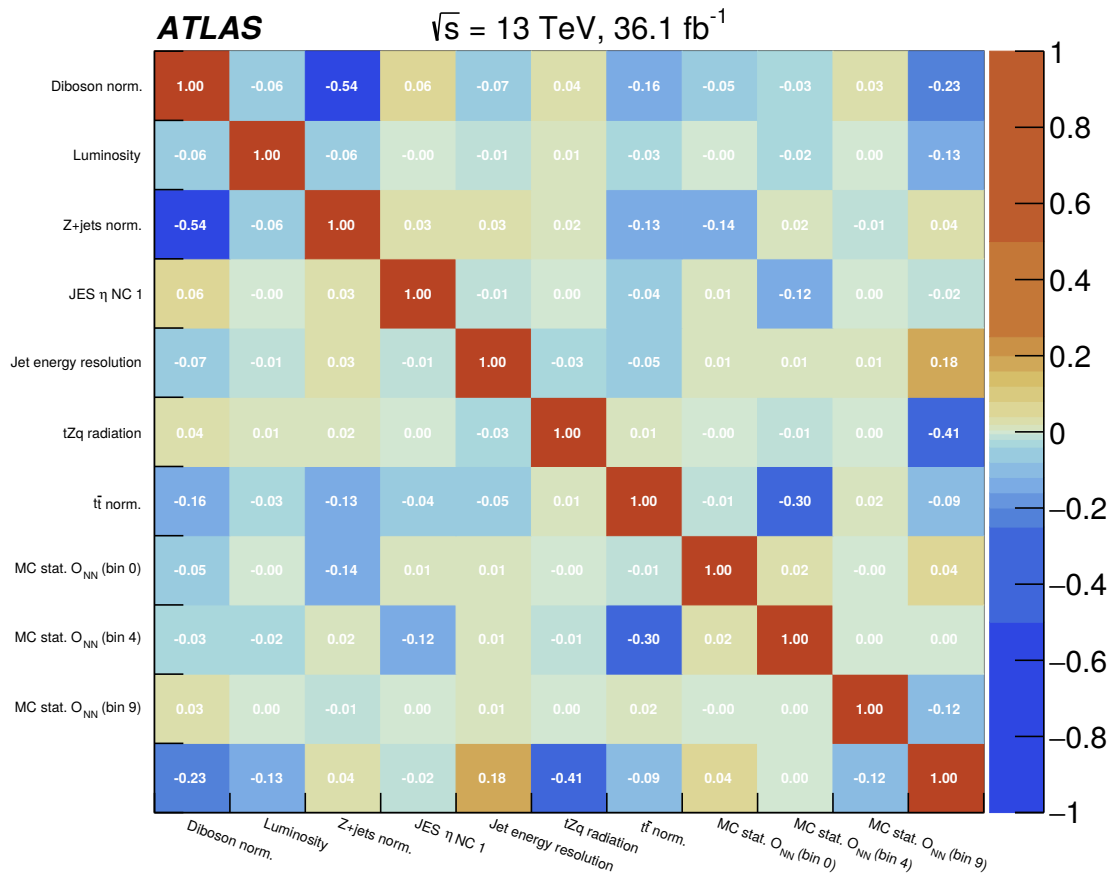
Figure 7.6: Correlation matrix of the parameters included in the likelihood fit for the data. Only those uncertainties that are correlated by more than 10 % with another uncertainty are included.

Cross-section measurement and observed significance

When performing the fit, the signal strength is the only unconstrained parameter, while the normalisation of the background processes is allowed to change within their assigned uncertainty. Figure 7.7 shows the post-fit NN output distribution (left), as well as the corresponding event yields (right). As expected, better agreement is observed between data and post-fit signal and background events. For all processes, the fitted yields are close to their initial prediction. The ratio between the observed and predicted events for each process is given in the second column of the table. All ratios are compatible with 1.

For the signal, the fitted number of events is 25.8 ± 8.3, resulting in a measured signal strength:

$$\mu_{\mathrm{SIG}} = 0.75 \pm 0.21(\mathrm{stat.}) \pm 0.17(\mathrm{syst.}) \pm 0.05(\mathrm{theo.}).$$

The quoted theoretical error is related to the *tZq* predicted cross-section scale uncertainty. Using the extracted μ_{SIG}, the cross section for *tZq* production is calculated to be:

$$\sigma^{tZq} = 600 \pm 170 \;(\mathrm{stat.}) \pm 140 \;(\mathrm{syst.}).$$

The statistical uncertainty is determined by performing the fit without any systematic uncertainties. The total systematic uncertainty is obtained by subtracting in quadrature the statistical part from the total error.

From the fit, the probability of observing the data given the background only hypothesis is $p_0 = 1.3 \times 10^{-5}$. This corresponds to an observed significance of 4.2σ.
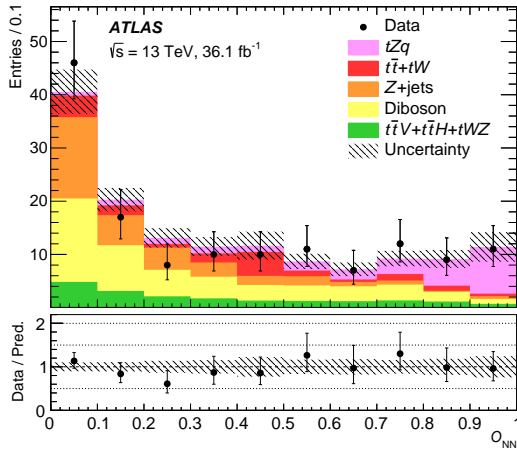
Channel	$N_{\mathrm{obs.}}$	$N_{\mathrm{obs.}}/N_{\mathrm{pred.}}$
tZq	25.8 ± 8.3	0.7 ± 0.3
$t\bar{t} + tW$	16.9 ± 6.8	0.9 ± 0.6
$Z + \mathrm{jets}$	33.5 ± 10.9	0.9 ± 0.5
Diboson	47.7 ± 12.5	0.9 ± 0.4
$t\bar{t}V + t\bar{t}H + tWZ$	18.9 ± 3.1	1.0 ± 0.2
Total	142.8 ± 10.7	-
Data	141	-

Figure 7.7: Post-fit NN output distribution (left) and event yields (right) in the SR. The errors include the post-fit statistical and systematic uncertainties.

7.3 Discussion of the results

There are several reasons motivating the study of the associated production of a top quark and a *Z* boson. Because of its very low cross-section, this process had not been previously investigated by ATLAS and CMS searches at $\sqrt{s} = 8\,\mathrm{TeV}$ did not yield significant results, thus no evidence of *tZq* production was established before this analysis.

The observed statistical significance of the result is 4.2σ, corresponding to a strong evidence of the

existence of this process. The value is slightly lower than the expected significance of 5.4σ. This comes from the downward fluctuation of the data in the signal dominated region of the NN discriminant (particularly the last two bins) compared to the signal and background predictions.

Two important couplings are probed when measuring this process, namely the top-quark coupling to the Z and the triple gauge boson (WWZ) coupling. New Physics effects that modify these constants would thus affect the value of the tZq cross-section. The measured value of μ_{SIG} is 0.75 ± 0.28(stat. + sys.) ± 0.05(theo.). Within the uncertainties, this is in good agreement with the theoretical predictions (corresponding to $\mu_{SIG} = 1$), thus further confirming the validity of the SM.

In searches for other rare processes involving top-quarks or searches for non-SM top-quark decays, the tZq process, that constitutes an irreducible background, was not taken into account until the start of Run 2. An example of such analysis is the search for FCNC decays of the top quark in $t\bar{t}$ events. In the SM the branching ratio for the FCNC decay $t \rightarrow Zq$ is less than 10^{-12} but several New Physics scenarios could lead to an enhanced value. A $t\bar{t}$ event in which one the two top quarks has a non-SM decay, resulting in a Z boson and a quark, would lead to a final state identical to tZq production. A reliable estimation of the background, with a reasonable associated uncertainty, is needed in order to set competitive limits on the relevant coupling. Establishing and measuring the tZq process is therefore an important step both in itself, and in the context of other top-quark related analyses.

Although the result of this measurement is statistically dominated, this is expected to change in the near future, once the 2017 data is analysed. Already in this analysis, the size of the total systematic uncertainty is only slightly smaller than the statistical one. A reduction of the systematic uncertainties is necessary in order to improve the precision of the cross-section measurement.

The dominant component, the scale and radiation signal systematics, is expected to significantly decrease when using a NLO signal sample. Another large contribution to the total uncertainty comes from background estimation and normalisation. For diboson, this could be better controlled by changing to a NLO sample, thus improving the modelling and decreasing the assigned normalisation uncertainty. The Z + jets contribution is evaluated using a data-driven technique. No straight-forward solution for getting a more precise estimation is known but other non-prompt lepton background estimation techniques can be investigated. In the case of $t\bar{t}$, a large improvement could be achieved just by increasing the statistics of the MC sample. This would lead to a more precise estimation of the data/MC SF used for correcting the $t\bar{t}$ normalisation and at the same time, would reduce the uncertainty due to low MC statistics.

Uncertainties due to the reconstruction and calibration of physics objects do not have a very large impact on the result. The most significant ones are related to the measurement of jets. These can potentially be further reduced by optimising the event selection criteria that are applied on the forward and b-tagged jets. Additionally, ATLAS recommendations for the jet uncertainties are constantly improving and changes such as reducing the flavour composition uncertainty, that was mentioned in section 7.1, could add up to a sizeable effect.

Comparison with the $tllq$ cross-section measurement performed with the CMS experiment

A measurement of the associated production of a single top-quark and a Z boson using $35.9 \, \text{fb}^{-1}$ of data collected in 2016 was also performed by the CMS collaboration [43]. This reports a measured cross-section for $tZq \rightarrow Wb\ell^+\ell^- q$ of 123^{+33}_{-31}(stat.)$^{+29}_{-23}$(syst.) fb, with the observed (expected) significance of 3.7 (3.1) standard deviations. In order to compare the results, a summary of both the ATLAS and CMS analyses is given in table 7.2.

Broadly speaking, the strategies for the ATLAS and CMS measurements are similar. For separating signal and backgrounds, MVA techniques are used for both analyses, namely a NN for ATLAS and boosted decision trees (including variables computed with the matrix element method) for CMS. Signal

extraction is done using a binned likelihood fit. However, the analyses do differ in certain key points such as signal definition and signal sample generation, event selection and background estimation. In order to understand the differences in results between the two experiments, the most relevant non-common features of the analysis strategy are discussed in more detail below.

	ATLAS (tZq)	CMS ($t\ell^+\ell^- q$)
μ_{SIG}	$0.75 \pm 0.21(\text{stat.}) \pm 0.17(\text{syst.}) \pm 0.05(\text{theo.})$	$1.31^{+0.35}_{-0.33}(\text{stat.})^{+0.31}_{-0.25}(\text{syst.})$
$\sigma^{\mathrm{SM}}_{tZq \backslash t\ell^+\ell^- q}$ (fb)	$800^{+6.1\%}_{-7.4\%}(\text{scale + PDF})$	$94.2^{+1.9}_{-1.8}(\text{scale}) \pm 2.5(\text{PDF.})$
$\sigma_{tZq \backslash t\ell^+\ell^- q}$ (fb)	$600 \pm 170 \,(\text{stat.}) \pm 140 \,(\text{syst.})$	$123^{+33}_{-31}(\text{stat.})^{+29}_{-23}(\text{syst.})$
Obs. (exp.) significance	$4.2 \,(5.4)\, \sigma$	$3.7 \,(3.1)\, \sigma$

Table 7.2: Summary of the final results for the ATLAS tZq cross-measurement and CMS $t\ell^+\ell^- q$ measurement.

The tZq MC sample used for the CMS analysis is generated at NLO, and includes only leptonically decaying Z bosons. An additional diagram including the non-resonant Z boson contribution is also considered as part of the signal in the generation processes. This is shown in figure 7.8. The Z boson can be off-shell but the invariant mass of the $\ell^+\ell^-$ pair is required to be higher than $30\,\text{GeV}$. Additionally, the tZq process is generated in the 5-flavour scheme and the scale is set to $\mu_{\mathrm{r}} = \mu_{\mathrm{f}} = 1/2 \sum \sqrt{E^2 - P_z^2}$. Using this setup, the predicted cross-section calculation yields $\sigma^{\mathrm{SM}}_{t\ell^+\ell^- q} = 94.2^{+1.9}_{-1.8}(\text{scale}) \pm 2.5(\text{PDF.})$ fb.

In order to make a direct comparison of the two results, the different values of the predicted cross-sections must be understood. When the $\sigma^{SM}_{t\ell^+\ell^- q}$ prediction is corrected by the $Z \to \ell^+\ell^-$ branching ratio of $10\,\%$ (including τ leptons), an approximate prediction for the inclusive cross-section: $\sigma^{\mathrm{SM}}_{tZq}(\text{CMS}) = 942^{+19}_{-18}(\text{scale}) \pm 25(\text{PDF.})$ fb is obtained. The ATLAS cross-section calculation yields $800^{+6.1}_{-7.4}\%(\text{scale})$ fb, but it does not include the non-resonant contribution mentioned before, and also uses a different scale choice. Given these differences and taking into account the associated uncertainties, the predictions from both experiments are in reasonable agreement.

Recent investigations show that the effect of including the non-resonant diagrams is only visible in the $m_{\ell\ell} < 70\,\text{GeV}$ range [123]. Because the analysis presented in this thesis requires the invariant mass of the two leptons at reconstruction level to be between 81 and $101\,\text{GeV}$, no bias is introduced in the ATLAS analysis due to the omission of this contribution.
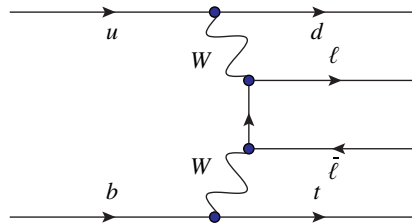
Figure 7.8: Non-resonant tZq LO production.

In terms of selection, the most significant difference comes from the requirement on the number of jets in the event. The CMS analysis selects events with exactly two or three jets. Because a NLO signal sample is used, it is possible to have a significant signal fraction in the higher jet multiplicity bins. One of the selected jets must be identified as b-tagged and it is worth noting that for the chosen b

identification working point, the mistag rate is 10 times higher for CMS compared to ATLAS. The cut on the invariant mass of the two leptons associated with the Z boson applied in the CMS analysis is more permissive, allowing events to pass the selection if the $m_{\ell\ell}$ falls within a ± 15 GeV window around the Z boson mass. This will increase the contamination from $t\bar{t}$ events that have an additional non-prompt lepton, as well as other processes in which no Z boson is produced.

After the selection, in the CMS analysis, the S/B for all jet bins is approximately $10\,\%$[2]. This is two times smaller than the corresponding ratio in the ATLAS analysis.

For CMS, all non-prompt lepton background sources ($t\bar{t}$ and $Z+$ jets) are concurrently estimated using a fully data-driven method. This contribution is not included in the MVA training and hence the MVA output shape of the non-prompt lepton background is roughly flat. This plays a significant role in the signal background separation. The ATLAS measurement and statistical significance of the result is driven by the last bins of the NN discriminant that have a very high S/B ratio.

The measured tZq cross-sections, for both ATLAS and CMS, are in agreement with the respective SM predictions. The calculated uncertainties are also of similar magnitude, with a dominating statistical component. In terms of statistical significance, the ATLAS experiment outperforms the CMS one, with the difference most likely being related to the lower S/B ratio in the CMS signal dominated region of the MVA discriminant. This is influenced by the different selection criteria, as well as the inclusion of the non-prompt lepton background in the NN training for the ATLAS analysis, allowing this background to be better separated from the signal.

---

[2] Based on the post-fit signal and background number of events.

Conclusions

The associated production of a single top-quark and a Z boson is a rare process predicted by the Standard Model. The tZq cross-section is calculated at NLO precision in QCD and is 800 fb, with a $^{+6.1}_{-7.4}\%$ uncertainty obtained by changing the renormalisation and factorisation scales. This thesis presents the first search for tZq production performed using pp collision data recorded by the ATLAS detector. In total, 36.1 fb^{-1} of data collected in 2015 and 2016 at a centre-of-mass energy of 13 TeV were used.

This process occurs through the radiation of the Z boson from any of the quarks in a t-channel single top-quark production diagram. Additionally, production via the WWZ vertex is also possible. Studying tZq production thus indirectly probes both the top-Z and the tri-boson coupling involved. Any deviation from the SM predicted cross-section could indicate a modification of these couplings through BSM effects.

Based on the decay mode of the Z boson and the top quark, several final states can be identified. The final state selected for this analysis is chosen such that the potential for discovery of tZq SM production is maximised. Events in which both the top-quark and the Z boson decay leptonically are selected. The resulting final state includes three isolated leptons, two jets, one of which has to be b-tagged, as well as missing transverse momentum.

The main challenge for this analysis is handling the events coming from other physics processes with much larger cross-sections. The first step towards that is accurately estimating these backgrounds. For processes in which three prompt leptons are produced, MC predictions are used. However, processes with a dileptonic final state, such as $t\bar{t}$ and Z + jets, with an additional non-prompt lepton, must be estimated using data-driven techniques. Once all these contributions are evaluated and validated, background events still are predicted to exceed the number of signal events in the selected phase space region. Out of a total of 163 events predicted, 35 are expected from tZq production. The number of signal events is estimated using a LO Monte Carlo sample, that is scaled to the NLO predicted cross-section.

Since none of the kinematic properties of the final state objects offers enough separation between signal and background, a multivariate classification algorithm is used. This artificial neural network combines information from several variables in order to construct a discriminant with increased separation power. The most significant variables in the neural network training are related to the untagged jet. This is a typical signature for t-channel single top-quark events, since it is predominantly present in the forward region and has a harder p_T spectrum compared to jets coming from top-quark decays.

In order to measure the tZq cross-section, a statistical analysis is done by performing a binned likelihood fit on the neural network discriminant, using 141 recorded data events. Systematic uncertainties

are included in the fit via dedicated nuisance parameters. After the fit, 26 *tZq* events are observed. This corresponds to a measured *tZq* cross-section:

$$\sigma_{tZq} = 600 \pm 170 \text{ stat.} \pm 140 \text{ syst. fb.}$$

This result has an observed (expected) significance of 4.2σ ($5.4\ \sigma$). The measurement is in agreement with the SM expectation within the calculated uncertainties.

The uncertainty on this measurement is dominated by the statistical component. With more data being collected at ATLAS and a better understanding of all ingredients involved in the *tZq* analysis, in particular background estimation techniques and systematic uncertainties, it should be possible in the very near future to surpass the 5σ statistical significance threshold and thus discover the *tZq* process. Furthermore, a significant improvement is expected from using a signal simulated sample produced at NLO. This would reduce the scale and radiation uncertainties on the signal, that are the dominating source of systematic errors in the current analysis.

The result presented in this thesis constitutes the first strong evidence for the associated production of a single top-quark and a *Z* boson. This was obtained by devising a successful analysis strategy that can also serve as a starting point for for more precise *tZq* measurements and other new searches for rare processes involving top quarks, such as *tH* associated production.

Additional Figures

A.0.1 Contol plots for basic kinematic variables in the SR
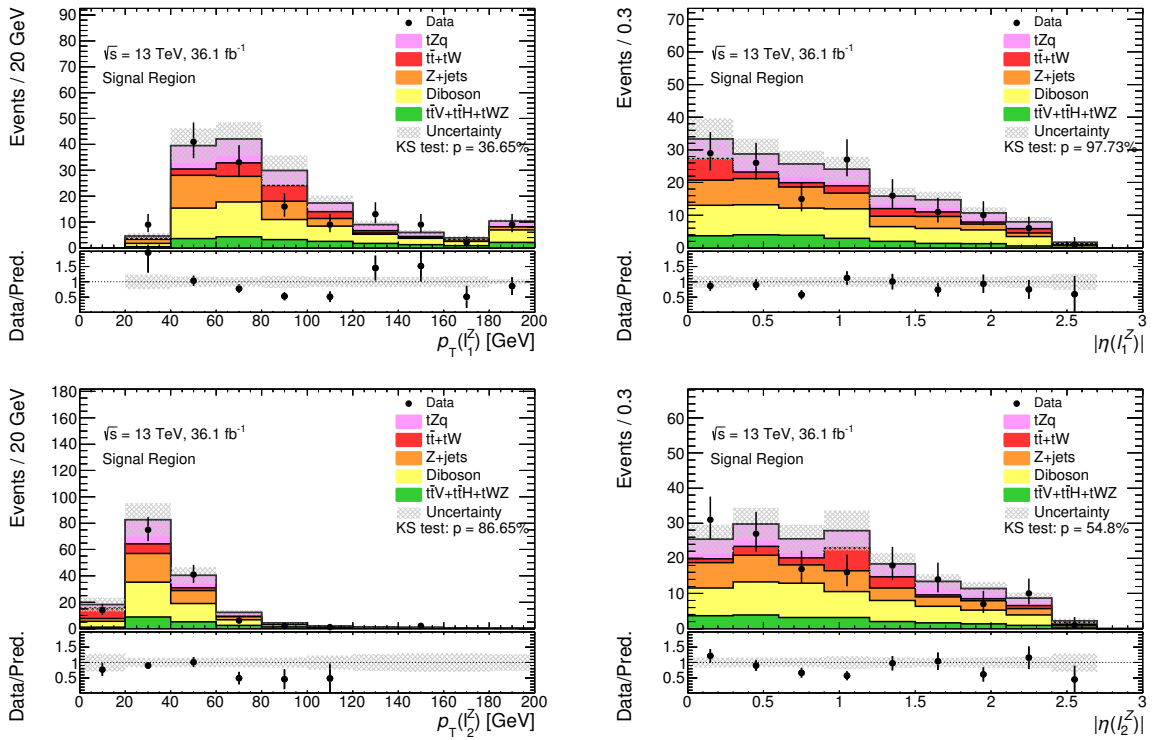
Figure A.1: Control plots for reconstructed lepton-related quantities in the SR. Signal and backgrounds are normalised to the expected number of events before the fit and additional scale factors are applied for diboson and $t\bar{t}$. The Z + jets background is estimated using a data-driven technique. The uncertainty band includes the statistical uncertainty and the uncertainties on the backgrounds derived in section 5.5.
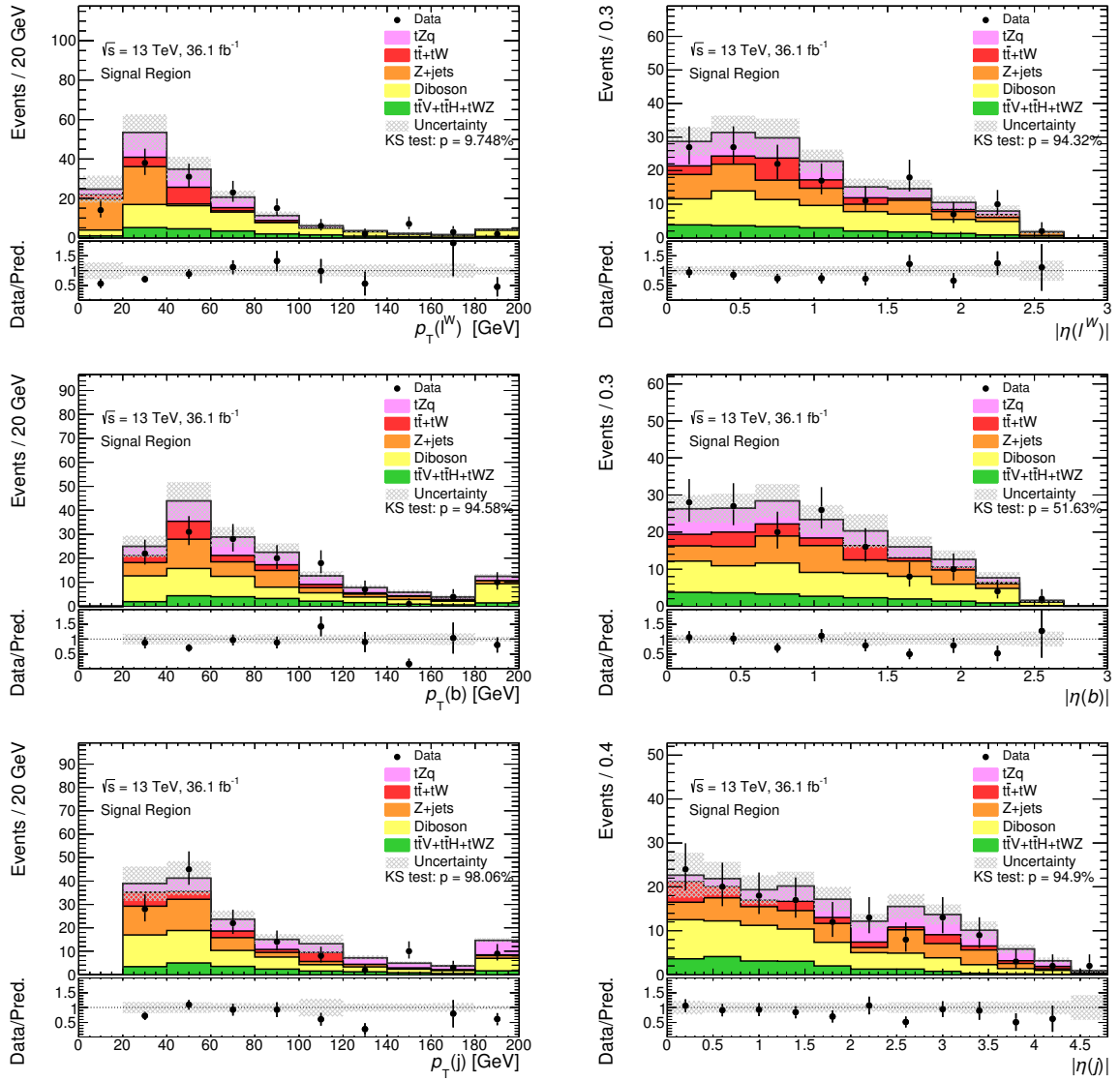
Figure A.2: Control plots for reconstructed lepton and jet-related quantities for events in the signal region. Signal and backgrounds are normalised to the expected number of events before the fit and additional scale factors are applied for diboson and $t\bar{t}$. The Z + jets background is estimated using a data-driven technique. The uncertainty band includes the statistical uncertainty and the uncertainties on the backgrounds derived in section 5.5.
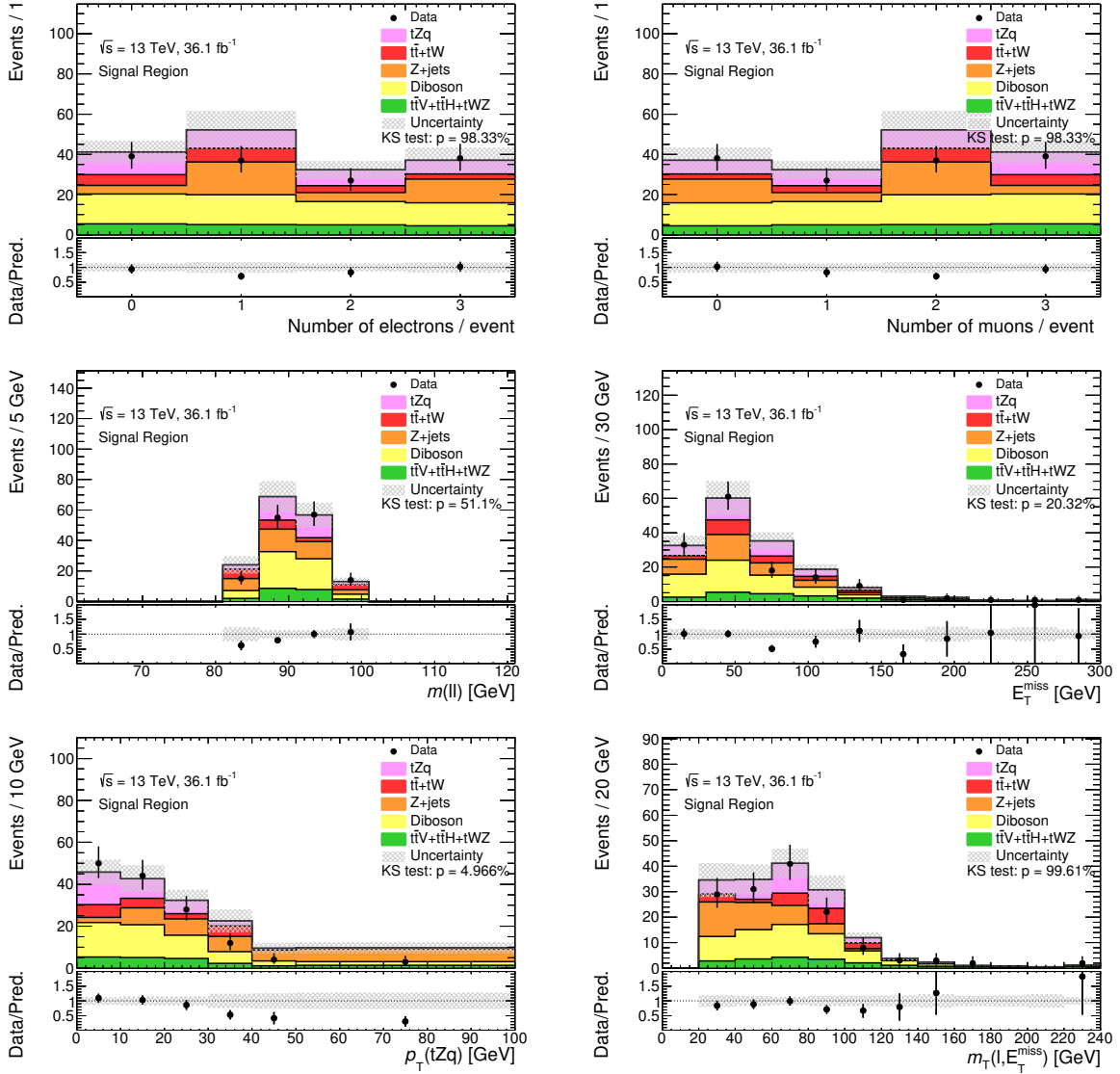
Figure A.3: Control plots for different quantities for events in the signal region. Signal and backgrounds are normalised to the expected number of events before the fit and additional scale factors are applied for diboson and $t\bar{t}$. The Z+jets background is estimated using a data-driven technique. The uncertainty band includes the statistical uncertainty and the uncertainties on the backgrounds derived in section 5.5.
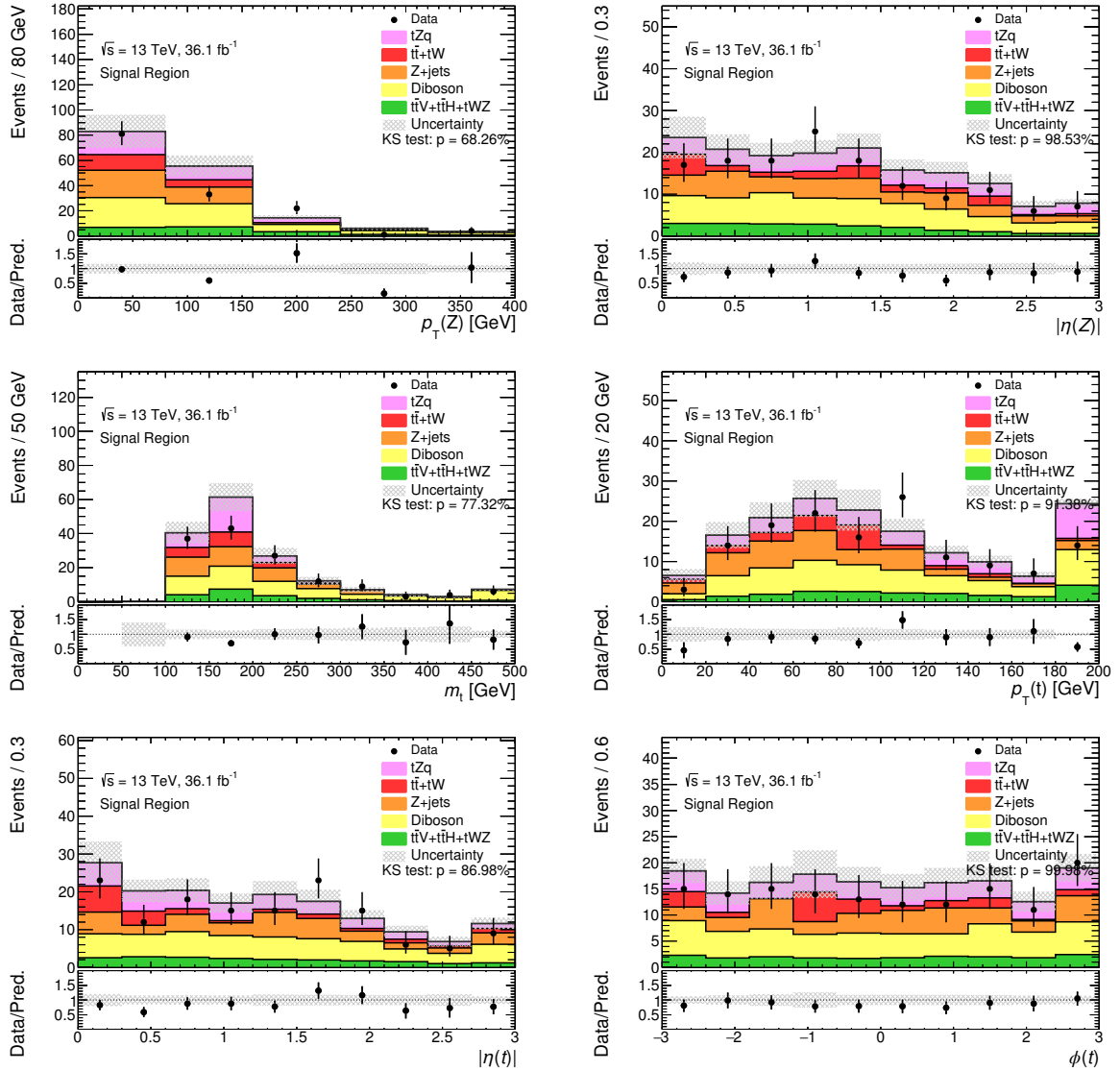
Figure A.4: Control plots for reconstructed top and *Z* related quantities for events in the signal region. Signal and backgrounds are normalised to the expected number of events before the fit and additional scale factors are applied for diboson and $t\bar{t}$. The *Z* + jets background is estimated using a data-driven technique. The uncertainty band includes the statistical uncertainty and the uncertainties on the backgrounds derived in section 5.5.

A.0.2 Control plots in the background dominated region

The set of variables shown in figure A.5 and **??** is the one that is used for the NN training. Starting with the signal region selection, the NN is applied on both data and MC but only events that have a NN score lower than 0.5 are shown. A good overall agreement between data and MC is observed.
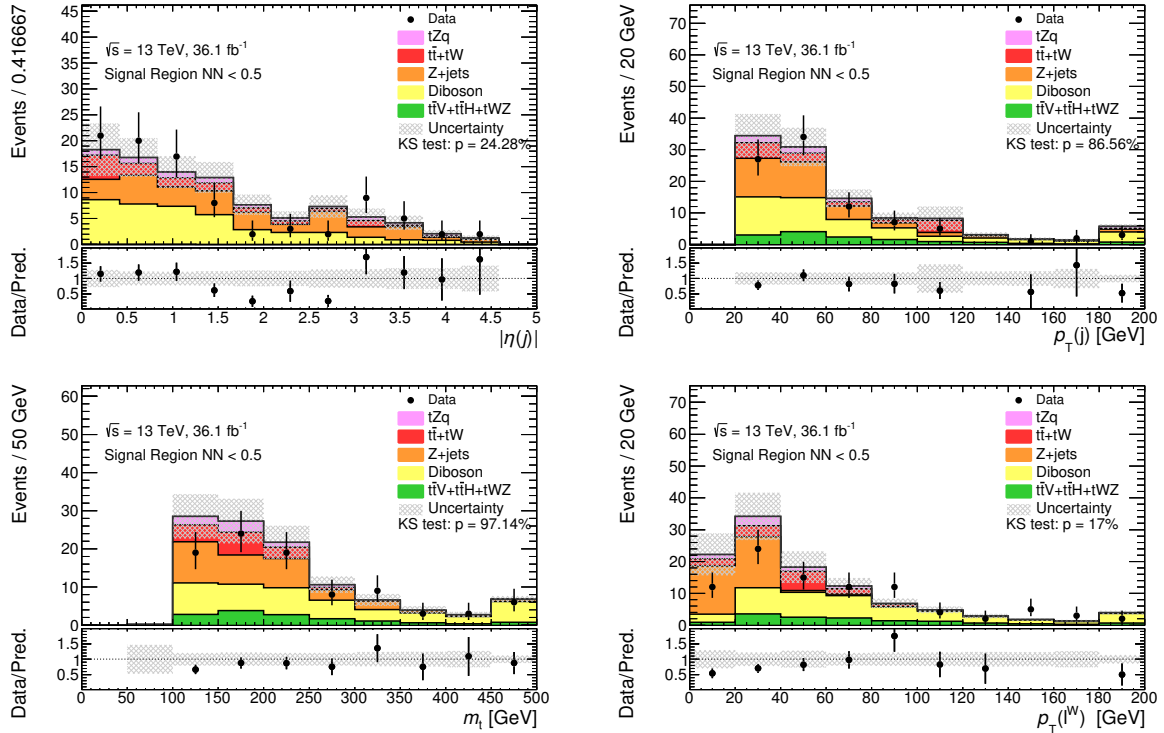
Figure A.5: Stacked kinematic plots of the most discriminating variables in the SR for background-like events (NN output < 0.5). Signal and backgrounds are normalised to the expected number of events before the fit and additional scale factors are applied for diboson and $t\bar{t}$. The Z + jets background is estimated using a data-driven technique. The uncertainty band includes the statistical uncertainty and the uncertainties on the backgrounds derived in section 5.5.
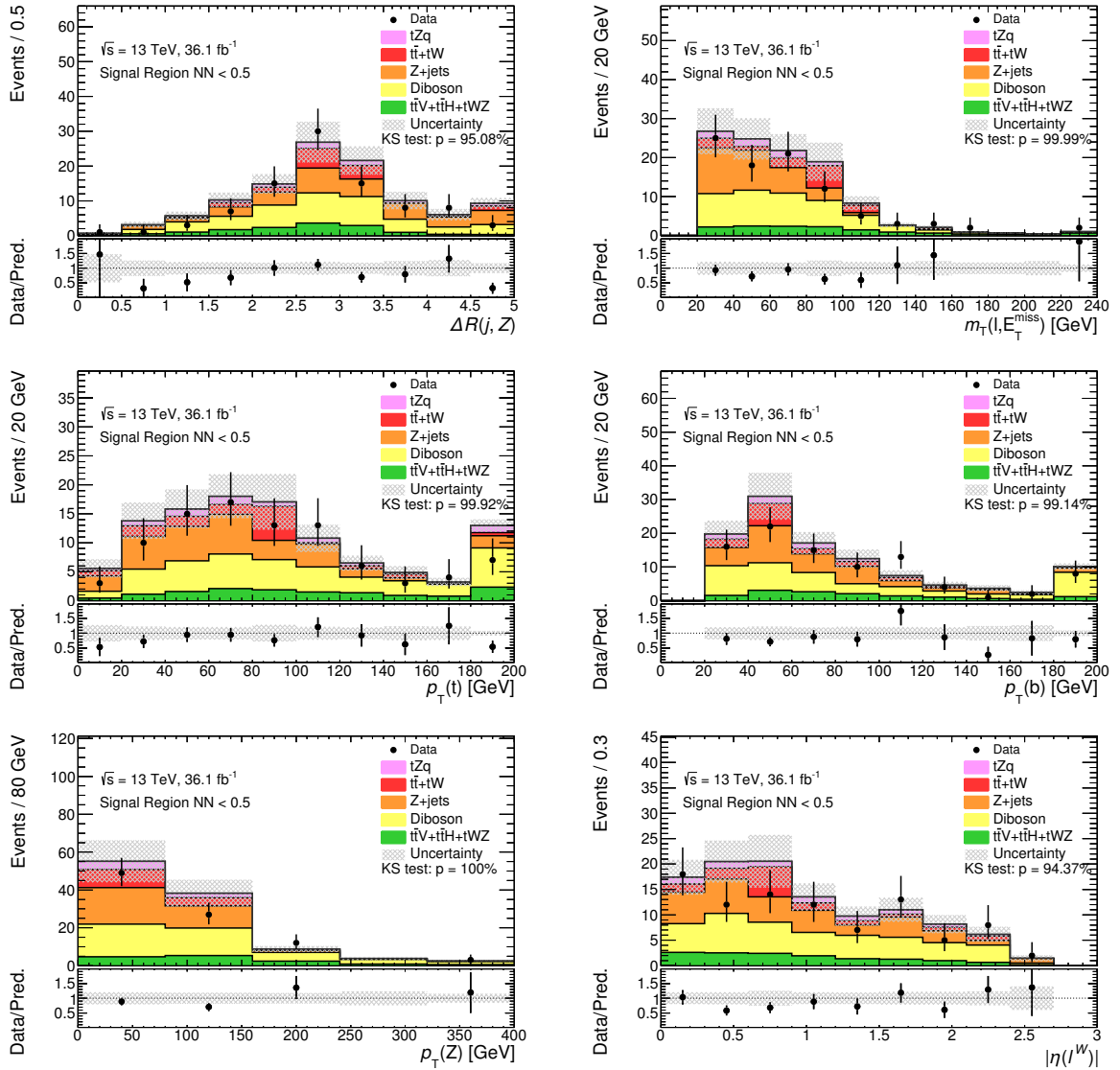
Figure A.6: Stacked kinematic plots of the most discriminating variables in the SR for background-like events (NN output < 0.5). Signal and backgrounds are normalised to the expected number of events before the fit and additional scale factors are applied for diboson and $t\bar{t}$. The Z + jets background is estimated using a data-driven technique. The uncertainty band includes the statistical uncertainty and the uncertainties on the backgrounds derived in section 5.5.

A.0.3 Control plots in the signal dominated region

The set of variables shown in figure A.7 and figure A.8 is the one that are selected for the NN training. Starting for the signal region selection, the NN is applied on both data and MC but only events that have a NN score lower than 0.5 are shown. A good overall agreement between data and MC is observed.
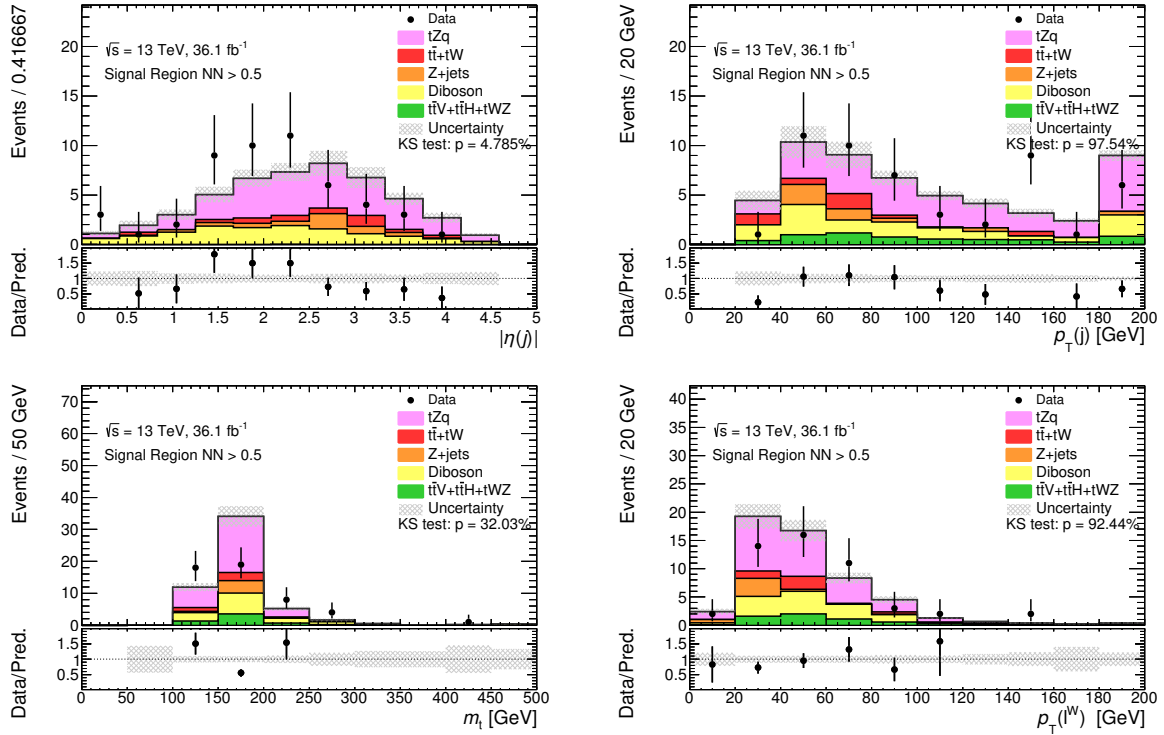
Figure A.7: Control plots for reconstructed lepton-related quantities for events in the signal-enhanced region ($O_{NN} > 0.5$). Signal and backgrounds are normalised to the expected number of events before the fit and additional scale factors are applied for diboson and $t\bar{t}$. The Z + jets background is estimated using a data-driven technique. The uncertainty band includes the statistical uncertainty and the uncertainties on the backgrounds derived in section 5.5.
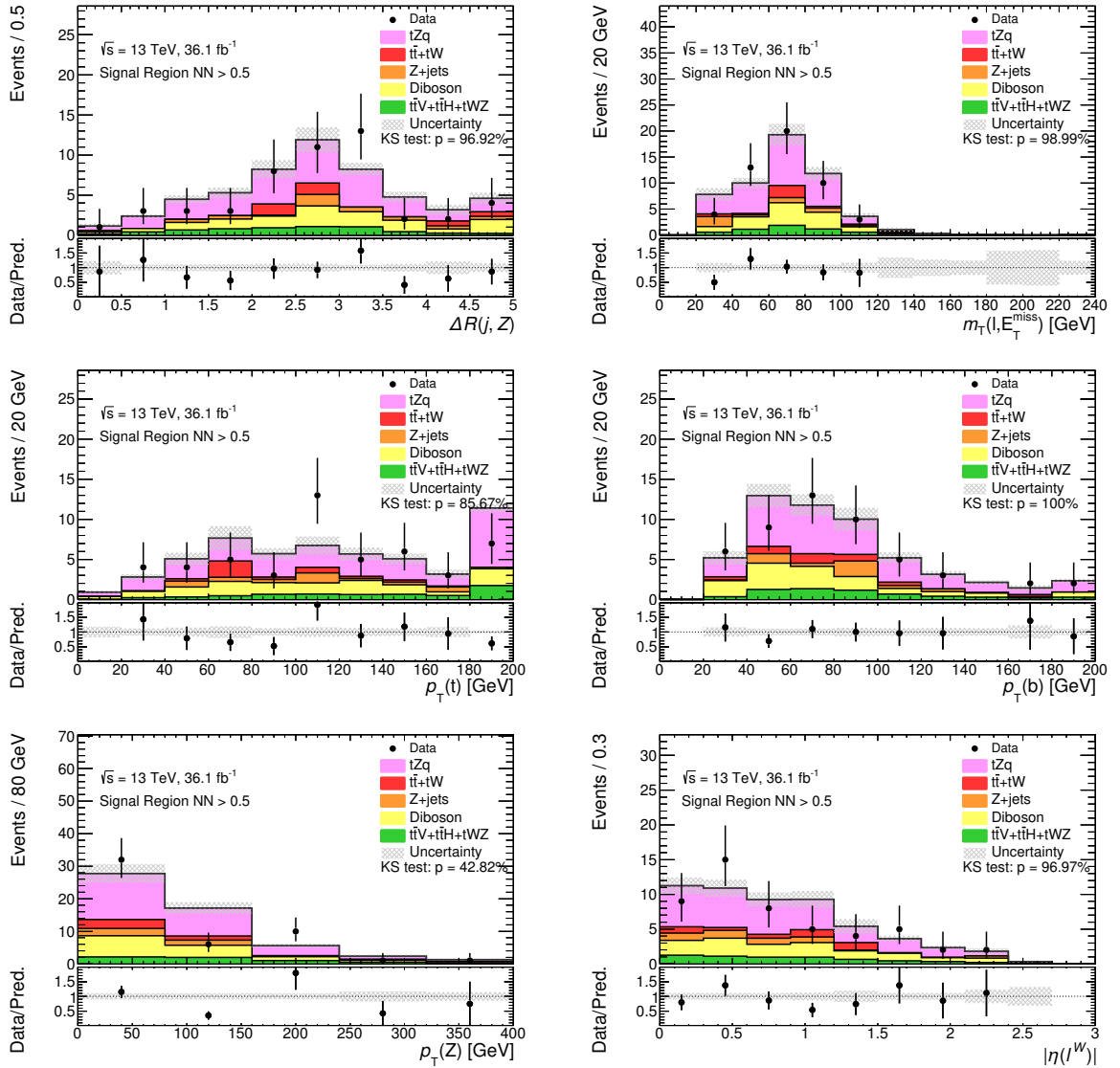
Figure A.8: Stacked kinematic plots of the most discriminating variables in the SR for signal-like events (NN output > 0.5). Signal and backgrounds are normalised to the expected number of events before the fit and additional scale factors are applied for diboson and $t\bar{t}$. The Z + jets background is estimated using a data-driven technique. The uncertainty band includes the statistical uncertainty and the uncertainties on the backgrounds derived in section 5.5.

A.0.4 Control Plots in the diboson VR

The first six variables selected by the NN in the preprocessing stage have been already shown in figure 5.23. Figure A.9 shows the modelling of the remaining four selected variables in the diboson VR.
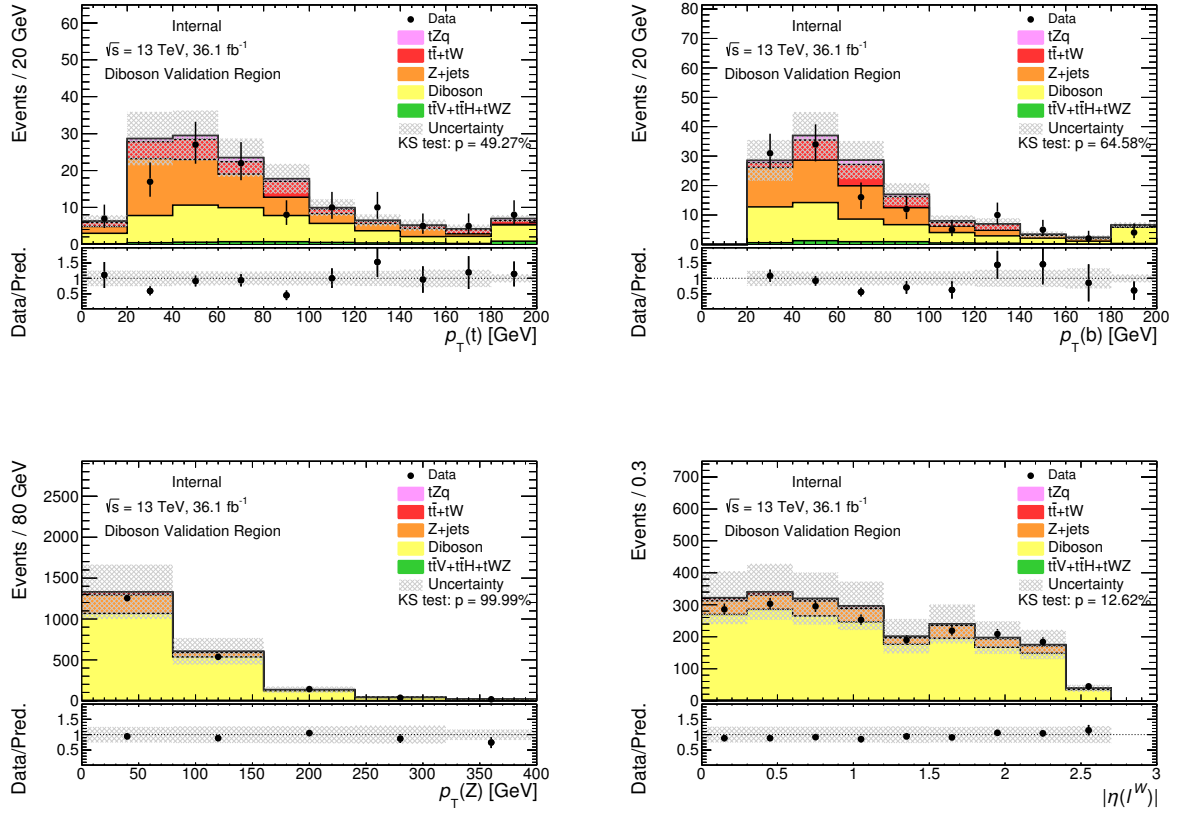
Figure A.9: Comparison of the data and the signal+background model for the last four neural-network training variables in the diboson validation region. The top-quark is reconstructed and variables built from b-tagged and top-quark vectors are calculated only if the available jet is b-tagged (bottom left plot). If the jet is untagged, then the top quark is not reconstructed, and variables built from the b-tagged jet and top-quark vectors are undefined. Signal and backgrounds are normalised to the expected number of events before the fit and additional scale factors are applied for diboson and $t\bar{t}$. The Z + jets background is estimated using a data-driven technique. The uncertainty band includes the statistical uncertainty and the uncertainties on the backgrounds derived in section 5.5. The rightmost bin includes overflow events.

A.0.5 Additional control plots in the $t\bar{t}$ VR

The first six variables selected by the NN in the preprocessing stage have been already shown in figure 5.24. Figure A.10 shows the modelling of the remaining four selected variables in the $t\bar{t}$ VR.
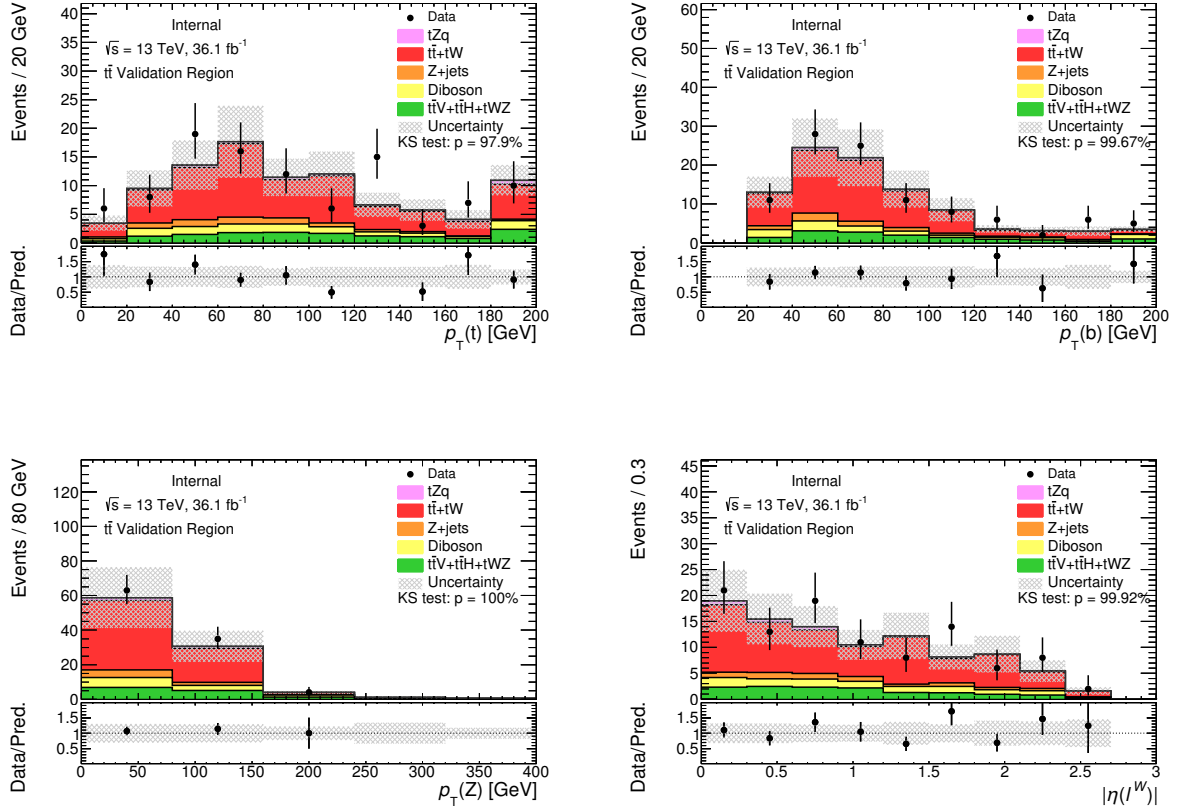
Figure A.10: Comparison of the data and the signal+background model for the last four neural-network training variables in the $t\bar{t}$ validation region. Signal and backgrounds are normalised to the expected number of events before the fit and additional scale factors are applied for diboson and $t\bar{t}$. The Z+jets background is estimated using a data-driven technique. The uncertainty band includes the statistical uncertainty and the uncertainties on the backgrounds derived in section 5.5. The rightmost bin includes overflow events.

A.0.6 Event yields for the $t\bar{t}$ and diboson VR

Table A.1: Number of observed and expected events in the $t\bar{t}$ validation region. The left table shows the number of events after luminosity weighting, while the right table shows the raw number of events available.

Process	Scaled events	Process	Raw events
$t\bar{t}V + t\bar{t}H + tWZ$	13.7 ± 0.3	$t\bar{t}V + t\bar{t}H + tWZ$	7979
Diboson	10.4 ± 3.2	Diboson	571
$Z + \text{jets}$	6.7 ± 2.7	$Z + \text{jets}$	531
$t\bar{t}$	61.2 ± 26.3	$t\bar{t}$	178
tZq	3.3 ± 0.2	tZq	320
Total expected	95.4 ± 26.6	Total expected	9579
Data	102	Data	102

Table A.2: Number of observed and expected events in the diboson validation region. The left table shows the number of events after luminosity weighting, while the right table shows the raw number of events available.

Process	Scaled events	Process	Raw events
$t\bar{t}V + t\bar{t}H + tWZ$	9.9 ± 0.3	$t\bar{t}V + t\bar{t}H + tWZ$	4448
Diboson	1778.9 ± 533.8	Diboson	64 082
$Z + \text{jets}$	290.8 ± 116.6	$Z + \text{jets}$	1792
$t\bar{t} + tW$	36.5 ± 15.8	$t\bar{t} + tW$	119
tZq	17.7 ± 0.5	tZq	1760
Total expected	2133.7 ± 546.6	Total expected	72 201
Data	1984	Data	1984

Table A.3: Number of observed and expected events in the diboson validation region. The left table shows the number of events after luminosity weighting, while the right table shows the raw number of events available.

Process	Events	Process	Raw events
tZq	35.2 ± 0.7	$t\bar{t}V + t\bar{t}H + tWZ$	9311
$t\bar{t}V + t\bar{t}H + tWZ$	19.9 ± 0.4	Diboson	2456
Diboson	52.7 ± 15.9	$Z + \text{jets}$	275
$Z + \text{jets}$	36.9 ± 15.1	$t\bar{t} + tW$	44
$t\bar{t} + tW$	18.1 ± 8.6	tZq	3438
Total expected	162.7 ± 23.5	Total expected	15 524
Data	141	Data	141

Additional information on systematic uncertainties

A summary of the effect of systematic uncertainties was given in table 7.1. The full breakdown showing the effect of the individual systematic uncertainties on the number of *tZq* events is shown in table B.1. Only uncertainty that cause at least a ±0.05 change in the signal number of events are shown.

Table B.1: Breakdown of the effect of the systematic uncertainties on the number of signal events after the fit for the data. Note that the individual uncertainties can be correlated, and do not necessarily add up quadratically to the total uncertainty. The percentage shows the size of the uncertainty relative to the number of *tZq* events.

Parameter	Events	Fraction [%]
Signal expectation	25.8	-
Total systematic	±8.3	32.2
mu_SIG	±9.4	36.4
tZ Radiation	±2.8	10.8
JER	±1.0	3.8
bTagSF_eigenvars_B_0	±0.7	2.6
LUMI	±0.5	2.1
JES JET_Flavor_Composition	±0.5	2.0
stat_nominal_NNOutput_bin_9	±0.4	1.7
leptonSF_EL_SF_ID	±0.4	1.4
leptonSF_MU_SF_ID_SYST	±0.3	1.3
stat_nominal_NNOutput_bin_8	±0.3	1.2
stat_nominal_NNOutput_bin_4	±0.3	1.0
bTagSF_eigenvars_B_1	±0.3	1.0
stat_nominal_NNOutput_bin_7	±0.3	1.0
PDFWeights13	±0.2	0.8

Parameter	Events	Fraction [%]
JES JET_Pileup_RhoTopology	±0.2	0.8
JES JET_EtaIntercalibration_Modelling	±0.2	0.8
stat_nominal_NNOutput_bin_5	±0.2	0.7
stat_nominal_NNOutput_bin_6	±0.2	0.6
JES JET_Pileup_PtTerm	±0.2	0.6
JES JET_EffectiveNP_2	±0.1	0.5
JES JET_BJES_Response	±0.1	0.5
stat_nominal_NNOutput_bin_3	±0.1	0.5
bTagSF_eigenvars_B_2	±0.1	0.5
PDFWeights3	±0.1	0.5
stat_nominal_NNOutput_bin_2	±0.1	0.4
JES JET_EtaIntercalibration_TotalStat	±0.1	0.4
leptonSF_MU_SF_Isol_SYST	±0.1	0.4
MUON_SCALE	±0.1	0.4
leptonSF_MU_SF_ID_STAT	±0.1	0.4
leptonSF_EL_SF_Reco	±0.1	0.3
leptonSF_EL_SF_Isol	±0.1	0.3
JES JET_Flavor_Response	±0.1	0.3
stat_nominal_NNOutput_bin_1	±0.1	0.3
PDFWeights22	±0.1	0.3
JES JET_EtaIntercalibration_NonClosure	±0.1	0.3
JES JET_EffectiveNP_1	±0.1	0.3
EG_RESOLUTION_ALL	±0.1	0.3
PDFWeights9	±0.1	0.3
PDFWeights17	±0.1	0.2
MET_SoftTrk_ResoPerp	±0.1	0.2
JES JET_Pileup_OffsetNPV	±0.1	0.2
leptonSF_MU_SF_TTVA_STAT	±0.1	0.2
PDFWeights4	±0.1	0.2
PDFWeights19	±0.1	0.2
leptonSF_MU_SF_TTVA_SYST	±0.1	0.2
PDFWeights28	±0.1	0.2
EG_SCALE_ALL	±0.1	0.2
PDFWeights5	±0.1	0.2

Comparisons between the nominal and the up and down variations of significant systematic uncertainties templates are show in. The effect on the rate and the shape of the NN discriminant for the signal and background processes are shown. All templates are shown before the pruning and symmetrisation procedure.
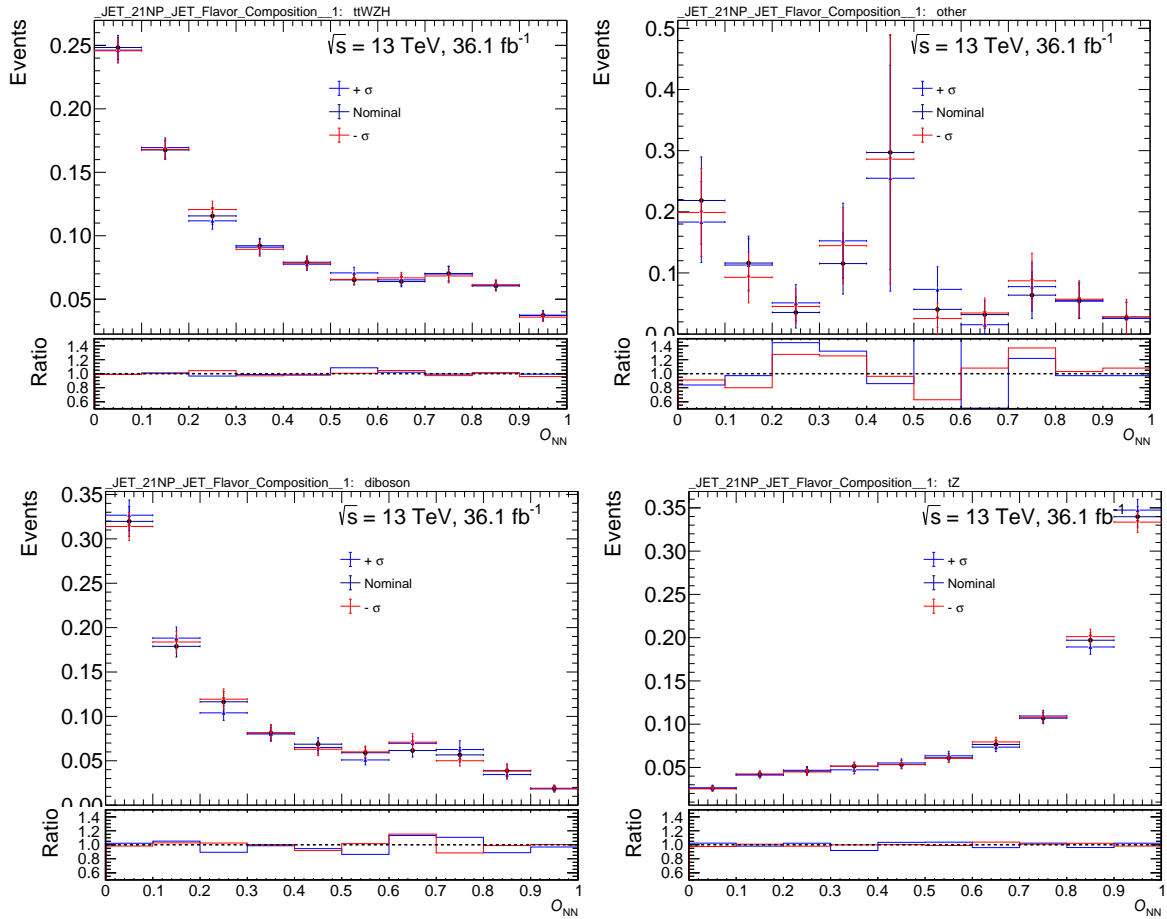
Figure B.1: Comparison between nominal (in black) and the $+1\sigma$ (in blue) and -1σ (in red) variations of the JES flavour composition uncertainty for the $t\bar{t}V + t\bar{t}H + tWZ$ and $t\bar{t}$ template (top row) and the diboson and tZq, bottom row.
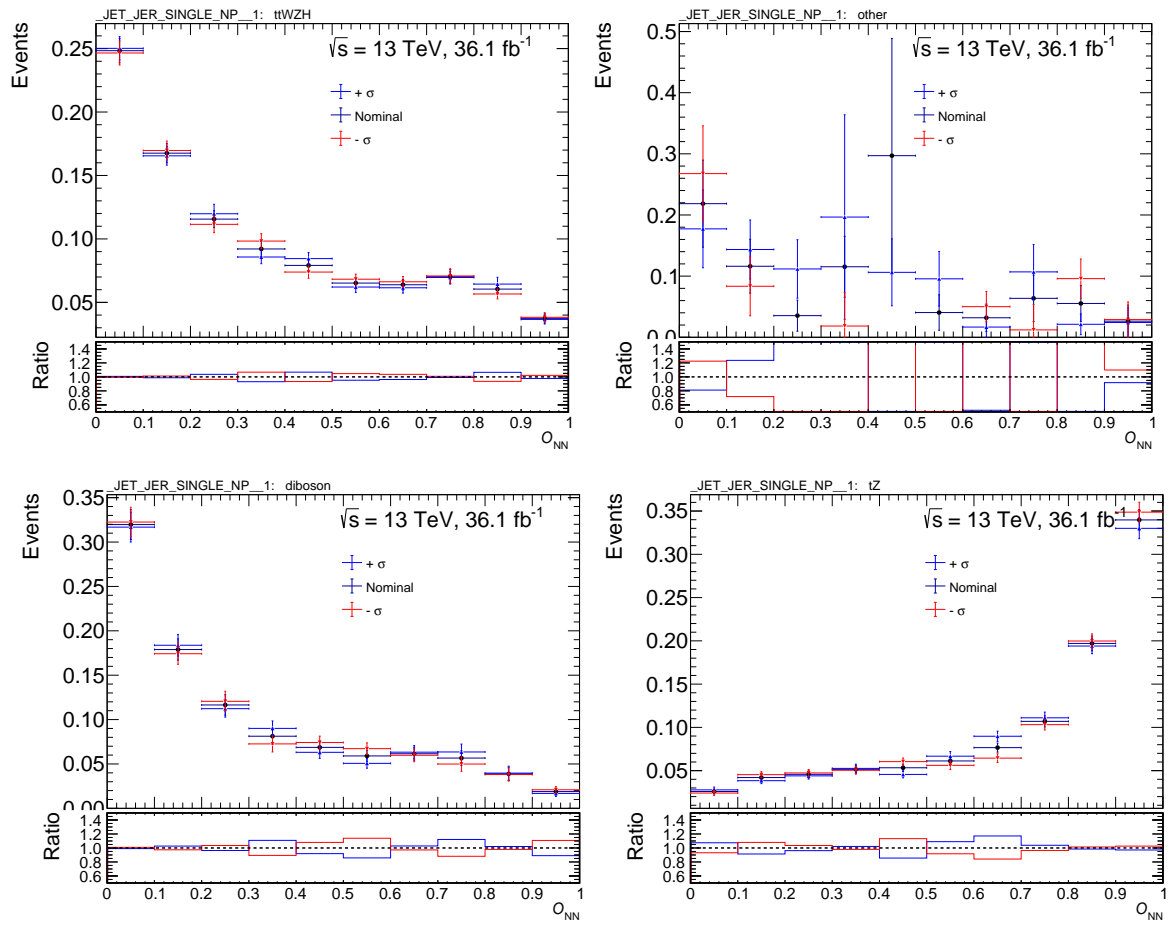
Figure B.2: Comparison between nominal (in black) and the $+1\sigma$ (in blue) and -1σ (in red) variations of the JER uncertainty for the $t\bar{t}V + t\bar{t}H + tWZ$ and $t\bar{t}$ template (top row) and the diboson and tZq, bottom row.
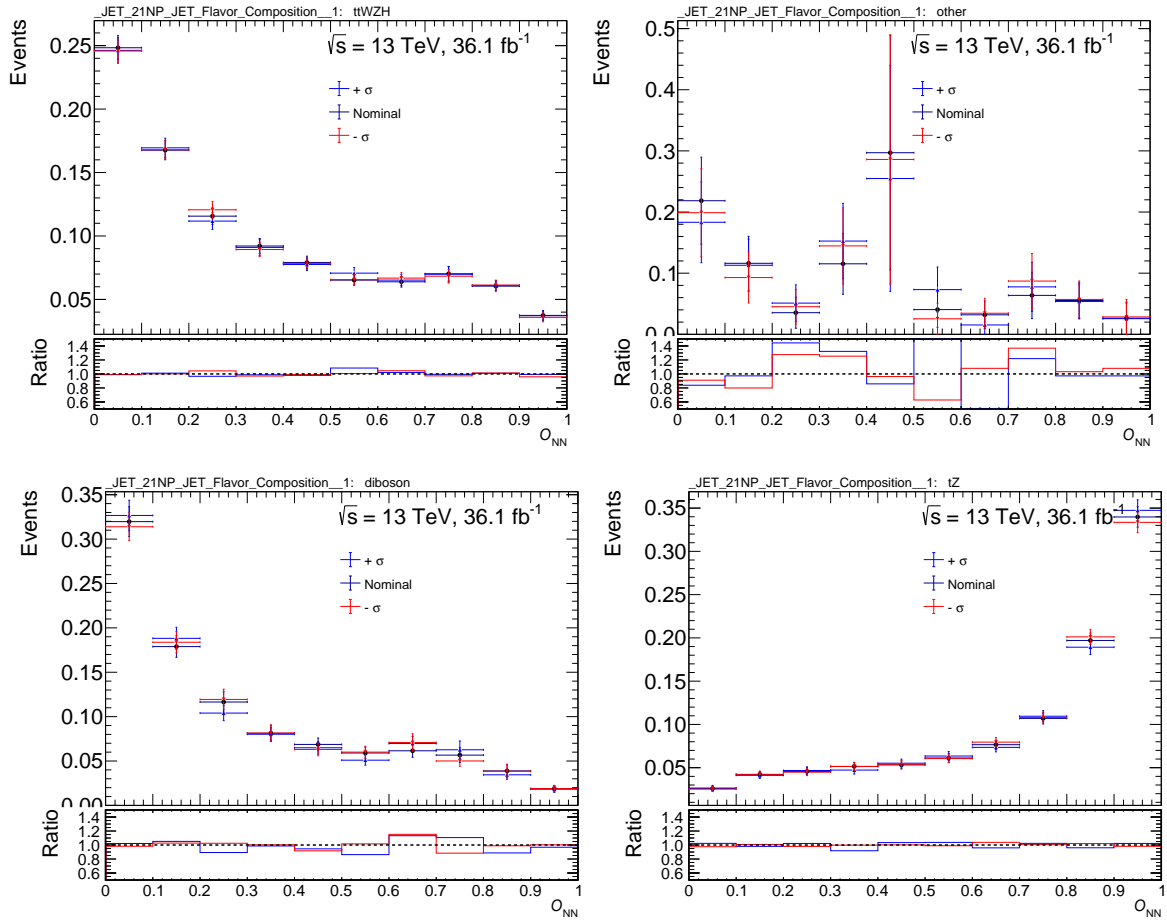
Figure B.3: Comparison between nominal (in black) and the $+1\sigma$ (in blue) and -1σ (in red) variations of the JES flavour composition uncertainty for the $t\bar{t}V + t\bar{t}H + tWZ$ and $t\bar{t}$ template (top row) and the diboson and tZq, bottom row.
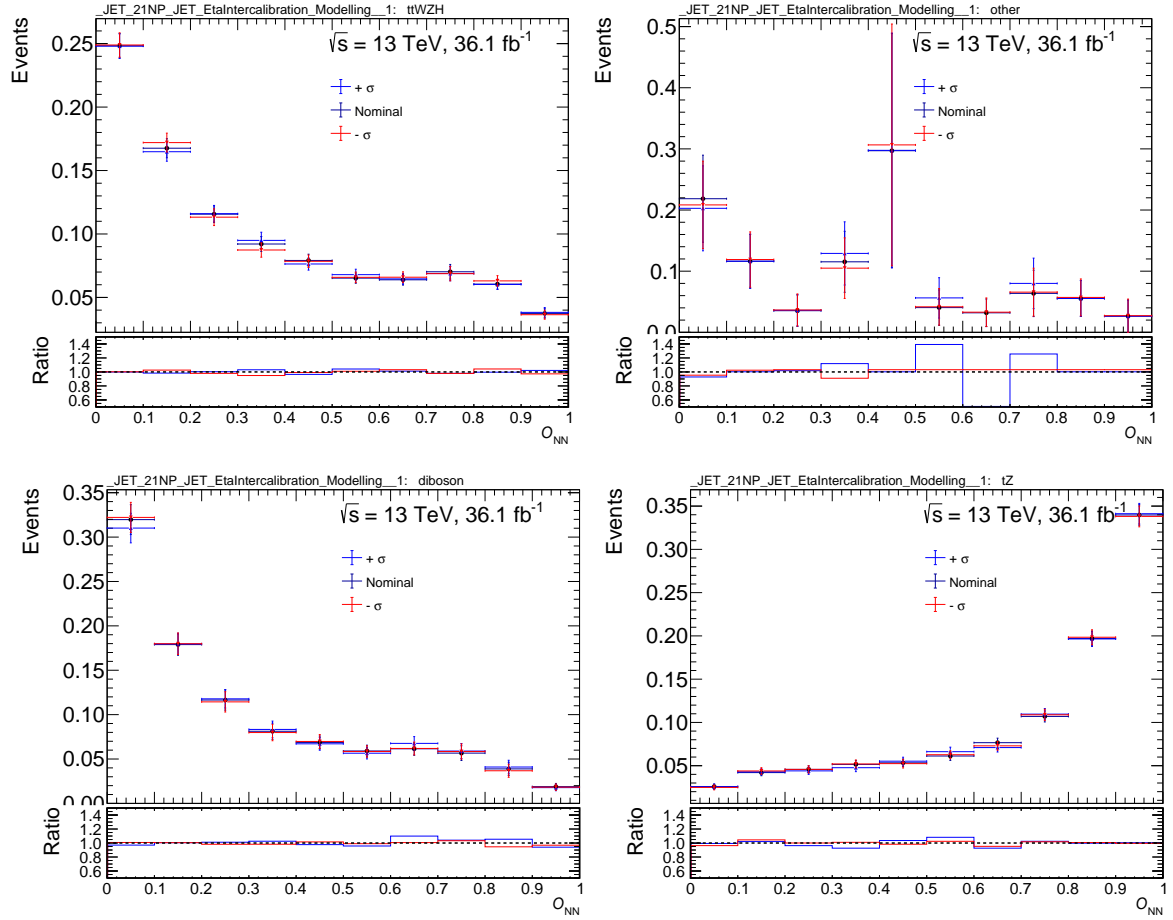
Figure B.4: Comparison between nominal (in black) and the $+1\sigma$ (in blue) and -1σ (in red) variations of the JES η interacalibration modelling uncertainty for the $t\bar{t}V + t\bar{t}H + tWZ$ and $t\bar{t}$ template (top row) and the diboson and tZq, bottom row.
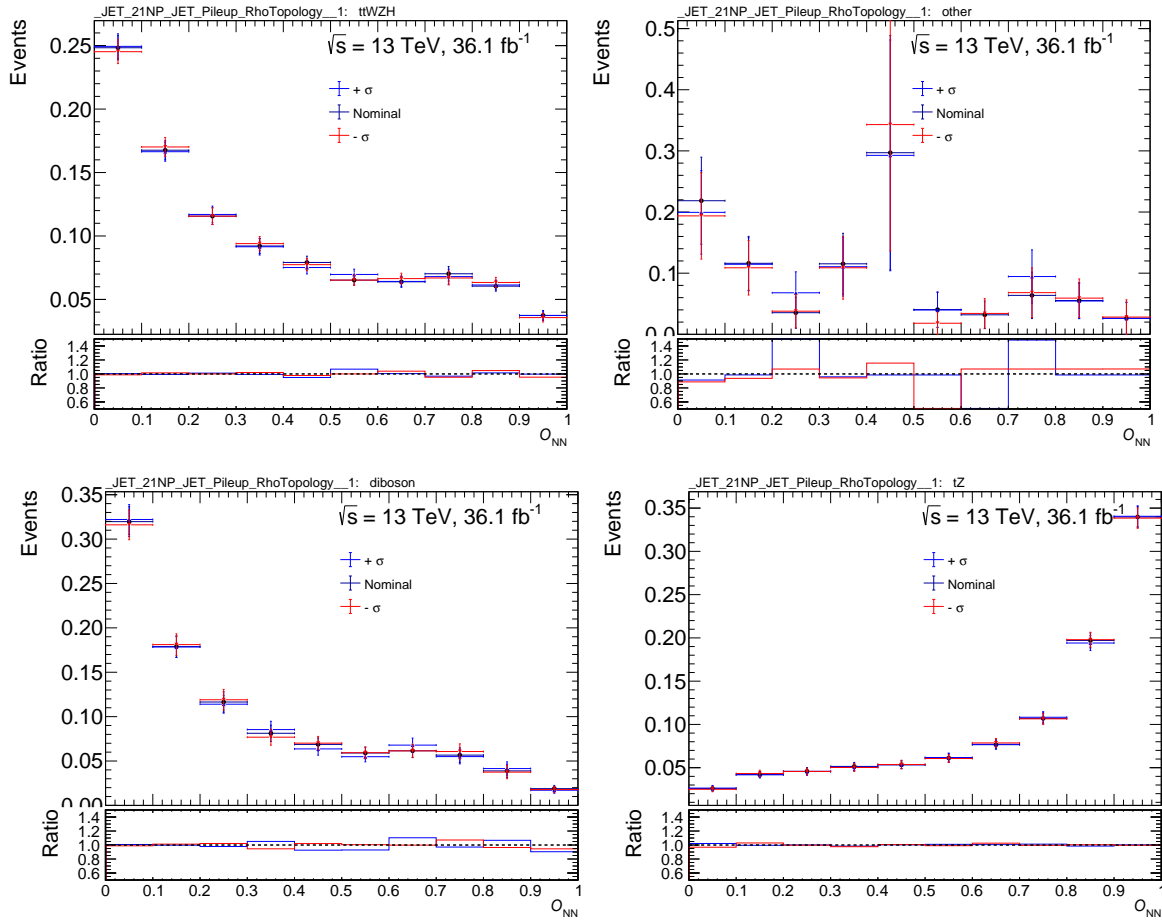
Figure B.5: Comparison between nominal (in black) and the $+1\sigma$ (in blue) and -1σ (in red) variations of the JES pile-up ρ topology uncertainty for the $t\bar{t}V + t\bar{t}H + tWZ$ and $t\bar{t}$ template (top row) and the diboson and tZq, bottom row.
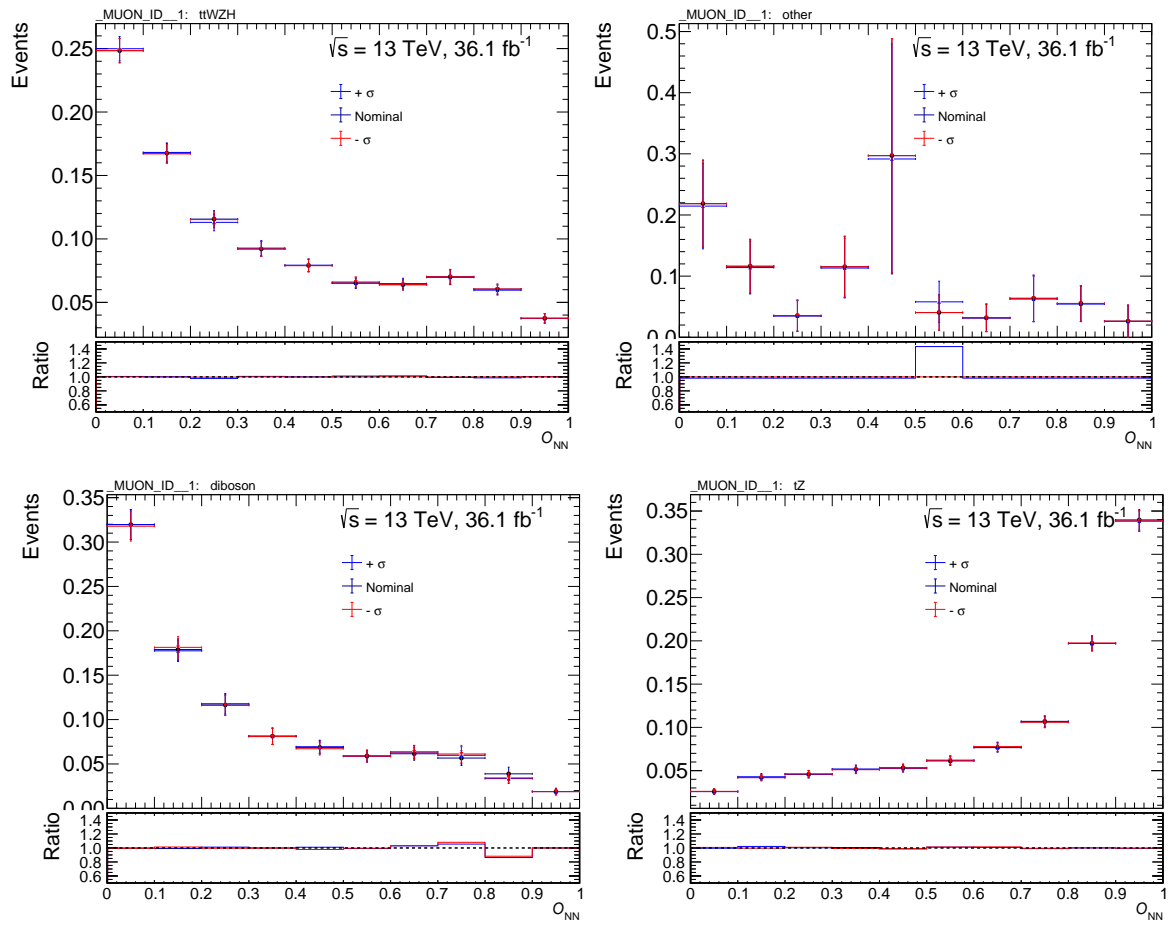
Figure B.6: Comparison between nominal (in black) and the $+1\sigma$ (in blue) and -1σ (in red) variations of the Muon ID uncertainty for the $t\bar{t}V + t\bar{t}H + tWZ$ and $t\bar{t}$ template (top row) and the diboson and tZq, bottom row.

Additional Studies on non-prompt lepton background estimation

C.1 Additional Studies on $t\bar{t}$ background estimation

In order to cross-check the stability of the default approach (namely the use of a single scale factor), two different alternative methods are tested and presented. These include calculating a p_{T}-dependent $SF_{\mathrm{data/MC}}$ or separate factors depending on the flavour of the fake lepton. A drawback for both of these approaches is that the statistics will be very low. All these strategies were investigated using the Version 14 single-top ntuples and yield results that are consistent with each other within the considered uncertainties. Comparisons between these methods and the default, previously presented approach are shown in the following.

The possibility of deriving a flavour dependent SF relies on the fact that, because of the applied selection, one can clearly separate between events where the fake lepton is a muon or an electron. Namely, events of the type $\mu^{\pm}\mu^{\pm}e^{\mp}$ have a fake muon, since the opposite sign electron–muon pair must come from the $t\bar{t}$ pair. Similarly, events with $e^{\pm}e^{\pm}\mu^{\mp}$ contain two real leptons and one fake electron. As mentioned above, a drawback of separating events into these two categories will be the very low statistics in each of them.

The corresponding number of events and calculated scale factors are listed in Table C.1. Again, the errors on the scale factors include the statistical errors on the observed and predicted number of events.

Table C.1: Number of expected and observed events in the $t\bar{t}$ OSOF CR. The channels separate between events that have a fake electron (top row) and fake muon (bottom row). The error on the calculated SF includes statistical errors on data and MC predictions.

Channel	$t\bar{t}$ MC	All-$t\bar{t}$ MC	Total MC	Data	$SF_{\mathrm{data/MC}}$
$e^{\pm}e^{\pm}\mu^{\mp}$	5.80 ± 1.40	1.02 ± 0.11	6.83 ± 1.40	7	1.03 ± 0.52
$\mu^{\pm}\mu^{\pm}e^{\mp}$	3.05 ± 0.90	0.99 ± 0.06	4.03 ± 0.90	7	1.97 ± 1.05

In order to obtain the final $t\bar{t}$ estimation using this strategy, the scale factors are applied according to whether the MC event had a fake electron or muon.

For completeness, we can calculate the final number of $t\bar{t}$ events in the SR, after applying the previ-

ously derived SF. The results are shown in Table C.2.

Table C.2: Numbers of $t\bar{t}$ expected events in the tZq signal region, after applying the lepton flavoured dependent $SF_{data/MC}$ derived in the fake-lepton-dominated $t\bar{t}$ region.

Channel	Event numbers
$t\bar{t} \times SF_{\mu\text{-fake}}$	6.9 ± 3.5
$t\bar{t} \times SF_{e\text{-fake}}$	19.3 ± 11.0
$t\bar{t}$ total	26.2 ± 11.5

As a second cross-check, the same procedure was applied in bins of p_T of the softest lepton that is associated to the Z boson. This parametrisation was chosen because, as seen from the truth level studies, this lepton is the one that is most often a non-prompt lepton.

The same definition for the $t\bar{t}$ control region is used and the corresponding p_T distribution is shown in Figure C.1. Table C.3 shows the derived scale factors for the different bins in transverse momentum.
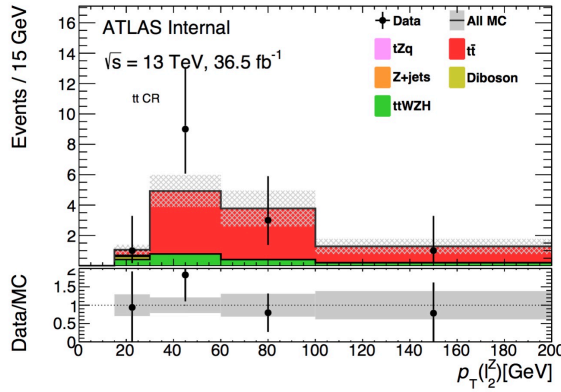
Figure C.1: Control plot for the p_T of the softest lepton associated to the Z boson in the $t\bar{t}$ control region used for calculating the data MC scale factor. The uncertainty band includes only statistical uncertainties.

In order to compare to the unbinned estimation, these scale factors have been applied to the $t\bar{t}$ MC prediction in both the signal and the validation region. These results are summarised in Table C.4. Note that in the p_T binned estimation the error on the individual scale factors is not yet propagated to the fake contribution estimation. For completeness, the numbers obtained from the unbinned estimation were added in the last columns. The two agree within the corresponding uncertainties. For a fair comparison however, an unbinned estimation without separating into flavour-dependent factors is also considered.

When looking at all the calculated scale factors, one sees the MC prediction does well in predicting the number of $t\bar{t}$ events. The scale factors for both the electron and muon contributions are consistent with 1, within the computed uncertainties.

C.2 Additional Studies on Z + jets background estimation

Table C.3: Data/MC SF derived in bins of p_T Z_2.

Process	Bin 2	Bin 3	Bin 4	Bin 5
Z + jets	0.07 ± 0.07	0 ± 0	0 ± 0	0 ± 0
Diboson	0.20 ± 0.14	0 ± 0	0 ± 0	0 ± 0
$t\bar{t}V + t\bar{t}H + tWZ$	0.42 ± 0.05	0.78 ± 0.06	0.41 ± 0.04	0.20 ± 0.03
tZq	0.03 ± 0.02	0.01 ± 0.01	0 ± 0	0.01 ± 0.01
$t\bar{t} + tW$	0.34 ± 0.27	4.14 ± 1.05	3.36 ± 1.18	1.07 ± 0.49
AllMC - $t\bar{t}$	0.72 ± 0.25	0.79 ± 0.14	0.41 ± 0.04	0.21 ± 0.12
Data	1	9	3	1
SF	0.81 ± 3.07	1.98 ± 0.88	0.77 ± 0.58	0.74 ± 1.00

Table C.4: Number of events after applying the SF derived in bins of p_T Z_2.

Process	Bin 2	Bin 3	Bin 4	Bin 5	Total	Unbinned total
$t\bar{t} \times$ SF (SR)	0.4 ± 0.3	3.1 ± 1.4	11.3 ± 3.1	2.2 ± 0.8	16.9 ± 3.5	25.5 ± 12.6
$t\bar{t} \times$ SF (tt VR)	1.7 ± 0.6	24.7 ± 4.4	26.4 ± 4.2	7.5 ± 1.6	60.3 ± 6.3	73.9 ± 26.8
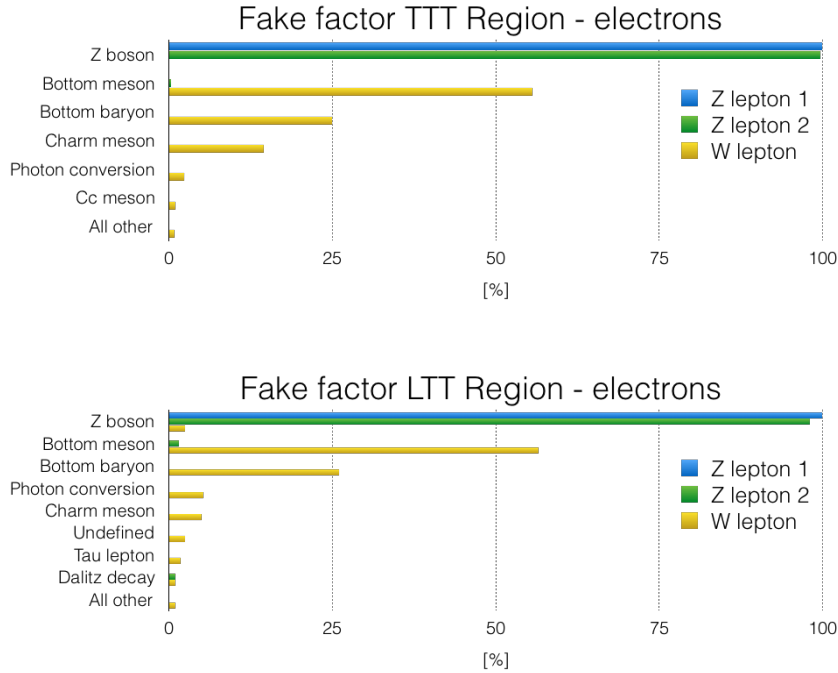
Figure C.2: Origin of the leptons in the Z + jets sample for events that have a non-prompt electron. The plot shows the fake factor region with three tight leptons (top row) and two tight and one loose lepton (bottom row). The particle of origin is shown on the y axis. All processes that contribute with less than 1 % are included in to the "All other" category. The highest transverse momentum lepton candidate from the Z boson is shown in blue and the second highest p_T lepton from the Z boson is shown in green. The lepton associated to the W is depicted in yellow.
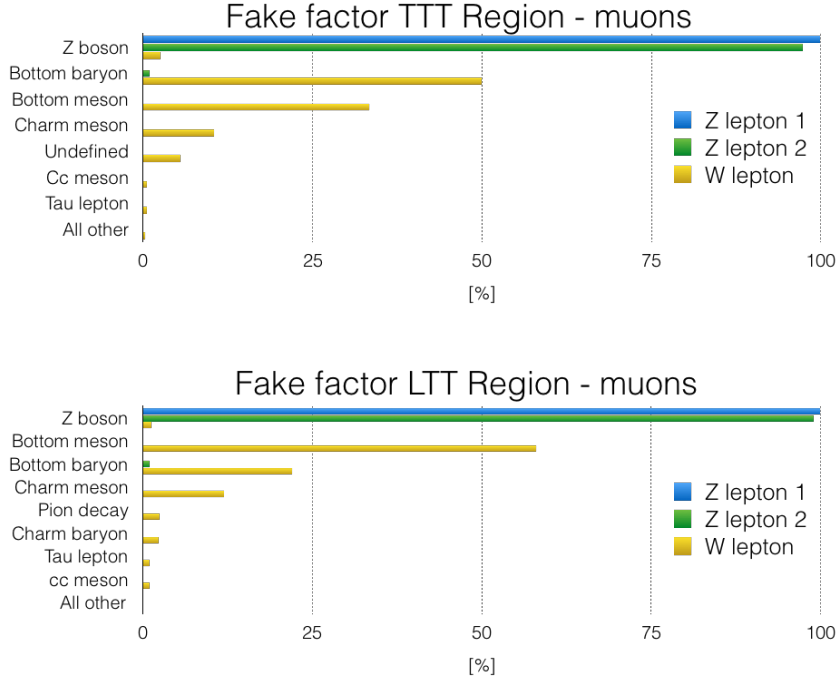
Figure C.3: Origin of the leptons in the Z + jets sample for events that have a non-prompt muon. The plot shows the fake factor region with three tight leptons (top row) and two tight and one loose lepton (bottom row). The particle of origin is shown on the y axis. All processes that contribute with less than 1 % are included in to the "All other" category. The highest transverse momentum lepton candidate from the Z boson is shown in blue and the second highest p_T lepton from the Z boson is shown in green. The lepton associated to the W is depicted in yellow.

Table C.5: Number of expected and observed events in the $t\bar{t}$ OSOF LTT region. The channels separate between events that have a fake electron (first two top rows) and fake muons (bottom rows). The error on the calculated SF includes statistical errors on data and MC predictions.

Channel	$t\bar{t}$ MC	All-$t\bar{t}$ MC	Data	$SF_{data/MC}$
$e^{\pm}e^{\pm}\mu^{\mp}$ bin 1	19.63 ± 8.66	0.09 ± 0.02	13	0.66 ± 0.34
$e^{\pm}e^{\pm}\mu^{\mp}$ bin 2	26.52 ± 6.65	0.19 ± 0.02	18	0.67 ± 0.23
$\mu^{\pm}\mu^{\pm}e^{\mp}$ bin 1	10.47 ± 4.72	0.05 ± 0.02	7	0.66 ± 0.39
$\mu^{\pm}\mu^{\pm}e^{\mp}$ bin 2	7.58 ± 2.19	0.10 ± 0.02	15	1.97 ± 0.76
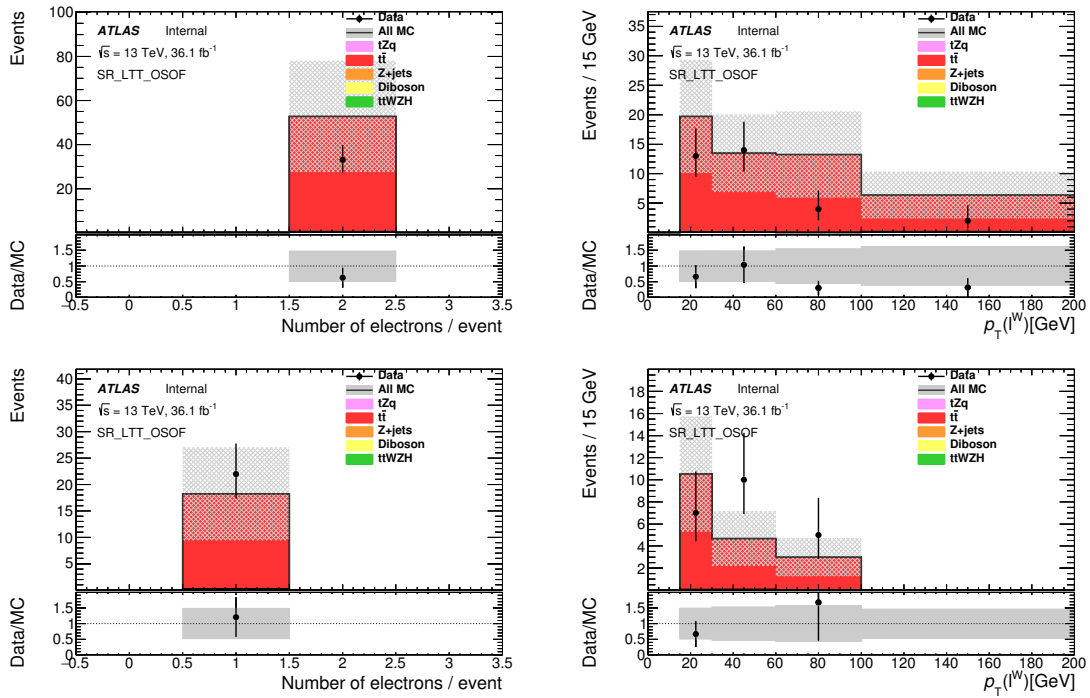
Figure C.4: Distributions of the number of electrons in the event (left) and the p_T of the lepton associated to the W boson (right) for the $t\bar{t}$ control region (signal region with OSOF lepton pair) when one of the leptons is loose-not-tight. The top row corresponds to events that have a fake electron, while in the bottom row the lepton that we associate to the W boson is a muon. The uncertainty band includes only statistical uncertainties.

tZq event displays

Event displays are a great way to visualise how particles interact with the detector, as well as study individual event topologies.

Figure D.1 and figure D.2 show *tZq* candidate events selected from the *p–p* collision data collected by the ATLAS collaboration in 2015 and 2016 respectively. Both figures have the same structure. The image on the left shows a $x - y$ view of the detector (transverse plane), while the view on the right is along the *x*-axis, in the $y - z$ plane. The details of the event, such as Run Number, Event Number and the time at which the event was recorded are listed in the top right corner.

Events with high NN score were chosen, making sure that they are likely to come from *tZq* production. The NN output goes from 0 to 1, with 1 for signal-like events and 0 for background-like.

The event shown in figure D.1 contains three electrons, one *b*-jet and one untagged jet that has a large pseudorapidity and a NN score of 0.93. The p_T values for all objects can be read in the caption of the figure. A forth lepton appears on the event display. This is a muon and is shown in red. Because the muon is very close to the *b*-tagged jet, it is likely that it originates from a *b* hadron decay. Since this event passes the trilepton event selection, it is probable that either the muon has low p_T and does not pass the 15 GeV cut, or it is removed by the overlap removal procedure.

Figure D.2 shows an event display with a NN score of 0.94. Again, the kinematic properties of the reconstructed objects are given in the caption. The two opposite sign, same flavour lepton pair is formed by two muons, while the third lepton is an electron. This event also has the typical single top-quark *t*-channel production signature: an untagged jet going in the forward direction. Additionally, the jet has high p_T (252 GeV), which is one of the features that is found to be very significant in discriminating between signal and background according to the NN.
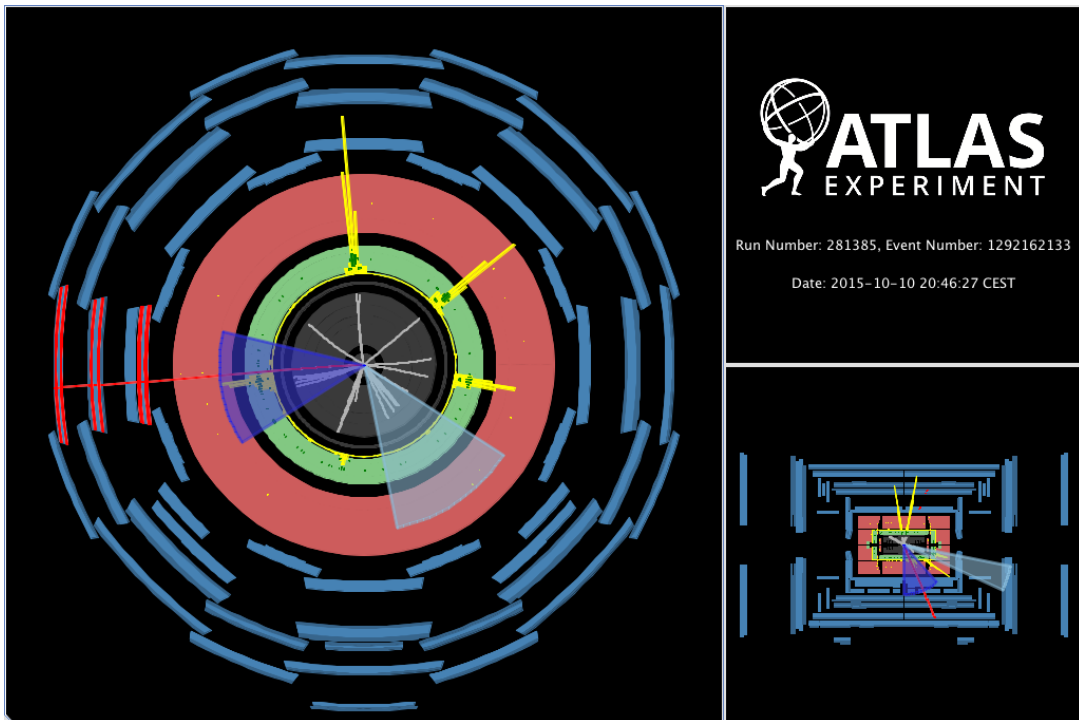
Figure D.1: Event display for one *tZq* candidate event from the data collected in 2015. The event was collected during the run 281385 and has O_{NN} = 0.93. This event contains three isolated electrons. They have $p_T(e_1)$ = 78 GeV, $p_T(e_2)$ = 55 GeV and $p_T(e_3)$ = 54 GeV. The forward jet has p_T = 107 GeV . The *b*-jet has p_T = 86 GeV. The muon is close to the *b*-jet and probably comes from the decay of a *b* hadron. The muon track is shown in red, electromagnetic clusters in yellow, inner detector tracks in grey. The blue and grey cones represent the *b*-jet and the forward jet respectively.
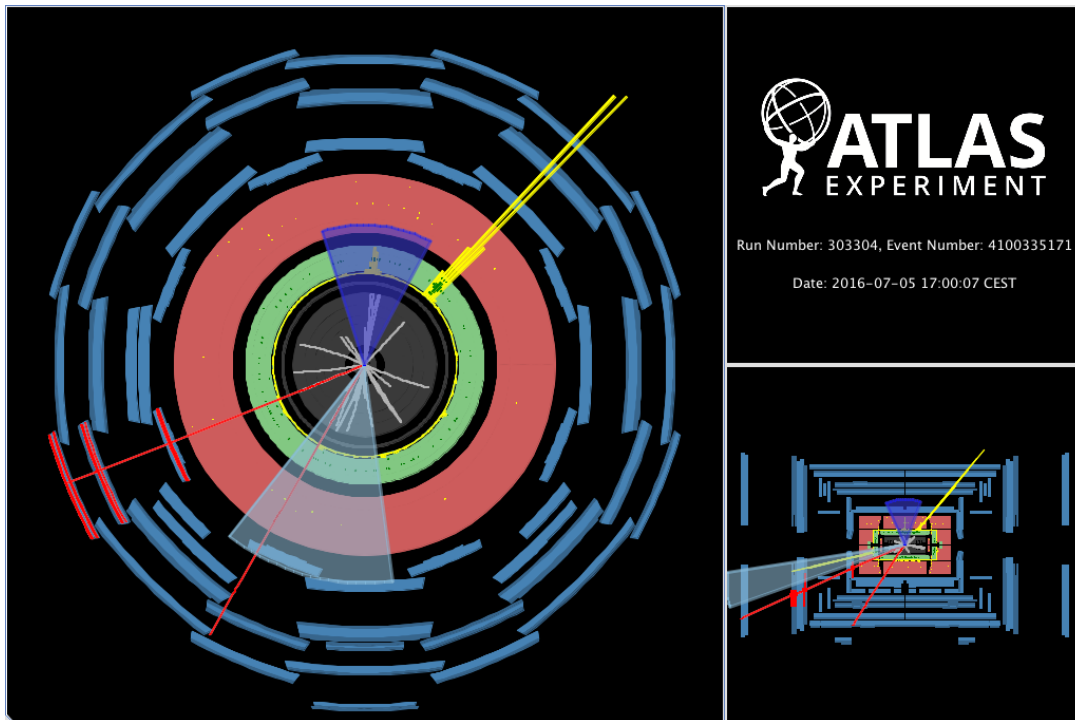
Figure D.2: Event display for one *tZq* candidate event from the data collected in 2016. The event was collected during the run 303304 and has O_{NN} = 0.94. This event contains one electron and two muons. The electron has $p_T(e)$ = 144 GeV, and the two muons have $p_T(\mu_1)$ = 159 GeV and $p_T(\mu_2)$ = 41 GeV. The forward jet has p_T = 252 GeV. The *b*-jet has p_T = 68 GeV. Muon tracks are shown in red, electromagnetic clusters in yellow, inner detector tracks in grey. The blue and grey cones represent the *b*-jet and the forward jet respectively.

Bibliography

[1] ATLAS Collaboration, "Measurement of the production cross-section of a single top quark in association with a *Z* boson in proton–proton collisions at 13 TeV with the ATLAS detector", *Phys. Lett. B* 780 (2018) 557, DOI: 10.1016/j.physletb.2018.03.023, arXiv: 1710.03659 [hep-ex].

[2] F. Halzen and A. D. Martin, *Quarks and leptons: and introductory course in modern particle physics*, 1984, ISBN: 0471887412, 9780471887416.

[3] M. Thomson, *Modern particle physics*, 2013, ISBN: 9781107034266, URL: http://www-spires.fnal.gov/spires/find/books/www?cl=QC793.2.T46::2013.

[4] U. Husemann, "Top-Quark Physics: Status and Prospects", *Prog. Part. Nucl. Phys.* 95 (2017) 48–97, DOI: 10.1016/j.ppnp.2017.03.002, arXiv: 1704.01356 [hep-ex].

[5] A. Giammanco and R. Schwienhorst, "Single top-quark production at the Tevatron and the LHC" (2017), arXiv: 1710.10699 [hep-ex].

[6] D. Abbaneo et al., "A Combination of preliminary electroweak measurements and constraints on the standard model" (2001), arXiv: hep-ex/0112021 [hep-ex].

[7] C. Patrignani et al., "Review of Particle Physics", *Chin. Phys.* C40.10 (2016) 100001, DOI: 10.1088/1674-1137/40/10/100001.

[8] I. C. Brock and T. Schorner-Sadenius, eds., *Physics at the Terascale*, 2011, URL: http://www.wiley-vch.de/publish/dt/books/ISBN3-527-41001-5.

[9] R. Placakyte, "Parton Distribution Functions", 2011, arXiv: 1111.5452 [hep-ph], URL: https://inspirehep.net/record/954990/files/arXiv:1111.5452.pdf.

[10] T. Plehn, "LHC Phenomenology for Physics Hunters", 2010 125–180, DOI: 10.1142/9789812838360_0003, arXiv: 0810.2281 [hep-ph], URL: https://inspirehep.net/record/799244/files/arXiv:0810.2281.pdf.

[11] CDF Collaboration, "A Limit on the top quark mass from $p\bar{p}$ collisions at $\sqrt{s}$ = 1.8 TeV", *Phys. Rev.* D45 (1992) 3921–3948, DOI: 10.1103/PhysRevD.45.3921.

[12] CDF Collaboration, "Observation of top quark production in $\bar{p}p$ collisions", *Phys. Rev. Lett.* 74 (1995) 2626–2631, DOI: 10.1103/PhysRevLett.74.2626, arXiv: hep-ex/9503002 [hep-ex].

[13] D0 Collaboration, "Observation of the top quark", *Phys. Rev. Lett.* 74 (1995) 2632–2637, DOI: 10.1103/PhysRevLett.74.2632, arXiv: hep-ex/9503003 [hep-ex].

[14] ATLAS, CDF, CMS and D0 Collaborations,
"First combination of Tevatron and LHC measurements of the top-quark mass" (2014),
arXiv: 1403.4427 [hep-ex].

[15] CDF and D0 Collaborations, "Combination of measurements of the top-quark pair production
cross section from the Tevatron Collider", *Phys. Rev.* D89.7 (2014) 072001,
DOI: 10.1103/PhysRevD.89.072001, arXiv: 1309.7570 [hep-ex].

[16] ATLAS Collaboration,
*Statistical combination of top quark pair production cross-section measurements using
dilepton, single-lepton, and all-hadronic final states at $\sqrt{s}$ = 7 TeV with the ATLAS detector*,
ATLAS-CONF-2012-024, 2012, URL: https://cds.cern.ch/record/1430733.

[17] ATLAS Collaboration,
"Fiducial, total and differential cross-section measurements of *t*-channel single top-quark
production in *pp* collisions at 8 TeV using data collected by the ATLAS detector",
Eur. Phys. J. C 77 (2017) 531, DOI: 10.1140/epjc/s10052-017-5061-9,
arXiv: 1702.02859 [hep-ex].

[18] ATLAS Collaboration,
"Measurement of the inclusive cross-sections of single top-quark and top-antiquark *t*-channel
production in *pp* collisions at $\sqrt{s}$ = 13 TeV with the ATLAS detector", *JHEP* 04 (2017) 086,
DOI: 10.1007/JHEP04(2017)086, arXiv: 1609.03920 [hep-ex].

[19] E. L. Berger et al.,
"NNLO QCD corrections to *t*-channel single top quark production and decay",
Phys. Rev. D 94 (7 Oct. 2016) 071501, DOI: 10.1103/PhysRevD.94.071501,
URL: https://link.aps.org/doi/10.1103/PhysRevD.94.071501.

[20] ATLAS Collaboration, "Measurement of the production cross-section of a single top quark in
association with a *W* boson at 8 TeV with the ATLAS experiment", *JHEP* 01 (2016) 064,
DOI: 10.1007/JHEP01(2016)064, arXiv: 1510.03752 [hep-ex].

[21] ATLAS Collaboration, "Measurement of the cross-section for producing a *W* boson in
association with a single top quark in *pp* collisions at $\sqrt{s}$ = 13 TeV with ATLAS",
JHEP 01 (2018) 063, DOI: 10.1007/JHEP01(2018)063, arXiv: 1612.07231 [hep-ex].

[22] ATLAS Collaboration, "Measurement of differential cross-sections of a single top quark
produced in association with a *W* boson at $\sqrt{s}$ = 13 TeV with ATLAS",
Eur. Phys. J. C 78 (2018) 186, DOI: 10.1140/epjc/s10052-018-5649-8,
arXiv: 1712.01602 [hep-ex].

[23] J. A. Stillings, "Search for the associated production of a W boson and a top quark with the
ATLAS detector at 7 TeV", June 2015, ISBN: BONN-IR-2015-04,
URL: http://cds.cern.ch/record/2054119.

[24] S. Mergelmeyer, "Measurement of the Associated Production of a Single Top Quark and a W
Boson in Single-Lepton Events with the ATLAS Detector", June 2016,
ISBN: BONN-IR-2016-03, URL: http://hss.ulb.uni-bonn.de/2016/4394/4394.htm.

[25] N. Kidonakis, "Two-loop soft anomalous dimensions for single top quark associated
production with a W- or H-", *Phys. Rev.* D82 (2010) 054018,
DOI: 10.1103/PhysRevD.82.054018, arXiv: 1005.4451 [hep-ph].

[26] S. Frixione et al., "Single-top hadroproduction in association with a W boson",
JHEP 07 (2008) 029, DOI: 10.1088/1126-6708/2008/07/029,
arXiv: 0805.3067 [hep-ph].

[27] N. Kidonakis, "NNLL resummation for s-channel single top quark production",
Phys. Rev. D81 (2010) 054028, DOI: 10.1103/PhysRevD.81.054028,
arXiv: 1001.5034 [hep-ph].

[28] ATLAS Collaboration,
"Evidence for single top-quark production in the *s*-channel in proton–proton collisions at
$\sqrt{s}$ = 8 TeV with the ATLAS detector using the Matrix Element Method",
Phys. Lett. B 756 (2016) 228, DOI: 10.1016/j.physletb.2016.03.017,
arXiv: 1511.05980 [hep-ex].

[29] LHCTopWg, *LHCTopWg Summary plots*,
URL: https://twiki.cern.ch/twiki/bin/view/LHCPhysics/LHCTopWGSummaryPlots.

[30] ATLAS Collaboration, "Evidence for the associated production of the Higgs boson and a top
quark pair with the ATLAS detector", *Phys. Rev. D* 97 (2018) 072003,
DOI: 10.1103/PhysRevD.97.072003, arXiv: 1712.08891 [hep-ex].

[31] ATLAS Collaboration, "Observation of Higgs boson production in association with a top quark
pair at the LHC with the ATLAS detector", *submitted to PLB* (June 2018),
arXiv: 1806.00425 [hep-ex].

[32] CMS Collaboration, "Observation of t$\bar{\text{t}}$H production",
Phys. Rev. Lett. 120 (June 2018) 231801, DOI: 10.1103/PhysRevLett.120.231801,
arXiv: 1804.02610 [hep-ex].

[33] D. de Florian et al.,
"Handbook of LHC Higgs Cross Sections: 4. Deciphering the Nature of the Higgs Sector"
(2016), DOI: 10.23731/CYRM-2017-002, arXiv: 1610.07922 [hep-ph].

[34] ATLAS and CMS Collaborations, "Combined Measurement of the Higgs Boson Mass in *pp*
Collisions at $\sqrt{s}$ = 7 and 8 TeV with the ATLAS and CMS Experiments",
Phys. Rev. Lett. 114 (2015) 191803, DOI: 10.1103/PhysRevLett.114.191803,
arXiv: 1503.07589 [hep-ex].

[35] J. Campbell, R. K. Ellis and R. Röntsch,
"Single top production in association with a Z boson at the LHC",
Phys. Rev. D 87 (2013) 114006, DOI: 10.1103/PhysRevD.87.114006,
arXiv: 1302.3856 [hep-ph].

[36] F. Demartin et al., "Higgs production in association with a single top quark at the LHC",
Eur. Phys. J. C75.6 (2015) 267, DOI: 10.1140/epjc/s10052-015-3475-9,
arXiv: 1504.00611 [hep-ph].

[37] CMS Collaboration, "Search for the associated production of a Higgs boson with a single top
quark in proton–proton collisions at $\sqrt{s}$ = 8 TeV", *JHEP* 06 (2016) 177,
DOI: 10.1007/JHEP06(2016)177, arXiv: 1509.08159 [hep-ex].

[38] J. A. Aguilar-Saavedra, "Top flavor-changing neutral interactions: Theoretical expectations and
experimental detection", *Acta Phys. Polon.* B35 (2004) 2695–2710,
arXiv: hep-ph/0409342 [hep-ph].

[39] CMS Collaboration, "Search for associated production of a *Z* boson with a single top quark and for *tZ* flavour-changing interactions in *pp* collisions at $\sqrt{s}$ = 8 TeV", *JHEP* 07 (2017) 003, DOI: 10.1007/JHEP07(2017)003, arXiv: 1702.01404 [hep-ex].

[40] ATLAS Collaboration,
"Measurement of the $t\bar{t}Z$ and $t\bar{t}W$ production cross sections in multilepton final states using 3.2 fb^{-1} of *pp* collisions at $\sqrt{s}$ = 13 TeV with the ATLAS detector",
Eur. Phys. J. C 77 (2017) 40, DOI: 10.1140/epjc/s10052-016-4574-y,
arXiv: 1609.01599 [hep-ex].

[41] CMS Collaboration, "Measurement of the cross section for top quark pair production in association with a *W* or *Z* boson in proton–proton collisions at $\sqrt{s}$ = 13 TeV" (2017),
arXiv: 1711.02547 [hep-ex].

[42] R. D. Ball et al., "Parton distributions for the LHC run II", *JHEP* 04 (2015) 40,
DOI: 10.1007/JHEP04(2015)040, arXiv: 1410.8849 [hep-ph].

[43] CMS Collaboration, "Measurement of the associated production of a single top quark and a *Z* boson in *pp* collisions at $\sqrt{s}$ = 13 TeV", *Phys. Lett. B* 779 (2018) 358,
DOI: 10.1016/j.physletb.2018.02.025, arXiv: 1712.02825 [hep-ex].

[44] L. Evans and P. Bryant, "LHC Machine", *JINST* 3 (2008) S08001,
DOI: 10.1088/1748-0221/3/08/S08001.

[45] ATLAS Collaboration, "The ATLAS Experiment at the CERN Large Hadron Collider",
JINST 3 (2008) S08003, DOI: 10.1088/1748-0221/3/08/S08003.

[46] CMS Collaboration, "The CMS Experiment at the CERN LHC", *JINST* 3 (2008) S08004,
DOI: 10.1088/1748-0221/3/08/S08004.

[47] LHCb Collaboration, "The LHCb Detector at the LHC", *JINST* 3 (2008) S08005,
DOI: 10.1088/1748-0221/3/08/S08005.

[48] Alice Collaboration, "The ALICE experiment at the CERN LHC", *JINST* 3 (2008) S08002,
DOI: 10.1088/1748-0221/3/08/S08002.

[49] C. De Melis, "The CERN accelerator complex. Complexe des accélérateurs du CERN"
(July 2016), URL: https://cds.cern.ch/record/2197559.

[50] J. Pequenao, "Computer generated image of the whole ATLAS detector", Mar. 2008,
URL: http://cds.cern.ch/record/1095924.

[51] J. Pequenao, "Computer generated image of the ATLAS inner detector", Mar. 2008,
URL: http://cds.cern.ch/record/1095926.

[52] H. Pernegger, "The Pixel Detector of the ATLAS experiment for LHC Run-2",
JINST 10.06 (2015) C06012, DOI: 10.1088/1748-0221/10/06/C06012.

[53] A. Abdesselam et al., "The barrel modules of the ATLAS semiconductor tracker",
Nucl. Instrum. Meth. A568 (2006) 642–671, DOI: 10.1016/j.nima.2006.08.036.

[54] ATLAS Collaboration, "Operation and performance of the ATLAS semiconductor tracker",
JINST 9 (2014) P08009, DOI: 10.1088/1748-0221/9/08/P08009,
arXiv: 1404.7473 [hep-ex].

[55] J. Pequenao, "Computer Generated image of the ATLAS calorimeter", Mar. 2008,
URL: http://cds.cern.ch/record/1095927.

[56] J. Pequenao, "Computer generated image of the ATLAS Muons subsystem", Mar. 2008, URL: http://cds.cern.ch/record/1095929.

[57] ATLAS Collaboration, "ATLAS muon spectrometer: Technical design report" (1997).

[58] M. z. Nedden, "The LHC Run 2 ATLAS trigger system: design, performance and plans", *JINST* 12.03 (2017) C03024, DOI: 10.1088/1748-0221/12/03/C03024.

[59] ATLAS Collaboration, "Performance of the ATLAS track reconstruction algorithms in dense environments in LHC Run 2", *Eur. Phys. J. C* 77 (2017) 673, DOI: 10.1140/epjc/s10052-017-5225-7, arXiv: 1704.07983 [hep-ex].

[60] ATLAS Collaboration, "Reconstruction of primary vertices at the ATLAS experiment in Run 1 proton–proton collisions at the LHC", *Eur. Phys. J. C* 77 (2017) 332, DOI: 10.1140/epjc/s10052-017-4887-5, arXiv: 1611.10235 [hep-ex].

[61] ATLAS Collaboration, "Measurement of the Inelastic Proton–Proton Cross Section at $\sqrt{s}$ = 13 TeV with the ATLAS Detector at the LHC", *Phys. Rev. Lett.* 117 (2016) 182002, DOI: 10.1103/PhysRevLett.117.182002, arXiv: 1606.02625 [hep-ex].

[62] ATLAS Collaboration, "Topological cell clustering in the ATLAS calorimeters and its performance in LHC Run 1", *Eur. Phys. J. C* 77 (2017) 490, DOI: 10.1140/epjc/s10052-017-5004-5, arXiv: 1603.02934 [hep-ex].

[63] ATLAS Collaboration, "Electron reconstruction and identification efficiency measurements with the ATLAS detector using the 2011 LHC proton–proton collision data", *Eur. Phys. J. C* 74 (2014) 2941, DOI: 10.1140/epjc/s10052-014-2941-0, arXiv: 1404.2240 [hep-ex].

[64] ATLAS Collaboration, *Electron identification measurements in ATLAS using $\sqrt{s}$ = 13 TeV data with* 50 *ns bunch spacing*, ATL-PHYS-PUB-2015-041, 2015, URL: https://cds.cern.ch/record/2048202.

[65] ATLAS Collaboration, *Electron and photon energy calibration with the ATLAS detector using data collected in 2015 at $\sqrt{s}$ = 13 TeV*, ATL-PHYS-PUB-2016-015, 2016, URL: https://cds.cern.ch/record/2203514.

[66] ATLAS Collaboration, *Electron efficiency measurements with the ATLAS detector using the 2015 LHC proton–proton collision data*, ATLAS-CONF-2016-024, 2016, URL: https://cds.cern.ch/record/2157687.

[67] ATLAS Collaboration, "Muon reconstruction performance of the ATLAS detector in proton–proton collision data at $\sqrt{s}$ = 13 TeV", *Eur. Phys. J. C* 76 (2016) 292, DOI: 10.1140/epjc/s10052-016-4120-y, arXiv: 1603.05598 [hep-ex].

[68] ATLAS Collaboration, "Performance of the ATLAS Trigger System in 2015", *Eur. Phys. J. C* 77 (2017) 317, DOI: 10.1140/epjc/s10052-017-4852-3, arXiv: 1611.09661 [hep-ex].

[69] G. P. Salam, "Towards Jetography", *Eur. Phys. J.* C67 (2010) 637–686, DOI: 10.1140/epjc/s10052-010-1314-6, arXiv: 0906.1833 [hep-ph].

[70] M. Cacciari and G. P. Salam, "Dispelling the N^3 myth for the k_t jet-finder", *Phys. Lett. B* 641 (2006) 57, DOI: 10.1016/j.physletb.2006.08.037, arXiv: hep-ph/0512210.

[71] M. Cacciari, G. P. Salam and G. Soyez, "The anti-k_t jet clustering algorithm",
JHEP 04 (2008) 063, DOI: 10.1088/1126-6708/2008/04/063, arXiv: 0802.1189.

[72] ATLAS Collaboration,
"Jet reconstruction and performance using particle flow with the ATLAS Detector",
Eur. Phys. J. C 77 (2017) 466, DOI: 10.1140/epjc/s10052-017-5031-2,
arXiv: 1703.10485 [hep-ex].

[73] ATLAS Collaboration, "Jet energy measurement and its systematic uncertainty in
proton–proton collisions at $\sqrt{s}$ = 7 TeV with the ATLAS detector",
Eur. Phys. J. C 75 (2015) 17, DOI: 10.1140/epjc/s10052-014-3190-y,
arXiv: 1406.0076 [hep-ex].

[74] ATLAS Collaboration, "Jet energy scale measurements and their systematic uncertainties in
proton–proton collisions at $\sqrt{s}$ = 13 TeV with the ATLAS detector",
Phys. Rev. D 96 (2017) 072002, DOI: 10.1103/PhysRevD.96.072002,
arXiv: 1703.09665 [hep-ex].

[75] ATLAS Collaboration, "Performance of pile-up mitigation techniques for jets in pp collisions
at $\sqrt{s}$ = 8 TeV using the ATLAS detector", *Eur. Phys. J. C* 76 (2016) 581,
DOI: 10.1140/epjc/s10052-016-4395-z, arXiv: 1510.03823 [hep-ex].

[76] ATLAS Collaboration,
Optimisation of the ATLAS b-tagging performance for the 2016 LHC Run,
ATL-PHYS-PUB-2016-012, 2016, URL: https://cds.cern.ch/record/2160731.

[77] ATLAS Collaboration, *Performance of missing transverse momentum reconstruction with the
ATLAS detector in the first proton–proton collisions at $\sqrt{s}$ = 13 TeV*,
ATL-PHYS-PUB-2015-027, 2015, URL: https://cds.cern.ch/record/2037904.

[78] M. Aaboud et al., "Performance of missing transverse momentum reconstruction with the
ATLAS detector using proton-proton collisions at $\sqrt{s}$ = 13 TeV" (2018),
arXiv: 1802.08168 [hep-ex].

[79] ATLAS Collaboration, *Luminosity plots for Run2 operations*,
URL: https://twiki.cern.ch/twiki/bin/view/AtlasPublic/
LuminosityPublicResultsRun2#Multiple_Year_Collision_Plots.

[80] ATLAS Collaboration, "Luminosity determination in pp collisions at $\sqrt{s}$ = 8 TeV using the
ATLAS detector at the LHC", *Eur. Phys. J. C* 76 (2016) 653,
DOI: 10.1140/epjc/s10052-016-4466-1, arXiv: 1608.03953 [hep-ex].

[81] ATLAS Collaboration, "Improved luminosity determination in pp collisions at $\sqrt{s}$ = 7 TeV
using the ATLAS detector at the LHC", *Eur. Phys. J. C* 73 (2013) 2518,
DOI: 10.1140/epjc/s10052-013-2518-3, arXiv: 1302.4393 [hep-ex].

[82] B. Andersson et al., "Parton Fragmentation and String Dynamics",
Phys. Rept. 97 (1983) 31–145, DOI: 10.1016/0370-1573(83)90080-7.

[83] J.-C. Winter, F. Krauss and G. Soff, "A Modified cluster hadronization model",
Eur. Phys. J. C36 (2004) 381–395, DOI: 10.1140/epjc/s2004-01960-8,
arXiv: hep-ph/0311085 [hep-ph].

[84] C. Patrignani et al., "Review of Particle Physics", *Chin. Phys. C* 40.10 (2016) 100001,
DOI: 10.1088/1674-1137/40/10/100001.

[85] A. Buckley et al., "General-purpose event generators for LHC physics",
Phys. Rept. 504 (2011) 145–233, DOI: `10.1016/j.physrep.2011.03.005`,
arXiv: `1101.2599 [hep-ph]`.

[86] P. Nason, "A New method for combining NLO QCD with shower Monte Carlo algorithms",
JHEP 11 (2004) 040, DOI: `10.1088/1126-6708/2004/11/040`, arXiv: `hep-ph/0409146`.

[87] S. Frixione, P. Nason and C. Oleari,
"Matching NLO QCD computations with parton shower simulations: the POWHEG method",
JHEP 11 (2007) 070, DOI: `10.1088/1126-6708/2007/11/070`,
arXiv: `0709.2092 [hep-ph]`.

[88] S. Alioli et al., "A general framework for implementing NLO calculations in shower Monte
Carlo programs: the POWHEG BOX", *JHEP* 06 (2010) 043,
DOI: `10.1007/JHEP06(2010)043`, arXiv: `1002.2581 [hep-ph]`.

[89] J. Alwall et al., "The automated computation of tree-level and next-to-leading order differential
cross sections, and their matching to parton shower simulations", *JHEP* 07 (2014) 079,
DOI: `10.1007/JHEP07(2014)079`, arXiv: `1405.0301 [hep-ph]`.

[90] T. Sjöstrand, S. Mrenna and P. Z. Skands, "PYTHIA 6.4 physics and manual",
JHEP 05 (2006) 026, DOI: `10.1088/1126-6708/2006/05/026`, arXiv: `hep-ph/0603175`.

[91] T. Sjöstrand, S. Mrenna and P. Z. Skands, "A brief introduction to PYTHIA 8.1",
Comput. Phys. Commun. 178 (2008) 852–867, DOI: `10.1016/j.cpc.2008.01.036`,
arXiv: `0710.3820 [hep-ph]`.

[92] P. Z. Skands, "Tuning Monte Carlo generators: The Perugia tunes",
Phys. Rev. D82 (2010) 074018, DOI: `10.1103/PhysRevD.82.074018`,
arXiv: `1005.3457 [hep-ph]`.

[93] J. Pumplin et al.,
"New generation of parton distributions with uncertainties from global QCD analysis",
JHEP 07 (2002) 012, DOI: `10.1088/1126-6708/2002/07/012`,
arXiv: `hep-ph/0201195 [hep-ph]`.

[94] R. Frederix, E. Re and P. Torrielli, "Single-top t-channel hadroproduction in the four-flavour
scheme with POWHEG and aMC@NLO", *JHEP* 09 (2012) 130,
DOI: `10.1007/JHEP09(2012)130`, arXiv: `1207.5391 [hep-ph]`.

[95] S. Agostinelli et al., "GEANT4 – a simulation toolkit",
Nucl. Instrum. Meth. A 506 (2003) 250–303, DOI: `10.1016/S0168-9002(03)01368-8`.

[96] ATLAS Collaboration, "The ATLAS Simulation Infrastructure", *Eur. Phys. J. C* 70 (2010) 823,
DOI: `10.1140/epjc/s10052-010-1429-9`, arXiv: `1005.4568 [physics.ins-det]`.

[97] ATLAS Collaboration, *Pile-up profile during Run2 operations*, URL: `https://twiki.cern.ch/twiki/bin/view/AtlasPublic/LuminosityPublicResultsRun2`.

[98] O. Bessidskaia Bylund, "Modelling Wt and tWZ production at NLO for ATLAS analyses",
2016, arXiv: `1612.00440 [hep-ph]`,
URL: `https://inspirehep.net/record/1501477/files/arXiv:1612.00440.pdf`.

[99] ATLAS Collaboration, *Summary plots from the ATLAS Standard Model physics groups*, URL:
`https://atlas.web.cern.ch/Atlas/GROUPS/PHYSICS/CombinedSummaryPlots/SM/`.

[100] ATLAS Collaboration, "Measurement of the $W^\pm Z$ boson pair-production cross section in pp
       collisions at $\sqrt{s}$ = 13 TeV with the ATLAS Detector", *Phys. Lett. B* 762 (2016) 1,
       DOI: 10.1016/j.physletb.2016.08.052, arXiv: 1606.04017 [hep-ex].

[101] ATLAS Collaboration,
       Selection of jets produced in 13 *TeV proton–proton collisions with the ATLAS detector*,
       ATLAS-CONF-2015-029, 2015, URL: https://cds.cern.ch/record/2037702.

[102] ATLAS Collaboration, *2015 start-up trigger menu and initial performance assessment of the
       ATLAS trigger using Run-2 data*, ATL-DAQ-PUB-2016-001, 2016,
       URL: https://cds.cern.ch/record/2136007.

[103] ATLAS Collaboration, *Estimation of non-prompt and fake lepton backgrounds in final states
       with top quarks produced in proton–proton collisions at* $\sqrt{s}$ = 8 *TeV with the ATLAS Detector*,
       ATLAS-CONF-2014-058, 2014, URL: https://cds.cern.ch/record/1951336.

[104] ATLAS Collaboration, *MCTruthClassifier Framework*, URL: https:
       //twiki.cern.ch/twiki/bin/viewauth/AtlasProtected/MCTruthClassifier.

[105] S. Ruder, "An overview of gradient descent optimization algorithms",
       CoRR abs/1609.04747 (2016), arXiv: 1609.04747,
       URL: http://arxiv.org/abs/1609.04747.

[106] M. Feindt, *A Neural Bayesian Estimator for Conditional Probability Densities*, 2004,
       arXiv: physics/0402093 [physics.data-an].

[107] M. Feindt and U. Kerzel, "The NeuroBayes neural network package",
       Nucl. Instrum. Meth. A559 (2006) 190–194, DOI: 10.1016/j.nima.2005.11.166.

[108] ATLAS Collaboration,
       "Electron and photon energy calibration with the ATLAS detector using LHC Run 1 data",
       Eur. Phys. J. C 74 (2014) 3071, DOI: 10.1140/epjc/s10052-014-3071-4,
       arXiv: 1407.5063 [hep-ex].

[109] ATLAS Collaboration, "Jet energy scale measurements and their systematic uncertainties in
       proton-proton collisions at $\sqrt{s}$ = 13 TeV with the ATLAS detector" (2017),
       arXiv: 1703.09665 [hep-ex].

[110] ATLAS Collaboration, *Jet Calibration and Systematic Uncertainties for Jets Reconstructed in
       the ATLAS Detector at* $\sqrt{s}$ = 13 *TeV*, ATL-PHYS-PUB-2015-015, 2015,
       URL: https://cds.cern.ch/record/2037613.

[111] ATLAS Collaboration, *Calibration of the performance of b-tagging for c and light-flavour jets
       in the 2012 ATLAS data*, ATLAS-CONF-2014-046, 2014,
       URL: https://cds.cern.ch/record/1741020.

[112] ATLAS Collaboration, *Calibration of b-tagging using dileptonic top pair events in a
       combinatorial likelihood approach with the ATLAS experiment*, ATLAS-CONF-2014-004,
       2014, URL: https://cds.cern.ch/record/1664335.

[113] J. Butterworth et al., "PDF4LHC recommendations for LHC Run II",
       J. Phys. G 43 (2016) 023001, DOI: 10.1088/0954-3899/43/2/023001,
       arXiv: 1510.03865 [hep-ph].

[114] R. J. Barlow and C. Beeston, "Fitting using finite Monte Carlo samples",
       Comput. Phys. Commun. 77 (1993) 219–228, DOI: 10.1016/0010-4655(93)90005-W.

[115] O. Behnke et al., *Data analysis in high energy physics: a practical guide to statistical methods*,
Weinheim: Wiley-VCH, 2013, URL: https://cds.cern.ch/record/1517556.

[116] K. Cranmer, "Practical Statistics for the LHC", [,247(2015)], 2015 267–308,
DOI: 10.5170/CERN-2015-001.247,10.5170/CERN-2014-003.267,
arXiv: 1503.07622 [physics.data-an].

[117] F. James and M. Roos, "Minuit: A System for Function Minimization and Analysis of the
Parameter Errors and Correlations", *Comput. Phys. Commun.* 10 (1975) 343–367,
DOI: 10.1016/0010-4655(75)90039-9.

[118] M. Baak et al., "HistFitter software framework for statistical data analysis",
Eur. Phys. J. C75 (2015) 153, DOI: 10.1140/epjc/s10052-015-3327-7,
arXiv: 1410.1280 [hep-ex].

[119] G. Cowan et al., "Asymptotic formulae for likelihood-based tests of new physics",
Eur. Phys. J. C 71 (2011) 1554, DOI: 10.1140/epjc/s10052-011-1554-0,
arXiv: 1007.1727 [physics.data-an],
Erratum: *Eur. Phys. J. C* 73 (2013) 2501, DOI: 10.1140/epjc/s10052-013-2501-z.

[120] P. K. Sinervo, "Signal significance in particle physics", 2002 64–76,
arXiv: hep-ex/0208005 [hep-ex].

[121] K. Cranmer et al.,
"HistFactory: A tool for creating statistical models for use with RooFit and RooStats",
tech. rep. CERN-OPEN-2012-016, New York U., Jan. 2012,
URL: https://cds.cern.ch/record/1456844.

[122] L. Moneta et al., "The RooStats Project", *PoS* ACAT2010 (2010) 057,
arXiv: 1009.1003 [physics.data-an].

[123] E. Vryonidou, "LHCTopWG: Theory update on tZj", June 2018,
URL: https://indico.cern.ch/event/708573/contributions/2995420/
attachments/1649998/2638496/VryonidoutZjsm.pdf.

Acknowledgements

Now that I am finally at the end of this journey, I look back and realise that I am filled with gratitude towards so many people that have, in different ways, contributed to the successful completion of this thesis and me getting a PhD.

First and foremost, I would like to thank my supervisor and mentor, Prof. Ian C. Brock for welcoming me into his research group. Your guidance, advice and continuous encouragement during the last five years have been invaluable. I am happy that we got to work together on this analysis and grateful for all the interesting discussions.

I also want to acknowledge and thank all the members of my PhD committee: Prof. Jochen Dingfelder, Prof. Bastian Kubis and Priv.-Doz. Gregor Kirfel for reviewing this thesis.

This analysis is a result of the successful collaboration between the University of Bonn, University of Oklahoma and Boston University so I want to acknowldge the support of everyone involved, in particular Lidia Dell'Asta, Alex Sherman and Muhammad Alhroob, for being a great team and making *tZq* such a fun topic.

This work would definitely not have been possible without the support of the Brock research group. All of you have provided countless times IT support, physics input, as well as good memories, long lasting friendships and an awesome doktorwagen. So, in a roughly chronological order, many thanks to Thomas, Jan, Pienpen, Sebastian, Ozan, Rui, Anji (with extra thanks for the literature and tennis related discussions. Go Federer!), Elena, Regina, Dorothee, Tanja, Rico, Christian, Marius and Alex.

Of course, I can't miss the chance to thank my closest friends. Ozan, I am grateful for all your support and the fun times we had, at the office, in Jamborees and off-work. I really appreciate your constant willingness to share your time and knowledge in order to help others.

Regina, thank you for being the best PostDoc our group could have asked for (and I am sure it's not only my opinion ;)). I hope I learned at least a bit from you about how to keep a smile on my face even when having a million things to work on. And of course, thanks for getting me into running. You can be sure that from now on you will be notified whenever I will sign up for a new race but of course, it won't be as fun as the first one.

Thanks Rui for showing me how one can be simultaneously the most hard-working and the funniest guy in the office. I have no doubt that you will do great things in your physics career! We shared so many fun moments that I cherish but probably my favourite one is still the "highlight of our PhDs" in Braga. You're probably the only person that I would never mind being passed by in a poster contest ;).

Also thanks to all the friends that I made along the way, be it at conferences, during my time at CERN or as a student living in Bonn. In particular, Johannes, I would have not been able to go through the last weeks of my PhD without your help, David for all your support during the writing phase of this thesis and Martin, for your support during the first years of my PhD.

Luckily for me, spatial proximity is not a mandatory requirement when it comes to friendship. Thanks Adina, Elena and Georgiana for being there for me every day, even if 2000+ km away, for all the virtual

coffees, all the advice and, most importantly, for all the fun. May we have many more years of friendship and celebration. Cheers! ;)

I also want to thank my family for always rooting for me and in particular my sister, Adriana, for not asking *too often* about when I will get "a real job".

But most of all, I am grateful to my parents, Marieta and Ionel. I cannot think of better role models of courage, positivity and strength. I am thankful for every word of encouragement and for all the times that you helped me in any possible way, even when I did not want to admit I needed it. The fact that you believe (and make me believe as well) that I can do absolutely anything I set my mind to is a gift that I know not many people have and that I cherish greatly.

I am incredibly lucky for having known everyone mentioned above (and others that maybe I forgot to mention explicitly, for which I apologize). You have all left a mark in my heart and this PhD would really not have been possible without your support.